國立臺灣大學電子資訊學院生醫電子與資訊學研究所
碩士論文
Graduate Institute of Biomedical Electronics and Bioinformatics
College of Electrical Engineering and Computer Science
National Taiwan University
Master’s Thesis

# 開發微流道系統晶片分析剪應力與缺氧刺激對於內皮細胞產生活性氧化物與一氧化氮之影響

# Development of a Microfluidic System to Study the Reactive Oxygen Species and Nitric Oxide Dynamics of Endothelial Cells under Simultaneous Stimulation of Shear Stress and Hypoxia

熊彥程
Yen-Cheng Hsiung

指導教授: 黃念祖 博士
Advisor: Nien-Tsu Huang Ph.D.

中華民國 113 年 6 月
June, 2024

doi:10.6342/NTU202402333

# 國立臺灣大學碩士學位論文
# 口試委員會審定書
## MASTER'S THESIS ACCEPTANCE CERTIFICATE
## NATIONAL TAIWAN UNIVERSITY

開發微流道系統晶片分析剪應力與缺氧刺激對於內皮 細胞產生活性氧化物與一氧化氮之影響

Development of a Microfluidic System to Study the Reactive Oxygen Species and Nitric Oxide Dynamics of Endothelial Cells under Simultaneous Stimulation of Shear Stress and Hypoxia

本論文係 熊彥程 R11945001 在國立臺灣大學電機資訊學院生醫電子與資訊學研究所完成之碩士學位論文，於民國 113 年 6 月 13 日承下列考試委員審查通過及口試及格，特此證明。

The undersigned, appointed by the Graduate Institute of Biomedical Electronics and Bioinformatics, College of Electrical Engineering and Computer Science, National Taiwan University on 13, June 2024 have examined a Master's thesis entitled above presented by Yen-Cheng Hsiung R11945001 candidate and hereby certify that it is worthy of acceptance.

口試委員 Oral examination committee:

黃念祖
（指導教授 Advisor）

郭柏齡

所長 Director: 林致廷

doi:10.6342/NTU202402333

# Acknowledgements

首先先感謝念祖老師努力維持實驗室的運作，讓我們得以持續進行實驗，而細胞實驗一直都不太順利，也感謝老師還願意堅持到三年的實驗結束。另外也感謝老師贊助我前往到波蘭參加2023$\mu$TAS，發表我們的研究內容，第一次去歐洲以及參加微流體最大的研討會是很特殊也開心的體驗。

接著要感謝中研院的董奕鍾老師在實驗上提供很多的幫助，不管是實驗設計上的討論以及實驗場地、器材的提供都是我能完成實驗不可或缺的助力，也感謝秀貞幫忙我在中研院做實驗的各種大小事。

然後是感謝旻諺，如果沒有你開始做這個題目的話，我大概也會陷入不知道做甚麼題目的窘境。然後比我大一屆的王鈞、明儁、彥安、子瑜，在儀器使用、實驗上也常互相討論幫忙，特別是明儁除了比較常陪我吃飯聊天外也常陪我去日k練習唱歌。接下來是感謝跟我同屆的宣融、冠均、啟耀，在許多雜務上能提醒我以及能讓我問，讓我不至於在很多時候搞不清楚狀況。最後感謝淮原也常常陪我聊天跟討論實驗。

一方面我做實驗的地方經常不在實驗室，而且我也不太喜歡待在有其他人的地方做事情，所以總覺得自己跟大家的互動也許還是挺有限的，以後的機會應該就更少了還是挺可惜的。以後還是希望大家能偶爾聚聚分享近況，最後還是感謝大家包容有時候有點驕傲又冒冒失失的我。

# 摘要

心血管疾病是全球最大死因之一，研究心血管的各式反應變得十分重要。本研究中我們開發出一個微流道系統用以建立得以模擬人體內的氧氣及剪應力環境。我們利用四個平行但寬度不同的微流道製造出來的剪應力分別為 2.5, 5, 10, 20 dyne/cm$^2$，同時我們也一個建立了一個介於 2.8 %-12 % 的氧氣濃度梯度。我們在這些微流道中培養人類臍靜脈血管內皮細胞，使這些內皮細胞同時受到剪應力以及氧氣梯度的刺激模擬在人體內的條件。我們使用相位差顯微鏡以及螢光染劑來分析細胞的型態、活性氧化物種以及一氧化氮的胞內表現。我們初步發現細胞沿著流體方向排列的速度較不存在缺氧條件的細胞快，我們更發現間歇性缺氧卻沒有如同缺氧促進細胞轉向的效果。而活性氧化物的分泌量則在一小時的實驗中受到缺氧而有所抑制，最後在六小時的實驗中，一氧化氮表現量並沒有發現明顯變化。這項研究有助於了解內皮細胞在各式心血管疾病、腫瘤以及人體運動時的反應，開發的微流道平台更有助於後人運用研究更複雜的生理條件。

**關鍵字：**微流體、人臍靜脈內皮細胞、活性氧化物種、一氧化氮、剪應力、缺氧

# Abstract

Cardiovascular diseases are the leading cause of death worldwide, making the study of various cardiovascular responses critically important. In this study, we developed a microfluidic system designed to simulate the oxygen and shear stress environments within the human body. Using four parallel microchannels of different widths, we generated shear stresses of 2.5, 5, 10, and 20 dyne/cm$^2$. Additionally, we established an oxygen concentration gradient ranging from 2.8 % to 12 %. Human umbilical vein endothelial cells were cultured within these channels, exposing them to both shear stress and the oxygen gradient to simulate in vivo conditions. We employed phase-contrast microscopy and fluorescent dyes to analyze cell morphology, reactive oxygen species, and nitric oxide production. Preliminary findings revealed that in hypoxic conditions, cell alignment along the flow direction was faster compared to normoxic conditions. We also found that cyclic hypoxia did not enhance cell reorientation. ROS production was suppressed under hypoxia within one hour, while NO production showed no significant changes over a six-hour period. This study enhances our understanding of endothelial cell responses in various cardiovascular diseases, tumors, and during physical exercise. Furthermore, this developed platform can also be a powerful tool for researchers studying complicated physiological conditions.

**Keywords:** microfluidic, human umbilical vein endothelial cell, reactive oxygen species, nitric oxide, shear stress, hypoxia

doi:10.6342/NTU202402333

# Contents

doi:10.6342/NTU202402333

doi:10.6342/NTU202402333

doi:10.6342/NTU202402333

# List of Figures

doi:10.6342/NTU202402333

doi:10.6342/NTU202402333

doi:10.6342/NTU202402333

doi:10.6342/NTU202402333

# List of Tables

doi:10.6342/NTU202402333

# Denotation

| | |
|---|---|
| HUVEC | human umbilical vein endothelial cell |
| ROS | reactive oxygen species |
| NO | nitric oxide |
| PDMS | polydimethylsiloxane |

# Chapter 1 Introduction

Endothelial cells are responsible for forming the inner layer of blood vessels and play a crucial role in exchanging nutrients and waste products between blood and tissues. They are exposed to a variety of stimuli, including oxidative stress, shear stress, and hypoxia, which can affect their function and ultimately impact cardiovascular health. In this chapter, how endothelial cells respond to these stimuli will be reviewed, and then we will review how these conditions are generated in biosystems.

## 1.1 ROS in endothelial cells

Reactive oxygen species (ROS) are the byproduct of cell metabolism, which act as second messengers that are important in cellular physiology. At the physiological concentration of ROS, ROS regulates cell growth, differentiation, senescence, apoptosis, and autography, however, the pathological concentration of ROS, ROS leads to dysfunction and cell death. Hence, the modulation of ROS is very important in cells [36].

### 1.1.1 Source of ROS

ROS includes many species such as free radical peroxide anion ($O_2^{2-}$), free radical superoxide anion $\cdot O_2^-$, hydrogen peroxide $H_2O_2$, etc. However, the $O_2^-$ is the first one generated. Owing to the short lifetime of $O_2^-$, it quickly transforms into other species such as $H_2O_2$ with the help of superoxide dismutases (SOD), which possess the longest lifetime (Figure 1.1). There are two main sources of endogenous ROS in endothelial cells: mitochondrial electron transport chain and NADPH oxidase. In mitochondria, electron leakage occurs in the electron transport chain, particularly in complex I and complex III, and can cause the partial reduction of about 1 - 2 % of $O_2$, which leads to the generation of $\cdot O_2^-$ [69]. Another important source of ROS is the generation of a family of proteins called

NADPH oxidase. Unlike other oxidases, ROS is not the byproduct of these enzymes, while producing ROS is their only function. On this aspect, we can know how important producing ROS to maintain normal redox signaling is. There are seven isoforms of NADPH oxidase identified so far, including NOX1, NOX2, NOX3, NOX4, NOX5, DUOX1, and DUOX2. For example, NOX2 is the major sources of ROS in endothelial cells.

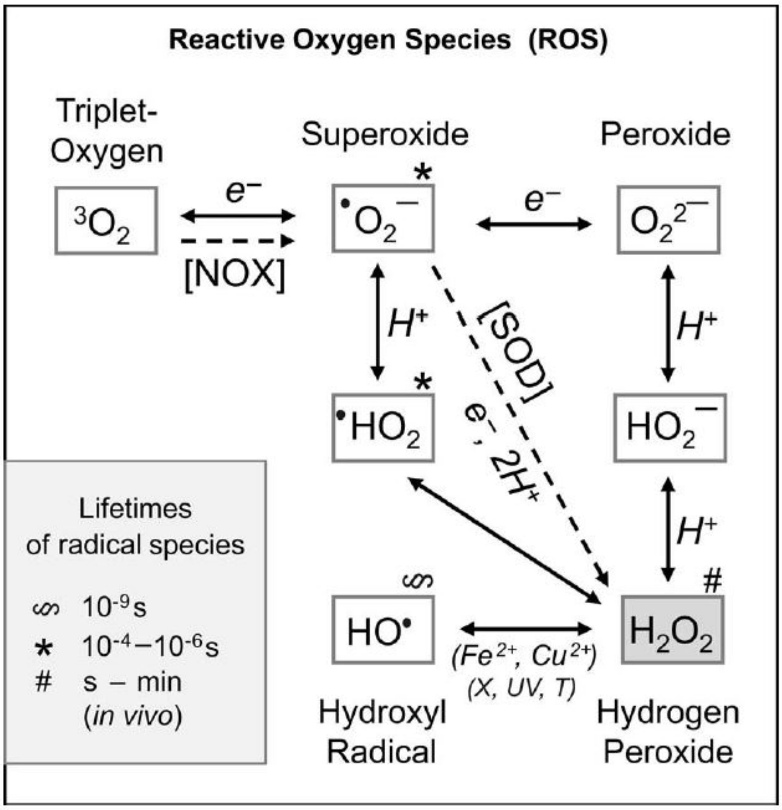

Figure 1.1 Reduction process of ROS. The series reaction is started from the partial reduction of triplet-oxygen. [28]

### 1.1.2 ROS signaling in endothelial cells

ROS related to redox signaling, which is an essential signaling pathway that helps cells function normally (Figure 1.2). In the case of endothelial cells, we focus on angiogenesis. There are two pathways known that ROS regulates angiogenesis (Figure 1.3). The first pathway is mediated by vascular endothelial growth factor (VEGF), the most powerful angiogenetic growth factor that not only engages normal vascular

doi:10.6342/NTU202402333

development but also tumor vasculature. For instance, $H_2O_2$ upregulates the expression of VEGF in endothelial cells [16]. In addition, VEGF also stimulates ROS production [72]. The second pathway, independent of VEGF, is associated with lipid oxidation [39]. ROS oxidases the unsaturated lipid, and then these lipids activate the downstream Toll-like recptor2 (TLR2) and finally lead to angiogenesis. It’s worth noting that TLR is a family of receptors related to the innate immune system, therefore it is interesting that not only ROS can activate angiogenesis through this pathway. That is the reason why lipopolysaccharide, known as the ligand of TLR4, can also trigger endothelial sprouting in vitro and angiogenesis in vivo [17].

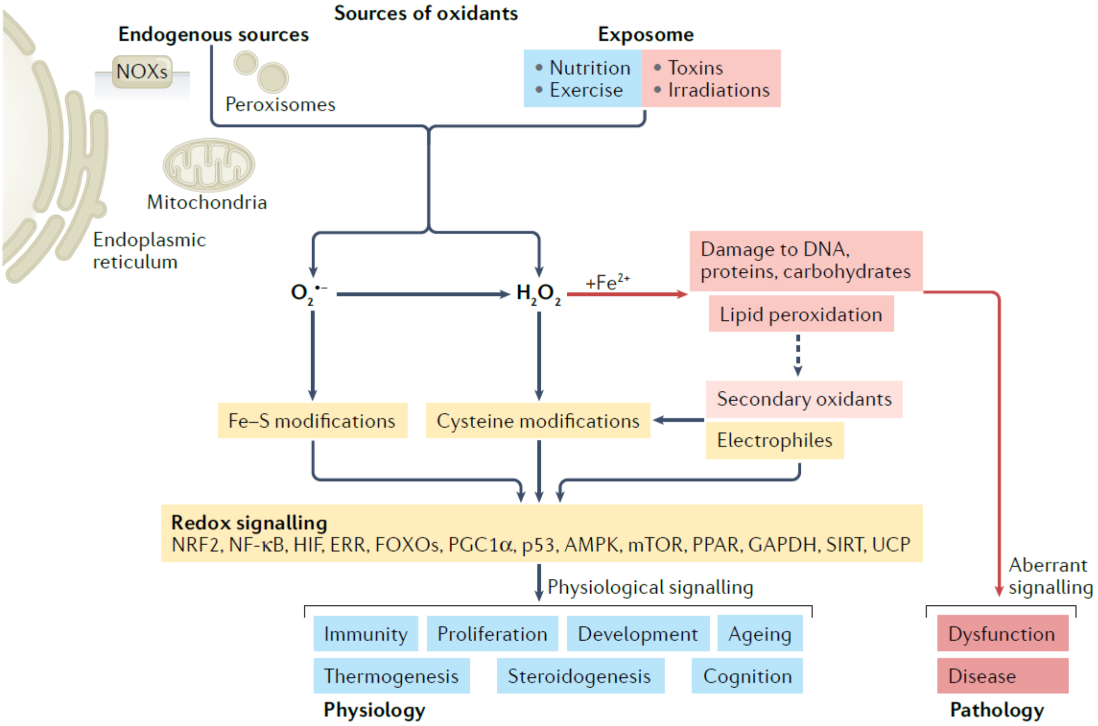

Figure 1.2 Relation of superoxide and hydrogen peroxide to redox signalling [65].

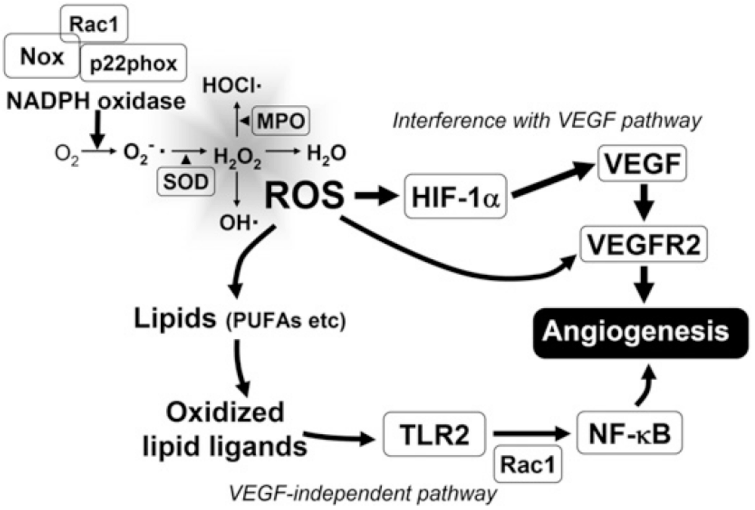

Figure 1.3 Schematic of ROS generation and its effect on angiogenesis [38].

### 1.1.3 ROS related to vascular diseases

When the level of ROS increases above a certain threshold, it can lead to oxidative stress and cause damage to cells and tissues. In the context of vascular disease, ROS is known to play a key role in endothelial dysfunction, which is an early stage in the development of various cardiovascular diseases. In normal conditions, NOX2 and NOX4 induce endothelial cell proliferation and survival, however, excessive levels of NOX2 have been associated with idiopathic pulmonary fibrosis [1]. Similarly, blood polymorphonuclear leukocytes (PMNs) in diabetes have increased levels of mitochondrial ROS production, reduced $O_2$ consumption, and reduced rolling velocity, which correlates with higher interaction with endothelial cells [30]. This interaction is one of the earlier steps in endothelial damage. Furthermore, the development of atherothrombosis is also known to be facilitated by ROS and NO [47].

## 1.2 Hypoxia effect on endothelial cells

Oxygen tension in the human body varies widely. For instance, the oxygen concentration in the lungs is approximately 13%, while it drops to around 5 % in systemic circulation [37]. Different tissues in the human body exhibit distinct oxygen levels, with even lower concentrations found in tumors (Figure 1.4). Consequently, ”physioxia” should refer to the physiological oxygen concentration range of about 4-13 % according to different tissues, which is more representative of in vivo conditions compared to the 20 % oxygen level used in most conventional cell cultures. On the other hand, ”hypoxia” refers to oxygen levels between 0-2 %. With a clear definition of hypoxia, we start our discussion on the most important transcription factor related to hypoxia, HIF.

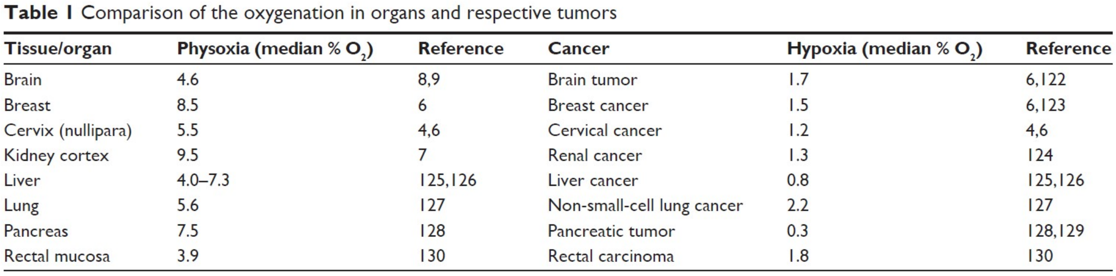

**Table 1** Comparison of the oxygenation in organs and respective tumors

| Tissue/organ | Physoxia (median % $O_2$) | Reference | Cancer | Hypoxia (median % $O_2$) | Reference |
|---|---|---|---|---|---|
| Brain | 4.6 | 8,9 | Brain tumor | 1.7 | 6,122 |
| Breast | 8.5 | 6 | Breast cancer | 1.5 | 6,123 |
| Cervix (nullipara) | 5.5 | 4,6 | Cervical cancer | 1.2 | 4,6 |
| Kidney cortex | 9.5 | 7 | Renal cancer | 1.3 | 124 |
| Liver | 4.0–7.3 | 125,126 | Liver cancer | 0.8 | 125,126 |
| Lung | 5.6 | 127 | Non-small-cell lung cancer | 2.2 | 127 |
| Pancreas | 7.5 | 128 | Pancreatic tumor | 0.3 | 128,129 |
| Rectal mucosa | 3.9 | 130 | Rectal carcinoma | 1.8 | 130 |

Figure 1.4 Oxygen levels in different human tissues [55].

### 1.2.1 HIF-1α and HIF-2α

When cells encounter hypoxic conditions, they must activate a series of cellular responses to survive. A group of proteins known as Hypoxia-Inducible Factors (HIFs) are the key transcription factors that drive the metabolic adaptations required to cope with hypoxia. There are two main types of HIFs that are typically studied: HIF-1α and HIF-2α. These transcription factors regulate both unique and overlapping sets of target genes. HIF-1α is primarily associated with pro-angiogenic responses, promoting the formation of new blood vessels, while HIF-2α is involved in the maturation and stabilization of these vessels. Prolonged expression of HIF-1α can lead to apoptosis, making the transition from HIF-1α to HIF-2α crucial for cells facing extended periods of hypoxia. This transition phenomenon can be observed as these proteins are activated in response to different hypoxic conditions. HIF-1α is rapidly activated within the first few hours of hypoxia but is subsequently degraded. In contrast, HIF-2α becomes the dominant factor after the initial response and remains active for over 24 hours (Figure 1.5). The duration of hypoxia significantly influences cellular responses. In conditions of cyclic or intermittent hypoxia, HIF-1α accumulates, whereas HIF-2α does not get activated during these cycles [49]. This indicates that cells respond differently depending on the hypoxia pattern they experience.

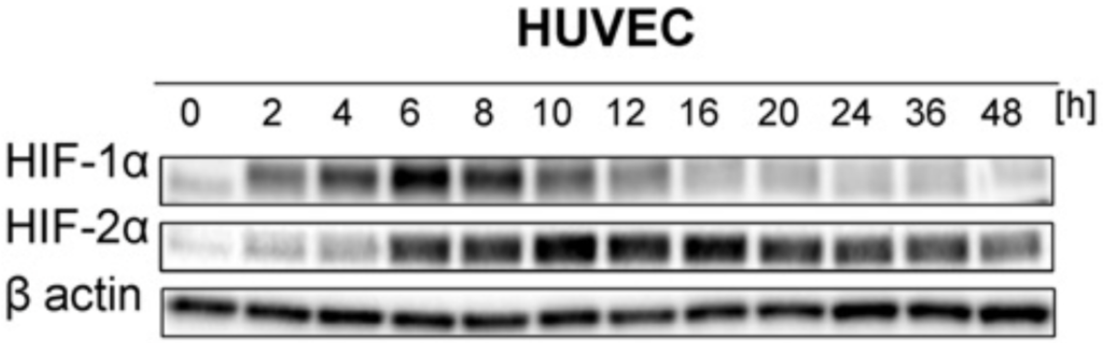

Figure 1.5 The western blotting HIF-1α and HIF-2α in HUVECs exposed to different durations of hypoxia [3].

### 1.2.2 Hypoxia effect on ROS and NO production

Different patterns of hypoxic conditions can lead to different cellular responses. Here, we divided into three groups with duration time: acute hypoxia, chronic hypoxia, and intermittent hypoxia.

Acute hypoxia refers to the cell exposure to the hypoxia for a few minutes or up to a few days [55]. On the other hand, chronic hypoxia is usually induced by tumors that can last up to months or years, but for experimental settings, chronic hypoxia usually refers to between a few hours and several weeks [4]. Although there are no clear boundaries between acute and chronic hypoxia, we can define it through the expression of HIF-1$\alpha$ and HIF-2$\alpha$ (Figure 1.5). Therefore, in this research, chronic hypoxia is defined for those durations that are more than 8 hours when HIF-1$\alpha$ starts to degrade, while HIF-2$\alpha$ starts to be activated. For the case of these two continuous hypoxia, it was found that the

doi:10.6342/NTU202402333

intracellular production of ROS increased up to 0.5 to 6-fold by the stimulation of 1-5% hypoxia (Figure 1.6B) in Hep3B cells. For HUVECs, 0.5 fold increment is also found under 1% of hypoxia (Figure 1.6C), which will internally drive the angiogenesis (Figure 1.7A). However, the extracellular $H_2O_2$ production seems conversely [46]. Moreover, nitric oxide (NO) production is initially inhibited under hypoxia because endothelial nitric oxide synthase (eNOS), the enzyme responsible for NO synthesis, requires $O_2$ as a substrate. The lifetime of eNOS mRNA is also shortened through chromatin-based mechanisms under hypoxic conditions. The downregulated NO can cause the recruitment and activation of neutrophils (Figure 1.7C). This inhibition poses a challenge under hypoxic conditions because NO is crucial for blood vessel dilation. Interestingly, under chronic hypoxia, the expression of neuronal nitric oxide synthase (nNOS), which is found in smooth muscle cells, is gradually upregulated. This leads to an eventual increase in NO concentration in the tissues and thus the blood vessels can function normally (Figure 1.7B, Figure 1.6A).

Cyclic hypoxia is a key feature of tumor microenvironment [54]. Hypoxia with reoxygenation can be regarded as a special case of cyclic hypoxia, and both these two stimuli are reported to increase the production of ROS. In bovine pulmonary artery endothelial cells, the extracellular $H_2O_2$ concentration was observed about two folds higher than control cells after exposure to 24hr hypoxia, while the $H_2O_2$ concentration was three folds lower in the first 2 hours [81]. A similar result is also reported for porcine pulmonary artery endothelial cells [78]. Many studies have elucidated that cyclic hypoxia can increase ROS production in cells [33][12], however seldom report how cyclic hypoxia affects the production of ROS in endothelial cells. Yet, the increase of radioresistance and survival rate after treatment of apoptosis drugs are observed under cyclic hypoxia [48]

doi:10.6342/NTU202402333

[12], and thus we can expect a higher ROS production under this condition.

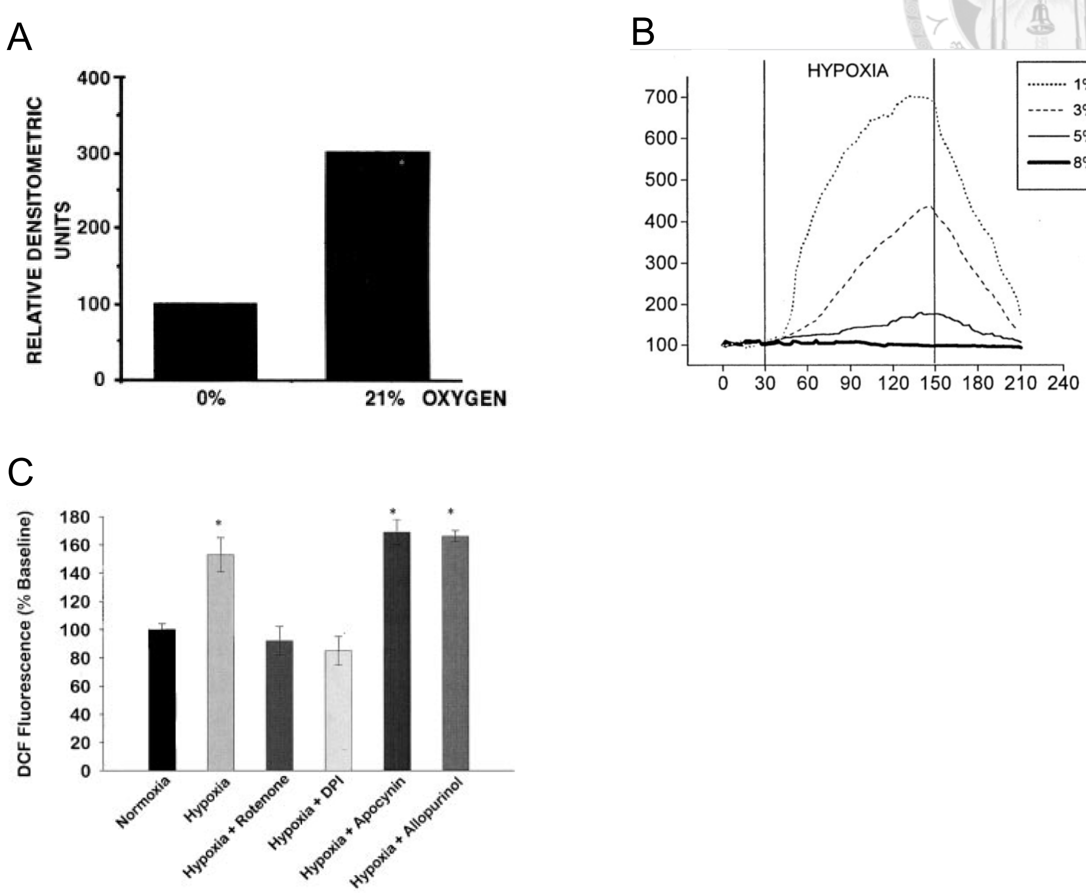

Figure 1.6 (A) The expression of eNOS is found $\frac{1}{3}$ after 48 hours of exposure to hypoxia [51]. (B) Effect of hypoxia on BAECs' ROS generation in 210 minutes [9]. (C) HUVEC's ROS production after 6hrs or hypoxia stimulation [59].

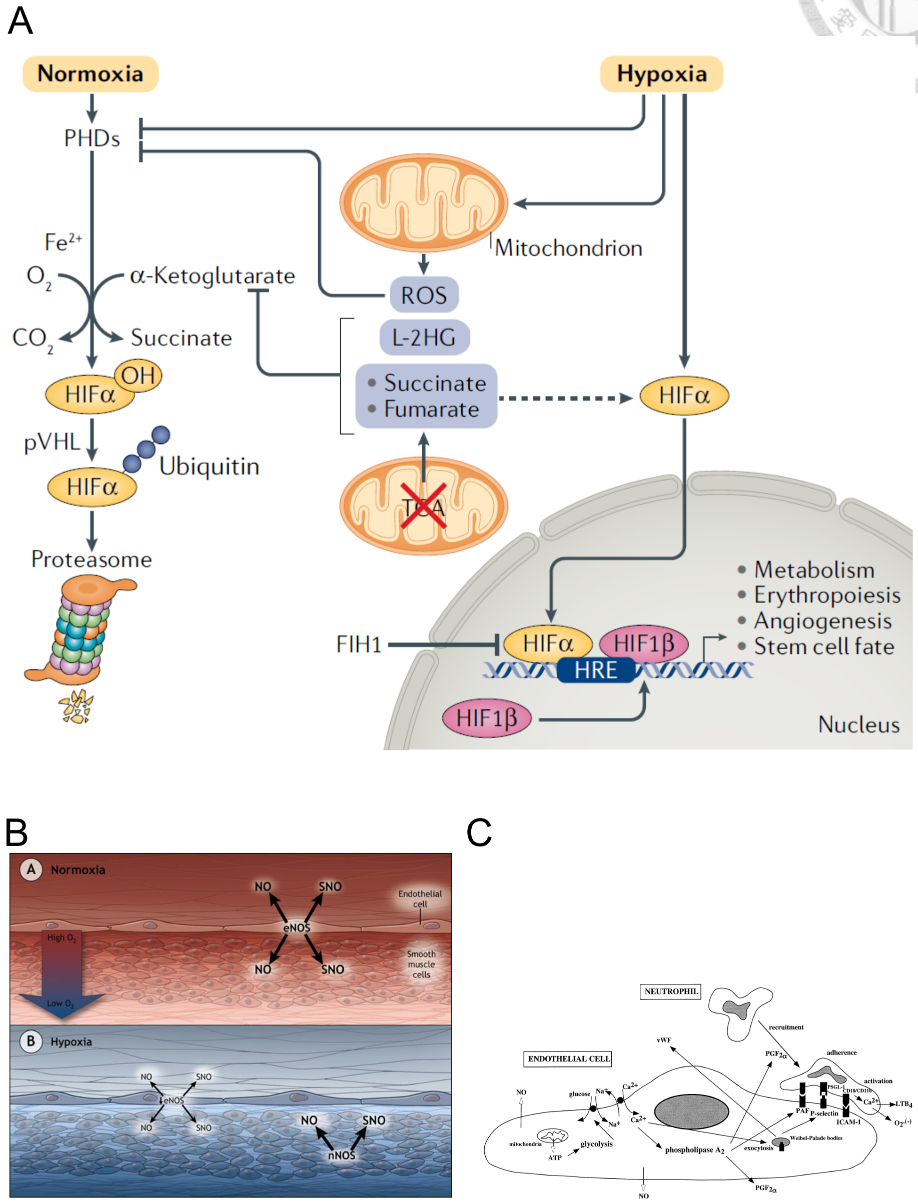

Figure 1.7 (A) Transcription regulation response to hypoxia [41]. (B) Effects of hypoxia on NOS regulation in the vasculature [31]. (C) Response of endothelial cells to hypoxia [53].

## 1.3 Shear stress effect on endothelial cells

Shear stress is also another important stimulus in blood vessels. Therefore, endothelial cells are very sensitive to shear stress. It is sensed by the mechanical sensors on cells and induces responses such as ROS production and anti-inflammation (Figure 1.8A). Interestingly, endothelial cells respond differently according to the pattern of the flow. For example, stable flow can inhibit atherosclerosis, while irregular flow has the opposite effect (Figure 1.8B).

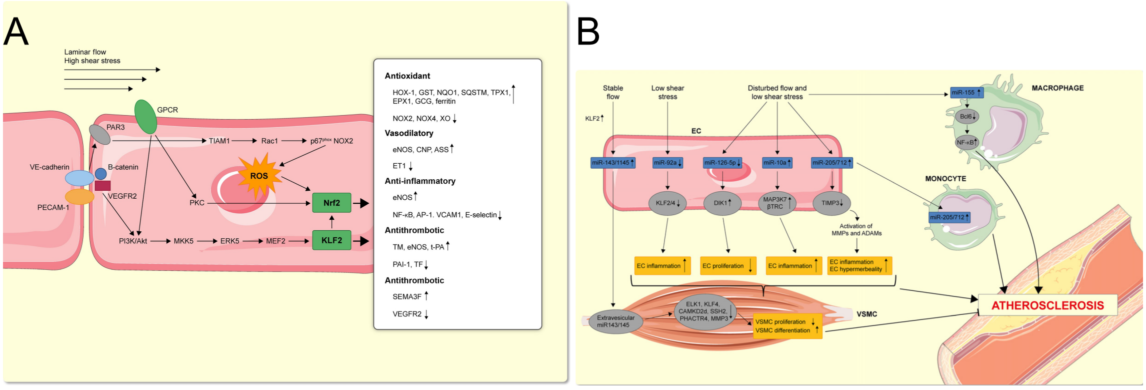

Figure 1.8 (A) Shear stress induces KLF2 and Nrf2 in endothelial cells [15]. (B) The different effects of the pattern of the flow [15].

### 1.3.1 Shear stress on the regulation of ROS and NO

In normal physiological conditions, cells are exerted stable laminar flow by the blood. It is shown that endothelial cells produce 50% to 150% higher ROS when exposed to 15 - 40 dyne/cm$^2$ shear stress for 15 mins (Figure 1.9A), and this difference remains even for 120 min flow (Figure 1.9B). ROS production can also be induced with pulsatile flow (Figure 1.10). However, a prolonged stable flow that continues for more than 24 hours inhibits ROS production [75]. This is reasonable that when the blood vessels are well-formed, the stable (pulsatile) flow therefore exists in the blood vessel, and then the endothelial cells no longer need to proliferate or facilitate other cellular metabolism, that is also called ”quiescent” [15][61]. On the other hand, when the flow pattern starts to be irregular or oscillatory, ROS production is increased and is 3-fold higher than the stable flow group at 4 hrs [50] and 20 hrs [67].

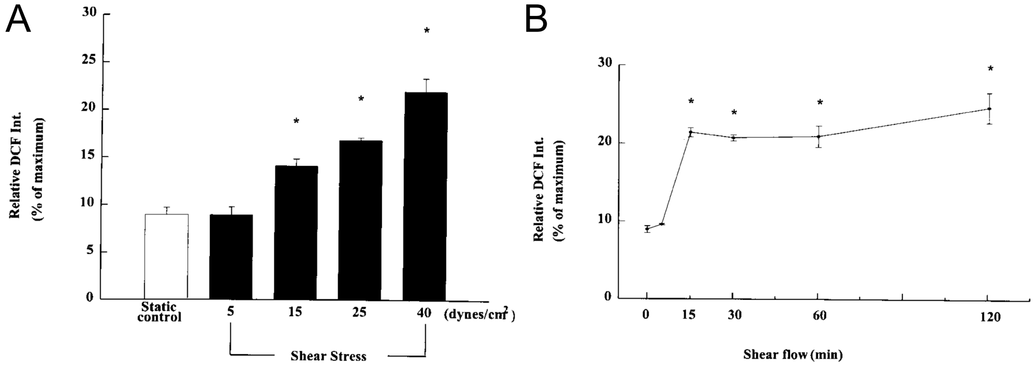

Figure 1.9 (A) The ROS production under varies of shear stress intensity [34]. (B) The ROS production under 40 dyne/$cm^2$ at different times [34].

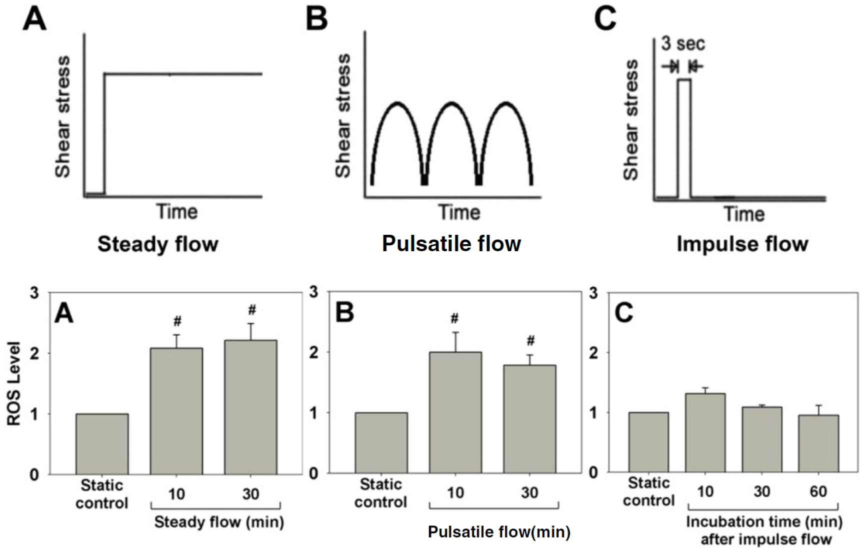

Figure 1.10 ROS production of endothelial cells exposed to different flow patterns [35].

We have already discussed how important is ROS in endothelial cells, meanwhile, NO is another essential molecule that regulates important cell functions in endothelial cells, including angiogenesis, anti-inflammatory, antioxidant and so on. NO is generated by an enzyme called eNOS, which makes NO from L-arginine. By the effect of shear stress, NO production is also induced. Hsiai et al. showed that the eNOS is downregulated by the oscillatory flow (irregular flow) and upregulated by the pulsatile flow (Figure 1.11) in 8hrs and 24hrs [79]. Another research focuses on the ROS and NO production in different wall shear stress and oscillatory frequencies. Although ROS increases as the oscillatory frequency and the wall shear stress increase, the higher frequency does not always guarantee higher NO production (Figure 1.12).

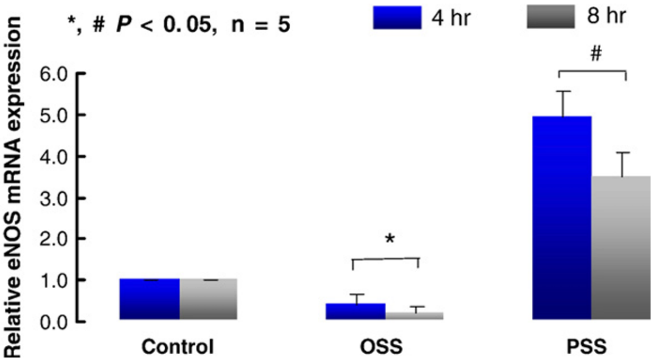

Figure 1.11 eNOS is upregulated by pulsatile flow while inhibited by the oscillatory flow [32].

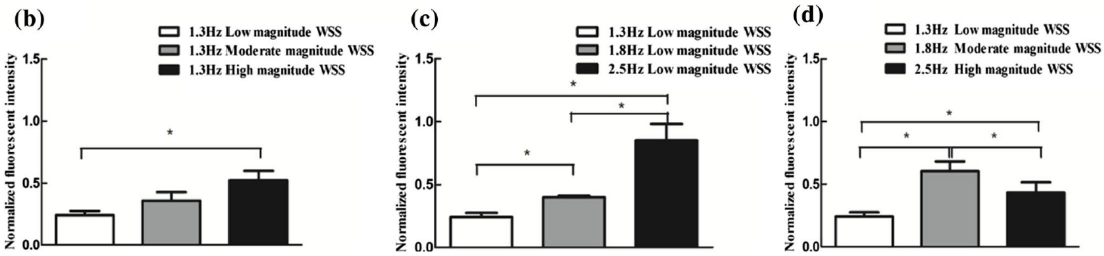

Figure 1.12 The shear stress and the oscillatory frequency increase the production of NO [74].

## 1.3.2 Shear stress on morphology

Shear stress not only affects the metabolism of endothelial cells but also their morphology. For example, the orientation of endothelial cells is highly related to vascular health. The alignment promotes the expression of anti-inflammatory and anti-thrombotic genes to prevent endothelial cells from cardiovascular diseases [2]. The required shear stress to make endothelial cells change their shapes was reported differently in different reports and cell types, however, the same result is that when the shear stress is high enough, elongation and alignment to flow are observed in endothelial cells after enough time of stimulation. The early report of the effects of shear stress is by Levesque et al. [42]. 10-85 dyne/cm$^2$ of shear stress is applied on bovine aortic endothelial cells for 24 hrs. They found that the shape index drops as the shear stress is increased, and the orientation of the endothelial cells starts to change at around 4 hrs of stimulation, but it takes about 24 hours to have the cells well aligned to the flow (Figure 1.13). Another research report that they didn't observe significant orientation changes of bovine aortic endothelial cells until 48 hrs [18]. The shear stress value they adopted is 10 dyne/cm$^2$, which suggests that higher shear stress can fasten the orientation-changing process. Interestingly, Dolan et al. reported that when the shear stress is too high, 284 dyne/cm$^2$ in their experiment, endothelial cells show less alignment compared to those with 35 dyne/cm$^2$ of shear stress [19].

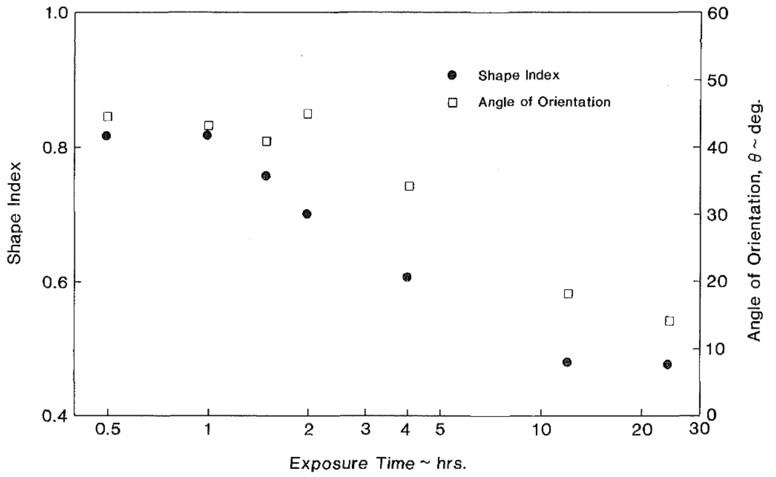

Figure 1.13 The relationship between the shear stress exposure time to the morphology changing of bovine aortic endothelial cells [42].

## 1.4 The combined effect of hypoxia and shear stress

Few studies mentioned the relationship between hypoxia and the morphology of vascular endothelial cells. Botto et al. reported that lung endothelial cells have smaller volumes and higher surface area after exposed to hypoxia [5]. Takahashi et al. show how HUVECs' morphology responds to hypoxia and shear stress. When the flow is not present, the distribution of aspect ratio in the hypoxia group has a higher kurtosis compared to the normoxia group. On the other hand, when the flow is present, hypoxia enhances the alignment to the flow compared to the normoxia group with the flow (Figure 1.14).

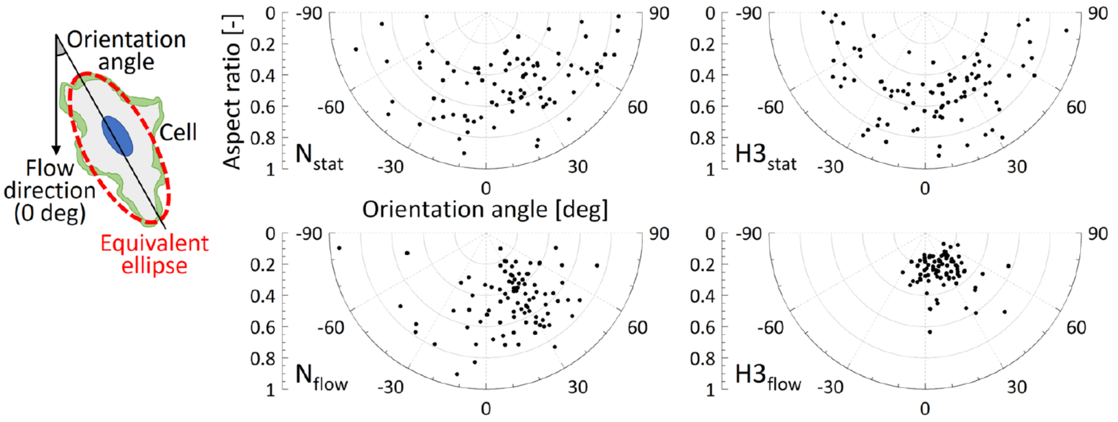

Figure 1.14 The morphology distribution after HUVECs exposed to flow and 3% oxygen for 6 hrs [68].

## 1.5 Literature review

In the previous section, we discussed how shear stress and hypoxia affect the metabolism of endothelial cells. In this chapter, we will explore the traditional approaches to studying these two stimuli, as well as recent advancements in microfluidic systems that have enabled more precise measurements and control.

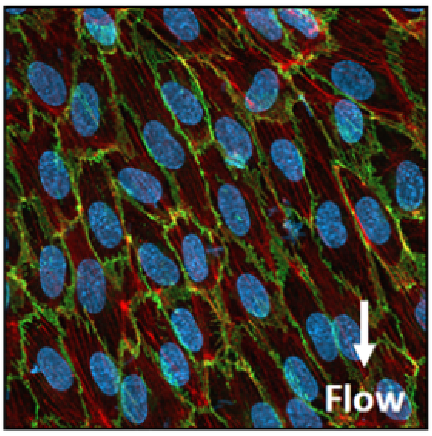

Figure 1.15 The immuno staining after HUVECs exposed to flow and 3% oxygen for 6 hrs (red: Actin filaments, green: VE-cadherin, blue: nuclei) [68].

### 1.5.1 Traditional methods to generate shear stress

Early research involved culturing cells in Petri dishes or flasks [18][42], which are not capable of applying shear stress within. These static cultures failed to reproduce the dynamic in vivo environment, leading to altered cellular behavior. Consequently, the need to generate shear stress in cell culture systems became apparent.

One of the simplest methods for applying shear stress is the rotary cell culture system. In this technique, cells are seeded onto a flask or bioreactor that rotates at a constant speed. This rotation creates a low-shear environment that mimics some aspects of the in vivo conditions. Rotary cell culture systems are advantageous due to their simplicity and the ability to maintain a relatively uniform shear stress across the cell surface [66]. The parallel-plate flow chamber is another widely used method. In this setup, cells are placed on one of the plates, while the other serves as a chamber wall, creating a narrow flow chamber. Fluid is pumped through this chamber, generating shear stress on the cell monolayer. This method allows for precise control over shear stress magnitude and can replicate various physiological and pathological conditions [24][71][42]. Lastly, the cone

doi:10.6342/NTU202402333

and plate apparatus is a common method for generating shear stress. This technique involves placing a rotating cone on a stationary cell culture plate. As the cone rotates, it generates a uniform shear stress across the plate. This method is particularly useful for creating well-defined and consistent shear stress environments, making it a preferred choice for many experimental setups [70][18].

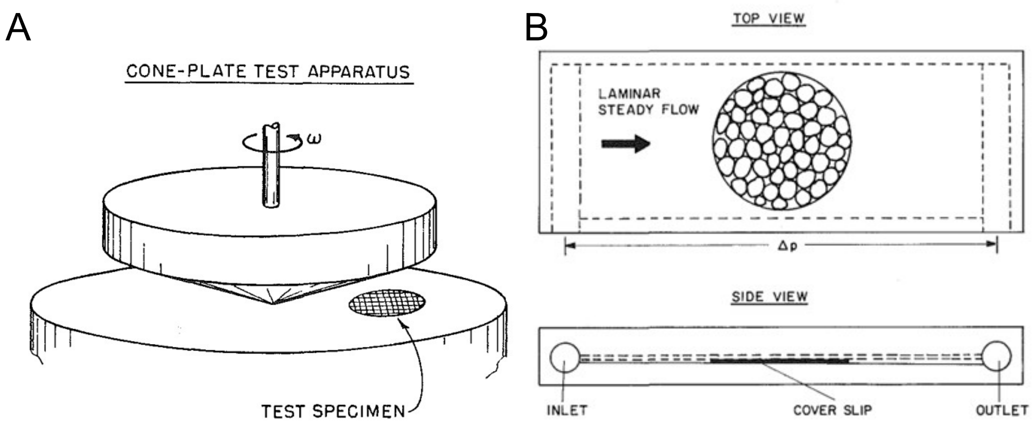

Figure 1.16 Illustration of cone-and-plate system [18] and parallel plate method [42].

### 1.5.2 Methods to study shear stress in microfluidics

Microfluidics has emerged as a powerful tool for establishing complex conditions for cell cultures. By leveraging microchannels and precise flow control, researchers can generate physiologically relevant shear stress conditions to study cellular responses. This section will review various techniques to apply shear stress using microfluidic systems.

In microfluidic systems, shear stress can be applied to cells by connecting a pump to a microchannel. By adjusting the flow rate or channel dimensions, the desired shear stress can be achieved. While this approach is straightforward, several advanced techniques have been developed to meet specific research needs. Hattori et al. introduced a method using flow-control channels to manipulate flow resistance and, consequently, the flow rate within each channel. This approach allows researchers to adjust shear stress without altering the channel width (Figure1.17). By integrating peristaltic pumps, which generate pulsatile flow, their system can better mimic in vivo conditions. Their study demonstrated that HUVECs align with the flow when shear stress exceeds 4.9 dyne/cm$^2$.

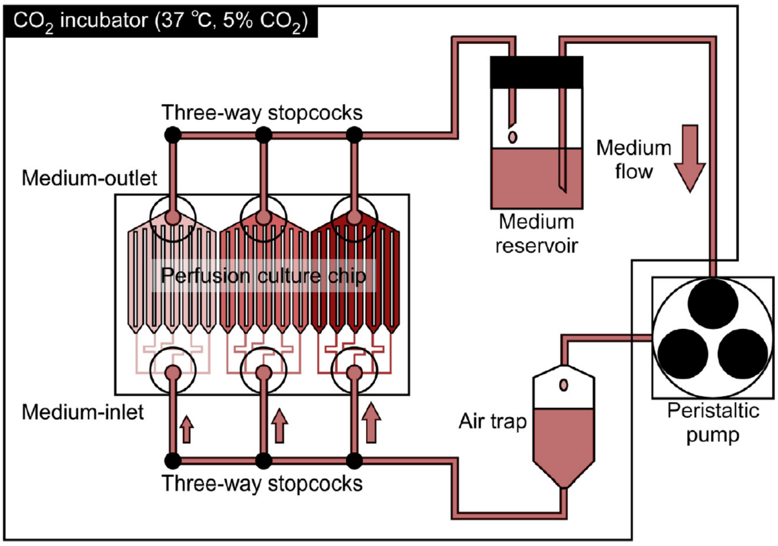

Figure 1.17 Culturing system with flow-control channels that adjusts the flow resistance [29].

Peristaltic pumps are commonly used in microfluidic systems to create pulsatile flow, which is more representative of physiological conditions. Previous studies have shown that endothelial cells respond differently to various flow patterns [35]. The pulsatile flow generated by peristaltic pumps can closely simulate the conditions experienced by endothelial cells in vivo, making this method particularly useful for studying vascular biology [13]. Chin et al. designed microfluidic channels with integrated valves, allowing for different durations of flow stimulation within a single experiment (Figure 1.18). This design enables the simulation of various shear stress conditions in a controlled manner. Additionally, they incorporated a concentration generator to examine how varying glucose concentrations affect ROS production in cells. This integrated approach provides a comprehensive platform for studying the combined effects of shear stress and biochemical factors on cellular behavior.

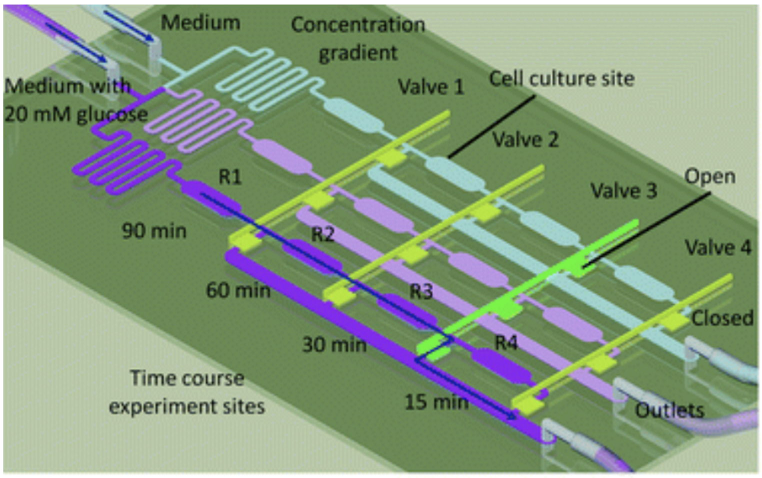

Figure 1.18 Different duration of shear stress and glucose concentration stimulation combined in one chip [14].

## 1.6 Generating hypoxia in microfluidics

Although hypoxic condition can easily be generated by using a hypoxia chamber, microfluidics have the advantages of precise control and even oxygen gradient generation, which makes microfluidics a new powerful tool for such studies. To generate the wanted hypoxia microenvironment in microfluidics, there are three different oxygen scavengers adopted: gases, chemical reactions and cells.

### 1.6.1 Using gases as oxygen scavengers

Gases are usually utilized for generating hypoxic conditions because using them is straightforward and biocompatible. Due to the oxygen permeability of the PDMS, the oxygen dissolved in the medium will diffuse into the gas channel that is filled with pure nitrogen through the PDMS membrane between them. However, due to the zero humidity of the gas, a hydration layer should be added or fresh medium should be kept flowing into the microfluidic channel in case of evaporation of water in the medium. By controlling the composition of premix gas, different levels of hypoxia or cyclic hypoxia can be achieved.

Liu et al. used such a technique to study the real-time response of the electrical impedance of erythrocytes by adjusting the gas valve (Figure 1.19). Grist et al. added a hydration layer inside the device for long-term observation of spheroid behavior under chronic and cyclic hypoxia (Figure 1.20A). To make the convex oxygen distribution due to the reoxygenation of the oxygen permeability of PDMS uniform, Funamoto et al. add a PC film within the PDMS device. The film is 2mm above the cell channel to limit oxygen diffusion (Figure 1.20B).

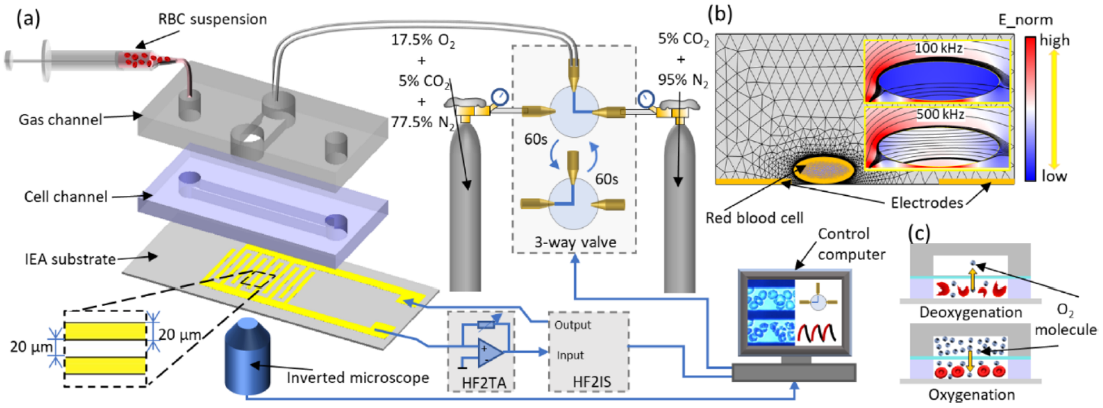

Figure 1.19 A cyclic hypoxia system for studying the electrical impedance of erythrocytes [44].

By combining a concentration gradient generator, the multiplexity of microfluidics can be leveraged and study different hypoxic conditions simultaneously [21]. Applying shear stress in culture systems such as endothelial cells can be important, however, the flow applied to generate shear stress will affect the control of oxygen. To decouple these two parameters, Bouquerel et al. propose a system named ”Oxilas” to achieve the requirement through precise control of gas supplementation (Figure 1.21).

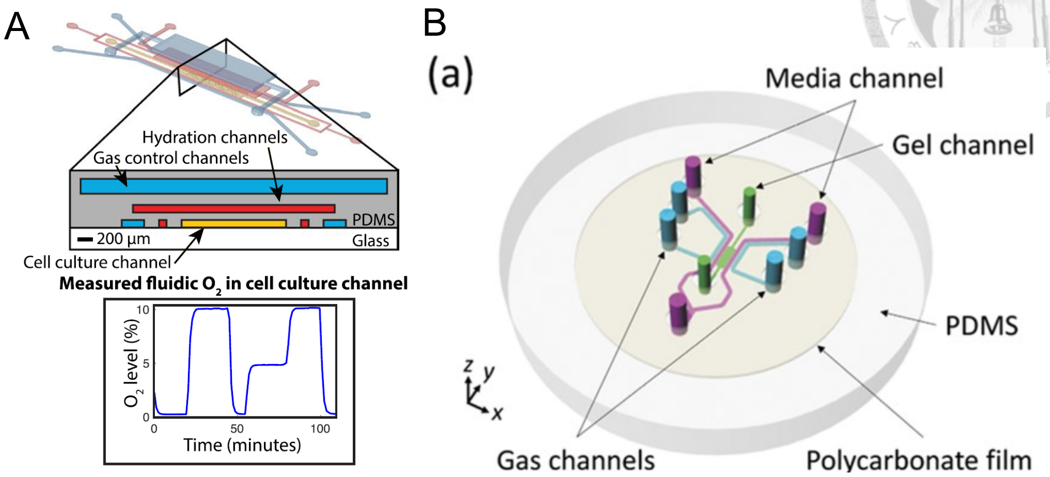

Figure 1.20 (A) A microchannel with hydration layer for studying the spheroid response to cyclic hypoxia [27]. (B) A PC film is inserted in the microfluidic device to further inhibit the diffusion of oxygen in PDMS [40][22].

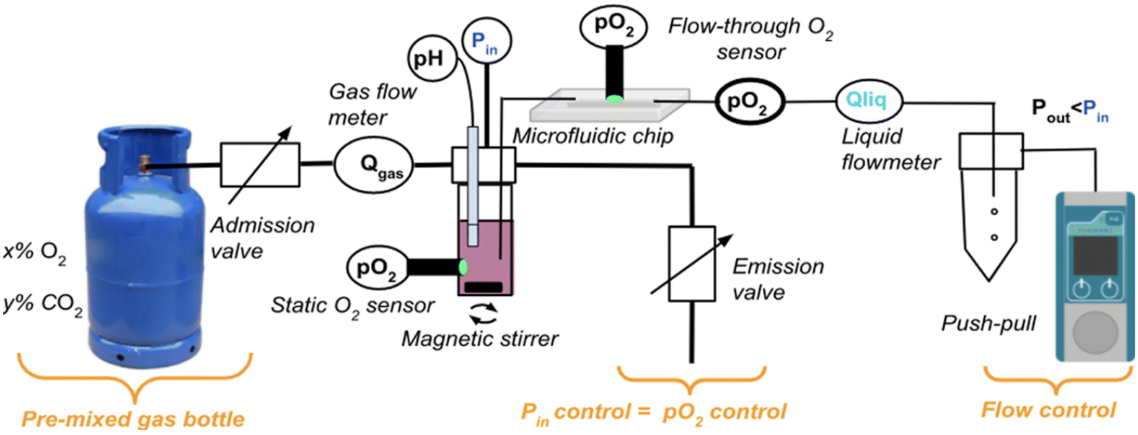

Figure 1.21 A precise control and calculated system for decoupling shear stress and oxygen level [6].

## 1.6.2 Using chemical reactions as oxygen scavengers

Shih et al. show that by flowing pyrogallol and NaOH on the side of the cell culturing channel oxygen gradient can be generated to study the migration of HUVECs cross through the oxygen gradient. A chemical concentration gradient can also be applied simultaneously to create both a chemical gradient and an oxygen gradient in the same chip (Figure 1.22A). The oxygen tension can also be adjusted by tuning the concentration of pyrogallol only [43]. Besides pyrogallol, sodium sulfite is also a frequently used chemical molecular due to its biocompatibility. For example, Wang et al. introduced sodium sulfite into the cell medium to create an oxygen gradient (Figure 1.22B). With proper and precise quantitative calculation of convection and diffusion, cyclic hypoxia and the level of oxygen tension can also be precisely generated [64].

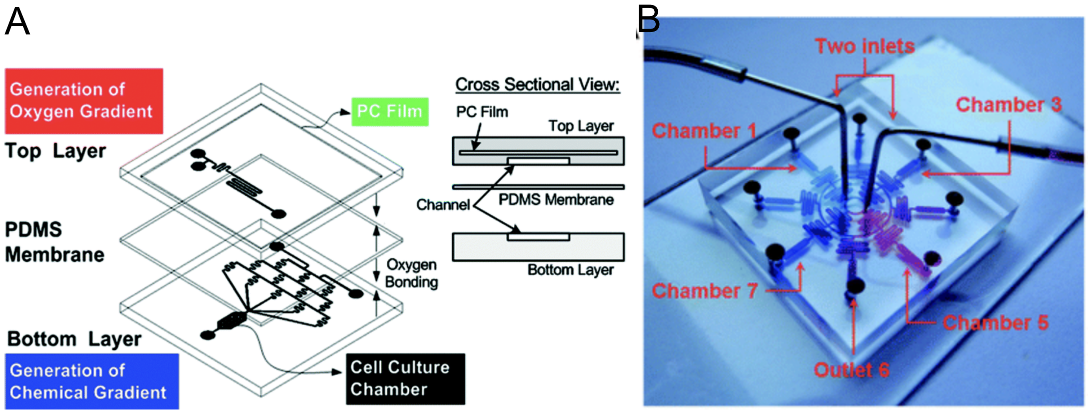

Figure 1.22 (A) Chemical gradient and oxygen gradient integrated for studying A549 [10]. (B) Hypoxia generation by concentration generation of sodium sulfite [73].

## 1.6.3 Using cells as oxygen scavengers

Cells themselves, of course, consume oxygen. This makes cells themselves the easiest tool to create hypoxic conditions by using low oxygen permeability materials, such as glass, polystyrene, SU-8, and cyclic olefin copolymer (COC) [57], though the conditions are fixed once the experiment is set up. Oh et al. used a PC film as the low-oxygen permeability material to generate tumor hypoxia for testing chemo drugs [56]. Grant et al. used PDMS to establishing an oxygen gradient [26].

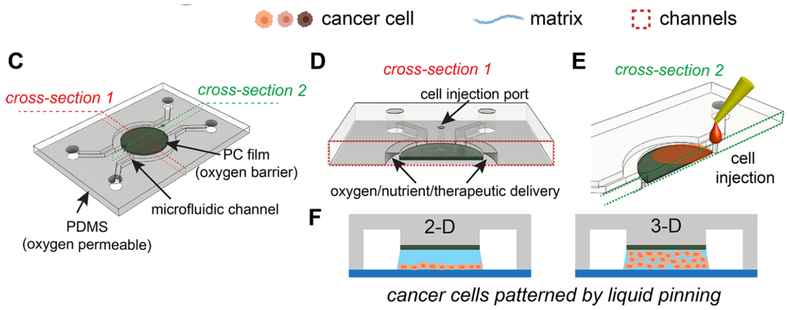

Figure 1.23 Leaveraging the consumption of oxygen of cells themselves, a hypoxic oxygen gradient can be established [73].

### 1.6.4 Using $CoCl_2$ as hypoxia inducers

$CoCl_2$ is a chemical that can mimic the hypoxic condition by inducing a HIF-1 in cells [60]. Chen et al. used $CoCl_2$ to investigate the cell-cell interaction between HUVEC and pigment epithelial cells under a hypoxia environment [11]. Zielke et al. also used $CoCl_2$ to induce the hypoxia reactions in tumor cells and utilized droplet microfluidic to select each single cell that is treated by $CoCl_2$ [80].

Table 1.1: Hypoxia microenvironment establishment methods in microfluidics

| Cell type | Method | Hypoxia pattern | Feature | Reference |
|---|---|---|---|---|
| Erythrocyte | gas | cyclic | impedance measurement | [44] |
| MCF-7 | gas | chronic & cyclic | hydration layer | [27] |
| MCF7 | gas | oxygen gradient | gradient generator | [21] |
| MDA-MB-231 | gas | oxygen gradient | PC film | [40] |
| HUVEC | gas | oxygen gradient | PC film | [22] |
| A549 | gas | chronic & cyclic | precise control system | [6] |
| HUVEC | gas | chronic | combined with shear stress | [68] |
| HUVEC | pyrogallol | oxygen gradient | cell migration | [63] |
| A549 | pyrogallol | oxygen gradient | chemical gradient | [10] |
| A549 | pyrogallol | chronic hypoxia | pyrogallol concentration generator | [43] |
| HeLa & A549 | sodium sulfite | oxygen gradient | realtime oxygen monitoring | [73] |
| MDA-MB-231 | sodium sulfite | cyclic and oxygen gradient | quantitative control | [64] |
| LNCaP | cell consumption | chronic | liquid pinning | [56] |
| Human small intestine epithelium& HIMEC | cell consumption | gradient | oxygen sensor | [26] |
| pigment endothelial cell & HUVEC | $CoCl_2$ | - | cell-cell interaction | [11] |
| MDA-MB-231 | $CoCl_2$ | - | single-cell selection | [80] |

## 1.7 Motivation

Many devices can generate shear stress or hypoxic conditions in microfluidic systems to study cellular responses. However, few can simultaneously apply both stimuli to investigate the combined effects of hypoxia and shear stress, which cells often experience in vivo. Additionally, gradients play a crucial physiological role; for example, HUVECs migrate towards low oxygen concentrations [63]. Therefore, generating an oxygen gradient in microchannels is essential not only for studying various oxygen levels simultaneously but also for accurately mimicking physiological microenvironments. To address these challenges, we designed a microfluidic chip capable of generating an oxygen gradient ranging from hypoxia to physioxia. Furthermore, cyclic hypoxia is known to activate different signaling pathways in cells. While previous research often required a bulky gas-mixing system to create such environments, which may not be available in many laboratories, we demonstrate that cyclic hypoxia can be achieved by simply programming the flow rate of syringe pumps. Lastly, we selected reactive oxygen species (ROS) and nitric oxide (NO) as key experimental observables to understand how hypoxia and shear stress may lead to cell dysfunctions, which are the early development of cardiovascular diseases. This study aims to provide a more comprehensive understanding of these combined stimuli, potentially leading to better therapeutic strategies.

doi:10.6342/NTU202402333

# Chapter 2 Theory

## 2.1 Hypoxic condition in microfluidic device

Here, we try to derive the theory to describe the oxygen concentration. We first start with the model definition. The simplified 2D device is shown as Figure 2.1. The channel filled with medium is first flow next the hypoxia region with pyrogallol inside and then PDMS for reoxygenation. We then deal with the oxygen concentration in the PDMS. We assume the pyrogallol reacts very fast to the oxygen, so the process is diffusion-dominated, which can be described by Fick's laws [20]. Fick's laws are written as equations 2.1, where c is the concentration, J is the flux and D is the diffusion coefficient.

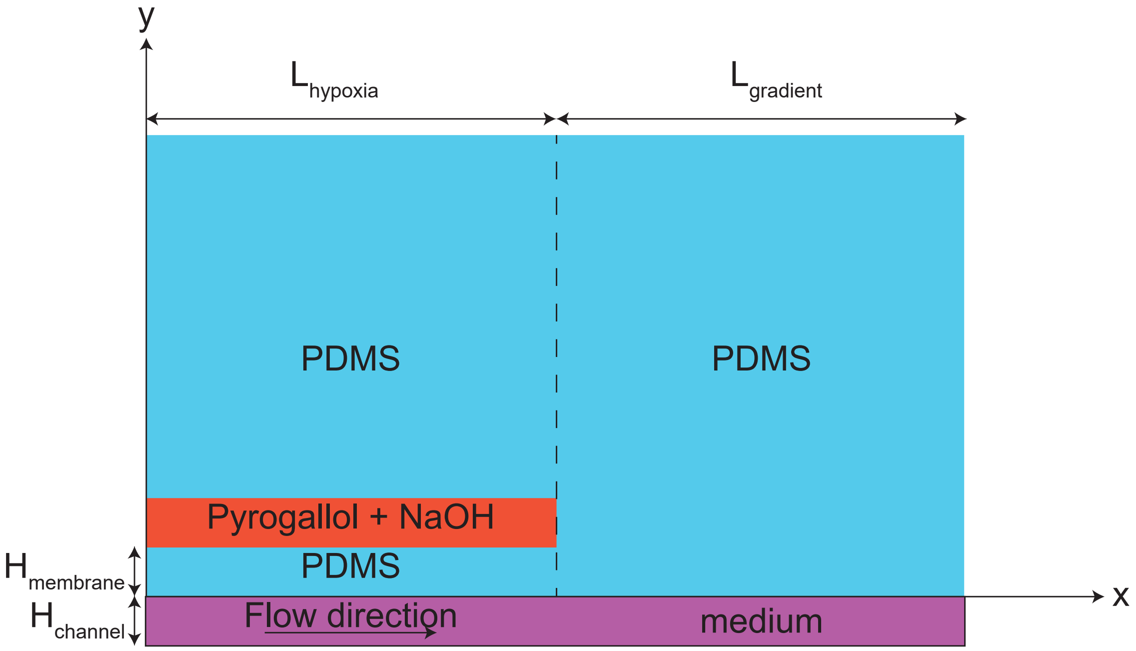

Figure 2.1 The geometry and parameters definition used in the derivation.

$$J = -D\nabla \cdot c \tag{2.1a}$$

$$\frac{\partial c}{\partial t} = D\nabla^2 c \tag{2.1b}$$

doi:10.6342/NTU202402333

We then can roughly estimate $\frac{\partial c_{\text{pdms}}}{\partial x} / \frac{\partial c_{\text{pdms}}}{\partial y} = \frac{H_{\text{channel}}}{H_{\text{membrane}}} = \frac{10*10^{-3}}{60*10^{-6}}$, so the we reduce Fick'law to 1D case in the diffusion process in PDMS. And then, for $0 \leq x \leq L_{\text{hypoxia}}$, the flux of oxygen, $J_{mp}$, is flowing from medium to PDMS. We can get the following equation.

$$J_{mp} = -D_{\text{pdms}} \frac{\partial c_{\text{pdms}}}{\partial y} \tag{2.2}$$

For a steady state, equation 2.1b equals to 0 everywhere. Combined with the previous assumption, $\frac{\partial c_{\text{pdms}}}{\partial y} =$ constant. We apply boundary condition that $c_{\text{pdms}}(x, H_{\text{membrane}})$, for $0 \leq x \leq L_{\text{hypoxia}} = 0$ due to the fast reaction of pyrogallol. Finally, we ignore the fringe effect. We now get the following relation:

$$J_{mp}(x) = D_{\text{pdms}} \frac{c_{\text{pdms}}(x, 0)}{H_{\text{membrane}}} \tag{2.3}$$

We assume the equilibrium at the interface of PDMS and medium is very fast and obey Henry's law: $c_{\text{pdms}}(x, 0) = c_{\text{medium}}(x, 0) * \frac{\text{solubility}_{\text{medium}}}{\text{solubility}_{\text{pdms}}}$. Applying Henry's law to equation 2.3 gets the following relation between $J_{mp}$ and $c_{\text{medium}}$

$$J_{mp}(x) = -\frac{\mathrm{d}c_{\text{medium}}(x, 0)}{\mathrm{d}t} * H_{\text{channel}} = -\frac{D_{\text{pdms}} * \text{solubility}_{\text{pdms}}}{H_{\text{membrane}} * \text{solubility}_{\text{medium}}} c_{\text{medium}}(x, 0) \tag{2.4}$$

Now we look at the part in the medium. Although the medium involves in both convection and diffusion processes, the x-axis is convection process dominated while y-axis is diffusion dominated. We can again reduce Fick's law into the 1D case in the medium. At this moment, we ignored the equilibrium time needs in the medium, and assume $\frac{\partial c^2_{\text{medium}}}{\partial^2 y} \approx 0$ for estimation. We get the relationship of $c_{\text{medium}}(x, 0)$ and $c_{\text{medium}}(x, y)$.

$$\begin{aligned} c_{\text{medium}}(x, y) &= c_{\text{medium}}(x, 0) - y\frac{J_{mp}}{D_{\text{medium}}} \\ &= (1 - y\frac{D_{\text{pdms}}}{D_{\text{medium}}}\frac{\text{solubility}_{\text{pdms}}}{\text{solubility}_{\text{medium}}})c_{\text{medium}}(x, 0) \end{aligned} \tag{2.5}$$

Substituting equation 2.5 into 2.4 for $y = -\frac{1}{2}H_{\text{channel}}$

$$\begin{aligned} \frac{\mathrm{d}c_{\text{medium}}(x, -\frac{1}{2}H_{\text{channel}})}{\mathrm{d}t} &= -\frac{D_{\text{pdms}} * \text{solubility}_{\text{pdms}}}{H_{\text{channel}} * H_{\text{membrane}} * \text{solubility}_{\text{medium}}} \\ &\quad \frac{1}{1 + \frac{1}{2}H_{\text{channel}}\frac{D_{\text{pdms}}}{D_{\text{medium}}}\frac{\text{solubility}_{\text{pdms}}}{\text{solubility}_{\text{medium}}}} c_{\text{medium}}(x, -\frac{1}{2}H_{\text{channel}}) \\ &= -9.82(c_{\text{medium}}(x, -\frac{1}{2}H_{\text{channel}})) \end{aligned} \tag{2.6}$$

We keep significant figures here to be 3. Notice that the second term to calibrate the concentration difference along to channel is very close to 1 due to the short channel height. With the relationship $x = vt \Rightarrow \mathrm{d}x = v\mathrm{d}t \Rightarrow \frac{\mathrm{dc}}{\mathrm{d}x} = \frac{1}{v}\frac{\mathrm{dc}}{\mathrm{d}t}$. Where $v = \frac{3}{2}\bar{v} = \frac{3}{2}Q/A = 6 \times 10^{-3}$. By solving the differential equation, and apply boundary conditions, we finally reach the expression of $c_{\text{medium}}(x, -\frac{1}{2}H_{\text{channel}})$.

$$c_{\text{medium}}(x, -\frac{1}{2}H_{\text{channel}}) = 0.22 * e^{-x/6.1\times 10^{-4}} \tag{2.7}$$

We define oxygen concentration less than 2% to be hypoxia, so when $e^{-x/6.1\times 10^{-4}} < 0.1 \Rightarrow x \approx 1.2 \times 10^{-3}$ (m) the culture channel enters the hypoxic condition. However, the diffusion length that can be derived in Fick's law $= 2\sqrt{D_{\text{medium}}t} \geq 50\mu m$ when $t \geq 0.658s$. This means that the medium has traveled $v_{max} * t \approx 4$ (mm) right after the oxygen at the bottom of the channel has reached the top. Hence, we here give a rough estimation that about 4+1.2=5.2 mm is needed to reach hypoxic conditions.

Now, we estimate the recovery of oxygen at downstream. If we assume the oxygen concentration at the downstream is filled with full oxygen. We can get similar equation below

$$\begin{aligned} J_{pm} &= D_{\text{medium}} \frac{\text{solubility}_{\text{medium}} - c_{\text{medium}}(x)}{H_{\text{channel}}} \\ \Rightarrow \frac{\partial c_{\text{meidum}}(x)}{\partial x} &= \frac{1}{v * H_{\text{channel}}} [D_{\text{medium}} \frac{\text{solubility}_{\text{medium}} - c_{\text{medium}}(x)}{H_{\text{channel}}}] \end{aligned} \tag{2.8}$$

Therefore, the expression of $c_{\text{medium}}$

$$c_{\text{medium}}(x) = 0.22 - 0.22e^{-\frac{x}{1.316 * v_{max}}} \tag{2.9}$$

However, we have known that this result is far away from the experimental simulation results. This is because that the assumption that PDMS is full of oxygen is wrong. Here, we give a heuristic way to estimate this effect. For a steady state, the oxygen profile is a straight line and independent of the width of the culture channel or the flow velocity in it, therefore we assume $c_{\text{pdms}}$ as follows.

$$c_{\text{pdms}}(x, 0) = \frac{x - L_{\text{hypoxia}}}{L_{\text{gradient}}} * \text{solubility}_{\text{pdms}} * 0.75, \text{ for } x > L_{\text{hypoxia}} \tag{2.10}$$

We add a 0.75 coefficient here is because there are still some distances from the channel ends to the device margin. Then the oxygen flux that diffuses back to the medium is (as shown in the previous derivation, we ignore the concentration differences along the y-axis in the culture channel)

$$
\begin{aligned}
J_{pm} &= D_{\text{medium}} \frac{\frac{\text{solubility}_{\text{medium}}}{\text{solubility}_{\text{pdms}}} c_{\text{pdms}}(x,0) - c_{\text{medium}}(x)}{H_{\text{channel}}} \\
&= \frac{D_{\text{medium}}}{H_{\text{channel}}} (\text{solubility}_{\text{medium}} * 0.75 \frac{(x - L_{\text{hypoxia}})}{L_{\text{gradient}}} - c_{\text{medium}}(x)) \qquad (2.11) \\
\Rightarrow \frac{\partial c_{\text{medium}}(x)}{\partial x} &= \frac{1}{v * H_{\text{channel}}} [\frac{D_{\text{medium}}}{H_{\text{channel}}} (0.75\text{solubility}_{\text{medium}} \frac{(x - L_{\text{hypoxia}})}{L_{\text{gradient}}} \\
&- c_{\text{medium}}(x))]
\end{aligned}
$$

We let $c(0) = 0$ here, the expression of $c_{\text{medium}}$ is

$$
\begin{aligned}
c_{\text{medium}}(x) &= 0.75\text{solubility}_{\text{medium}} \frac{(x - L_{\text{hypoxia}})}{L_{\text{gradient}}} \\
&- \frac{0.75\text{solubility}_{\text{medium}} H^2_{\text{channel}} v}{D_{\text{medium}} * L_{\text{gradient}}} (1 - e^{-\frac{D_{\text{medium}}}{H^2_{\text{channel}} * v}(x - L_{\text{hypoxia}})}) \qquad (2.12) \\
&= 16.5(x - L_{\text{hypoxia}}) - 21.7v(1 - e^{\frac{1}{1.315 * v}(x - L_{\text{hypoxia}})})
\end{aligned}
$$

We can now see that there are two terms in the equation, the first one is the oxygen concentration bounded by the PDMS, and the second one is the diffusion term. The plot of this equation is shown in Figure 4.2B. The equation shows that the gradient at downstream of the channel is closer to a straight line rather than an exponential curve.

Finally, we also give a quick estimation of the reoxygenation in the cyclic hypoxia process. We still assume the concentration profile inside the PDMS is a straight line for everywhere and every time.

$$
\begin{aligned}
J_{ap} &= D_{\text{pdms}} \frac{\text{solubility}_{\text{pdms}} - c_{\text{pdms}}(0)}{L_{\text{eff}}} \\
\Rightarrow \frac{\partial c_{\text{medium}}(0)}{\partial t} &= \frac{1}{L_{\text{eff}}} [\frac{D_{\text{pdms}}}{L_{\text{eff}}} (\text{solubility}_{\text{pdms}} - c_{\text{pdms}}(0))] \\
\Rightarrow c_{\text{pdms}}(t) &= \text{solubility}_{\text{pdms}} (1 - e^{-\frac{2D_{\text{pdms}}}{L_{\text{eff}}} t}) \\
&= 1.62 * (1 - e^{\frac{t}{3610}})
\end{aligned}
\tag{2.13}
$$

As the time constant about an hour, this is why the PDMS shows the damping behavior in Figure 4.5.

# Chapter 3 Materials and methods

## 3.1 The microfluidic chip

### 3.1.1 Microfluidic chip design

The microfluidic chip shown in Figure 3.2 contains two layers. The top layer is called the hypoxia layer. It contains two inlets for pyrogallol and NaOH respectively, and a mixing region for mixing two reagents. The diameter of the meandered channel is 400 $\mu$m. The length and the width of the hypoxia channel are designed from simulation results (Section 4.1.1). The dimensions of the rectangular that the hypoxia channel formed are 10 mm in length and 16 mm in width. The meandered shape of the hypoxia channel is adopted instead of a wide channel mainly due to two reasons: first, ensuring mixing and flow evenly. While wide and straight channels may not secure every part of the channel is refreshed with new pyrogallol and NaOH continuously. The second reason is for an easier fabrication process. The membrane beneath, the cell culture layer, will be too fragile to peel off from the mold during the fabrication process if there is not enough contact surface between the hypoxia layer and the cell culture layer. Some design their hypoxia channel beside their cell culture channel can have an easier fabrication process, instead of making two layers of the chip, however, this can only generate a relatively small region of hypoxia in their chip. Hence, we adopted the design that the hypoxia channel is placed on the cell culture channel, although this leads to another problem the channel will be bent due to the pressure difference between the hypoxia channel and cell culture channels. The details are discussed in Section 4.1.1.

The second layer is called the cell culture layer. We named the widest channel A and then B, C, and D in order. The width of each channel is 4 mm, 2 mm, 1 mm, and 0.5 mm respectively. These values are adopted for the consideration of glass slide dimension and the wall shear stress generated with a flow rate of 30 $\mu$L/min is 2.5, 5, 10 and 20 dyne/cm$^2$, which are estimated through the equation $\tau = \frac{6\mu Q}{wh^2}$ [29] and simulation, and these values are compatible with those in the human vein [58]. For each channel, the width of the midstream is 2.5 mm, the dimension limited by the fabrication process (channels can collapse if they are too wide) and glass slide width, to lower the flow rate to generate hypoxic conditions. Although channel A has a channel width of more than 2.5 mm, we still alter the width in the midstream due to symmetric reasons. The channel order in this design is arranged to make the oxygen profile more symmetric within the channel (Figure 4.3).

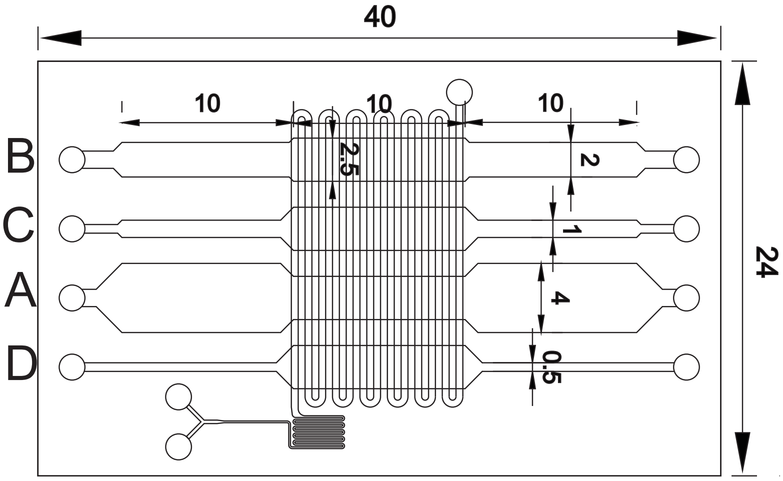

Figure 3.1 Dimensions of microfluidic device (unit: mm). The bigger numbers mark the dimension of hypoxia channel, while the smaller numbers mark the dimension of culture channels.

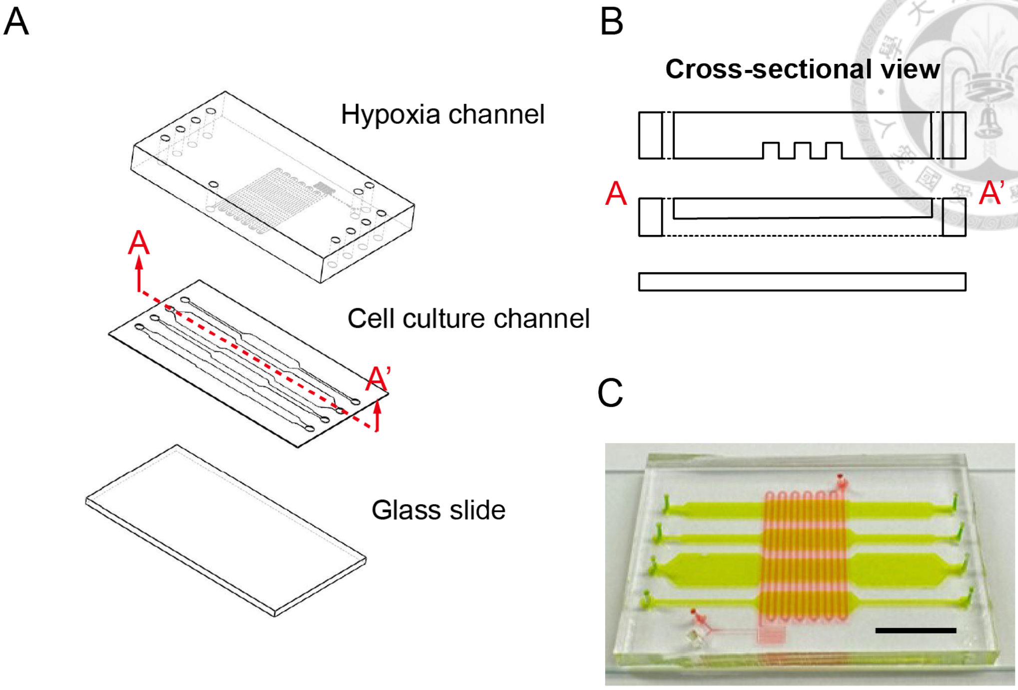

Figure 3.2 (A) The explode-view drawing of the device. (B) The cross-sectional view of the microfluidic device. (C) The photo of the microfluidic device. The scale bar is 10 mm.

### 3.1.2 Microfluidic chip fabrication process

First, the molds of two layers are made by photolithography. After that PDMS (Sylard-184, Dow Corning) is prepared with the 10:1 base to agent ratio. PDMS is then degassed and used as the material of the chips. The lower layer is made by spin coating (500 RPM 10s → 800 RPM 40s → 500 RPM 10s) a thin membrane of PDMS on the lower layer mold. The thickness of the membrane is measured by cutting the chip in the vertical direction. The upper layer is simply made by pouring 60g PDMS on the mold. The PDMS will then be cured in 60°C for 4 hours. The upper layer channel is then peeled from the mold and permanently bonded to the lower layer with plasma bonding. Finally, the combined two-layer chip is again bonded to the glass slide by plasma bonding (Figure 3.3).

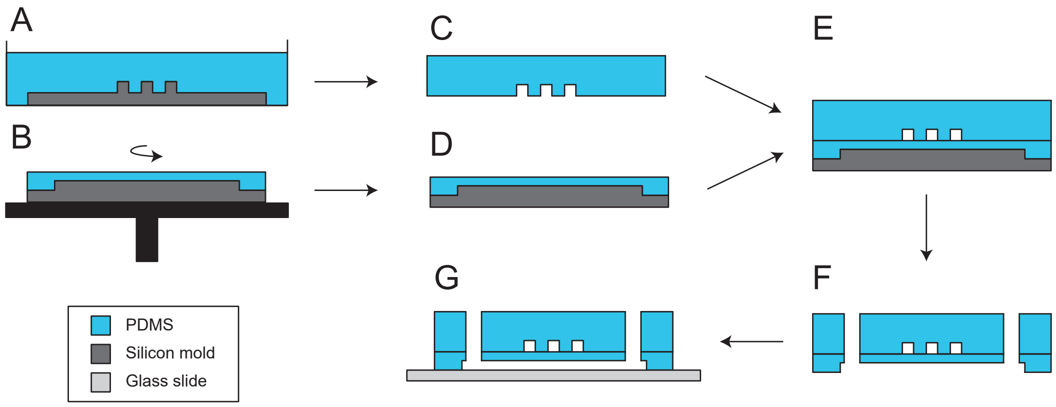

Figure 3.3 The fabrication process of the PDMS chip. (A) The PDMS precursor is poured into a Petri dish with a hypoxia channel mold inside. (B) A thin layer of PDMS is spin-coated on the culture channel mold. (C) The PDMS is peeled off after PDMS is cured. (E) The hypoxia channel parts are bonded to the surface of the culture channel through an oxygen plasma machine (F) The PDMS is then peeled off from the silicon mold and punched. (G) The PDMS is bonded to a glass slide using an oxygen plasma machine.

## 3.2 Cell culture

Human umbilical vein endothelial cells (HUVECs) and culture medium (CC-3162) are bought from Lonza. The cells are cultured inside T75 flask (Falco) and placed in an incubator with 37° and 5% $CO_2$.

### 3.2.1 Cell passage

After HUVECs in the T75 flask reach confluency higher than 80%, the cells are ready to be passaged. The culture medium in the flask is first removed, and then the cells are rinsed with 5mL of Dulbecco's phosphate-buffered saline (DPBS, Gibco). 2 mL trypsin-EDTA (Thermo Fisher 25200-056) is added to incubate with cells for 3 minutes to detach the cells from the surface. 5 mL of culture medium is then added to the flask to neutralize the trypsin. The solution is then centrifuged with 1000 RPM for 4 minutes, and the supernatant is removed. We do this twice to ensure trypsin is removed properly. The resulting cells are now resuspended into the culture medium and equally distributed to new flasks for passage. Finally, each flask will be filled with culture medium up to 8 mL.

### 3.2.2 Cell freezing

After the cells grow to nearly full confluency, cell freezing can be performed to keep cells for future use. By collecting cells in the same way, every $10^6$ cell can be stored in a single tube containing 10% DMSO. The distributed cells are then put in a cryo-freezing container in a -80° refrigerator for slowly freezing. After a day, the cells are moved to a liquid nitrogen tank for long-term storage.

### 3.2.3 Cell seeding

Before cell seeding, the chips will be sterilized by UV light for 2 hours. The channels are first filled with fibronectin (FC010; F0895, EMD Millipore, Billerica MA), which is

doi:10.6342/NTU202402333

diluted in to 0.1 mg/ml, and placed into an incubator for later use. The cells in the flask are collected by the method mentioned in 3.2.1. The concentration of cell suspension is set to be $4 \times 10^6$ cells/80 $\mu$L. 8 $\mu$L of cell suspension is then injected into each channel. After 30 minutes of incubation, the pipette tips containing 200 $\mu$L medium are added to one side of each of the channel inlets, while the other side is plugged with another empty pipette tip. With this matter, the culture medium will infuse the channels through gravity. This process is repeated twice to ensure fibronectin is eliminated, because HUVECs are sensitive to fibronectin. The seeded chips are kept in the incubator overnight for further experiments.

## 3.3 Hypoxic condition generation

In this research, we aim to produce an oxygen gradient between 0% to 13%, which corresponds to the oxygen concentration in artery and vein. Pyrogallol (benzene-1,2,3-triol, $C_6H_6O_3$) is chosen as an oxygen scavenger. Pyrogallol is a natural phenolic compound found in different crops and fruits such as Litchi and Indian gooseberries [23]. Alkaline solutions of pyrogallol can absorb oxygen, so we chose NaOH to create an alkaline environment. The mechanism of oxidation of pyrogallol is complicated because not only a single kind of molecule is produced (Figure 3.4). By injecting both pyrogallol with a concentration of 10 mg/ml and 1M NaOH with a flow rate of 2 $\mu$L/min into the hypoxia channel, the hypoxic conditions can be generated in our chip.

## 3.4 Oxygen level measurement in microfluidic devices

### 3.4.1 Fluorescence lifetime imaging microscopy

Fluorescence lifetime imaging microscopy (FLIM) is a technique that can determine the lifetime of incident fluorescence. By knowing the value of the lifetime of an

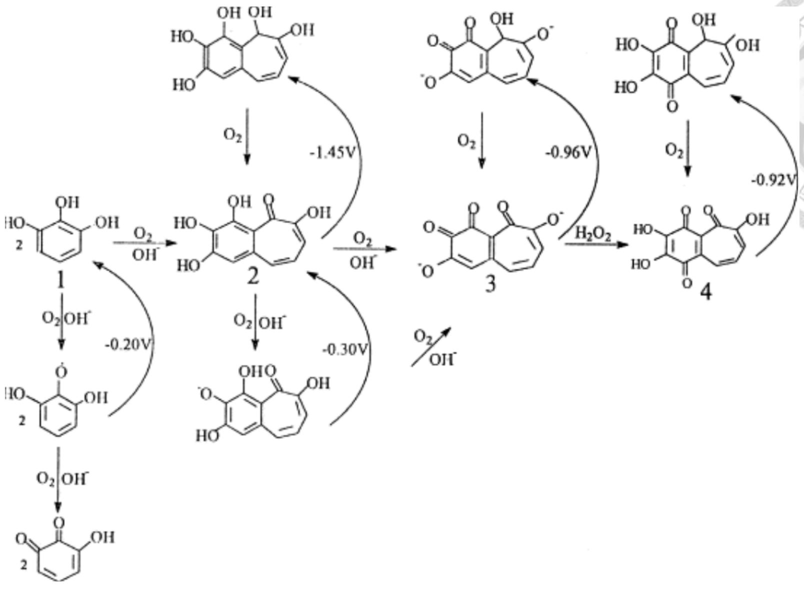

Figure 3.4 Auto-oxidation of pyrogallol with oxygen [25].

oxygen-sensitive dye, we can calculate the oxygen concentration through the Stern-Volmer equation (Equation. 3.1) [76].

$$\frac{\tau^0}{\tau} = 1 + K_q[O_2] \tag{3.1}$$

$\tau$ is the lifetime of the incident fluorescence dye, and $\tau^0$ is the lifetime of the incident fluorescence dye when the dye isn't bind to the oxygen, and $K_q$ is the quenching coefficient. These values in our experiments using Tris(2,2'-bipyridyl)ruthenium(II) (RTDP) are $\tau^0$ = 582.84 ns, $K_q$ = 2.0658/($O_2$ percentage in air=20%) , for example, for lifetime $\tau$ = 381 ns the oxygen concentration is 0.19 = 19%.

### 3.4.2 Oxygen sensor

The dissolved oxygen sensors are bought from PreSens. The oxygen measurement is set up as the photo (Figure 3.6). The sensors are plugged into the PDMS channel by punching a 2 mm hole in the channel. The fluorescence material inside the sensor is excited by a laser delivered through the optical fiber. After that, the reflected light will be transmitted back to the reader with phase and intensities will be recorded just like the working principle of FLIM. Those sensors are pre-calibrated by the manufacturer and then can monitor the oxygen level of a single point within the channel. The measurements are read out through PreSens Measurement Studio. The measurements are finally exported as an XLSX file for analysis.

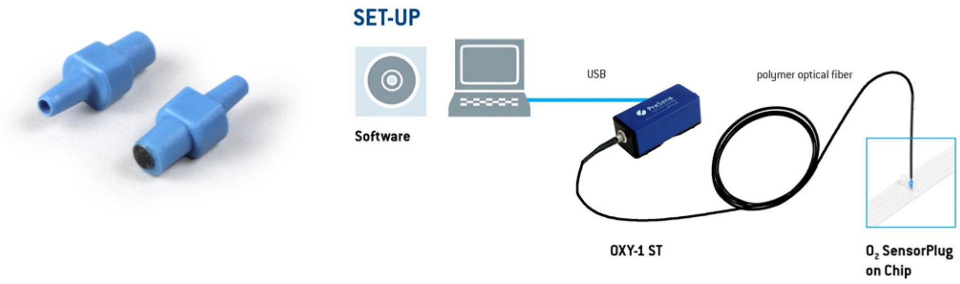

Figure 3.5 (A) Sensor plugs and (B) System setup (source: PreSens).

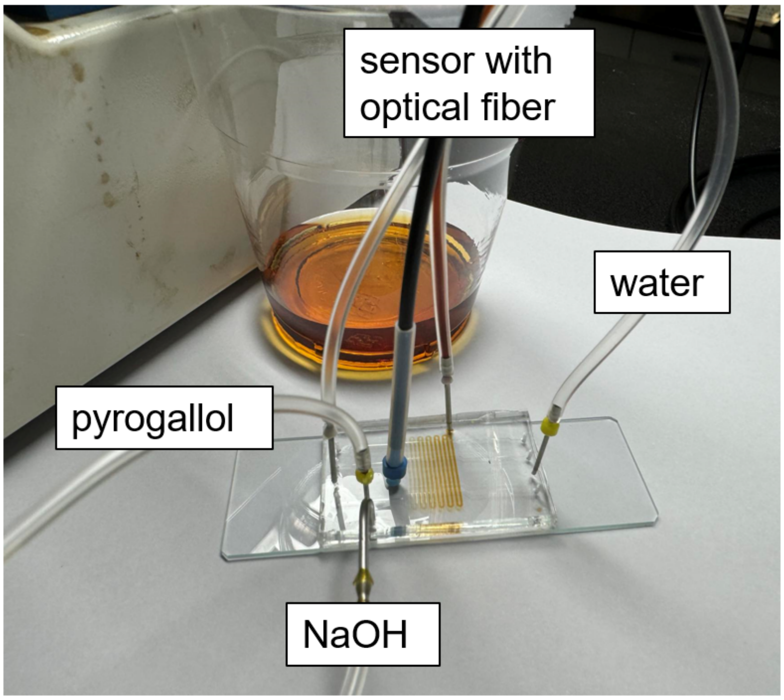

Figure 3.6 The oxygen level measurement setup of PreSens sensor plugs.

## 3.5 System setup

Two syringe pumps (Fusion 200, Chemyx; GOO-SPM-1, Infusetek) are used in our system, one is for pyrogallol and NaOH injection, and the other is for culture channel infusion (Figure 3.7A). The concentration of NaOH is 1M, while the concentration of pyrogallol is 10 mg/ml in the experiments. Both of the flow rate of the NaOH and pyrogallol are 1 $\mu$L/min. For the cyclic hypoxia experiments, the flow of pyrogallol will stop for 60 minutes every 60 minutes while the flow of NaOH remains.

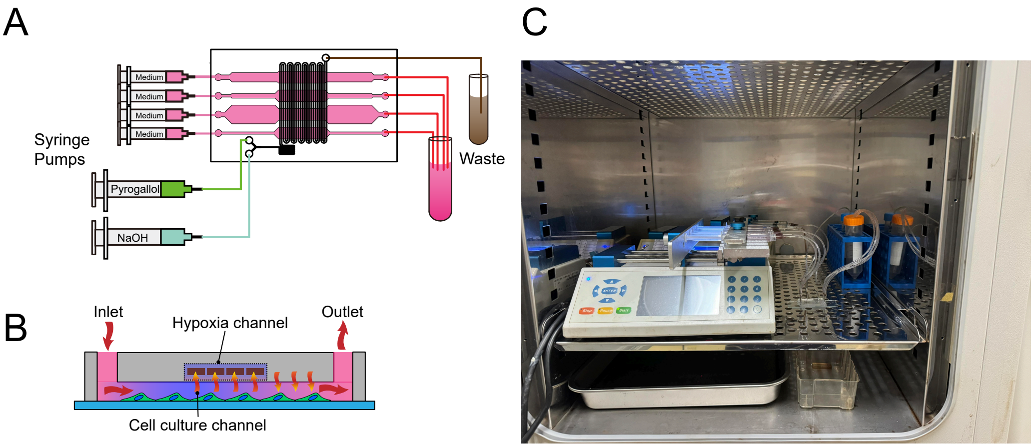

Figure 3.7 (A) System schematic (B) Working principle of microfluidic chip (C) Photo of system setup.

## 3.6 Cell imaging

The cells are imaged by inverted fluorescence microscopy (IX-73, Olympus), and the images are captured by a charged-coupled device (ORCA-Flash 4.0 V2, C11440-22CU, Hamamatsu) with a 10x objective lens (UPlan F1, N.A.=0.30, Olympus) and phase ring (Ph1/PhC, Olympus). The stage of the microscope is controlled by a motorized stage (Marzhauser, MFD-2) so that the whole image can be stitched by moving the stage and the calculation of the Olympus software.

## 3.7 ROS measurement in cells

The ROS measurement in cells is done by using the DCFDA / H2DCFDA - Cellular ROS Assay Kit (ab113851). After DCFDA / H2DCFDA / DCFH-DA / DCFH diffuses into cells, it is then trapped in cells due to the deacetylation by the enzymes inside the cells. These molecules can be oxidized by ROS into 2’, 7’ −dichlorofluorescein (DCF), which is highly fluorescent and is detected by fluorescence spectroscopy with excitation/emission at 485 nm / 535 nm. The staining protocol is stated in Section 4.3.1. The concentration for staining is 20 $\mu$M. The exposure time is 400 ms.

## 3.8 NO measurement in cells

The NO measurement in cells is done by using the DAF-FM diacetate (d23844, Invitrogen). The working principle is very similar to DCFDA/ H2DCFDA, and the excitation/emission wavelengths are at 495 nm / 515 nm. The staining protocol is stated in Section 4.4.1. The exposure time is 1 s with 4x4 binning.

## 3.9 Image processing

### 3.9.1 Bright-field image processing

The morphology analysis is based on the bright-field images of cells. Using bright-field images for the morphology analysis process has the advantage of convenience and is not being influenced by the fluorescence intensities. Here we used a hybrid processing pipeline of deep learning model and CellProfiler, which is inspired by CellProfiler official documents. The bright-field images are first cropped manually so that the center region of each channel is selected. After that, each piece is inputted to a trained U-Net [62]. The U-Net (Figure 3.8) is trained by a dataset containing 7 $512 \times 512$ bright field images that are labeled manually (Figure 3.9). Then the model is trained by utilizing data augmentation including rotation within $\pm 10^\circ$ and flipping. The optimizer adopted is Adam with a learning rate=0.005 and exponential learning scheduler with a decay rate=0.99 per epoch. The training batch size is 4 and the total training epoch is 100. The loss function is binary cross-entropy loss. The bright-field images are cropped in to $512 \times 512$ in order to be fed in U-Net model. If a cell lies at the boundary of the cropped boundary, the discontinuous of U-Net output of that cell is observed. Therefore, we chose to use the center of the output only. To achieve this, The cropping area is moved 256 pixels every time, and the area at the boundary of the original image is padded by 0 to fulfill the input size. After the U-Net outputs the results of semantic segmentation, the outputs are cropped into 10 segments along the x-axis of the channel. Each segment is then processed by the open-source software CellProfiler [8] with the pipeline listed below (Figure 3.12A). In the IdentifyPrimaryObject module, the diameter is set to be between 20-80, three-classes thresholding is used, and the local suppress maximum is 30.

doi:10.6342/NTU202402333

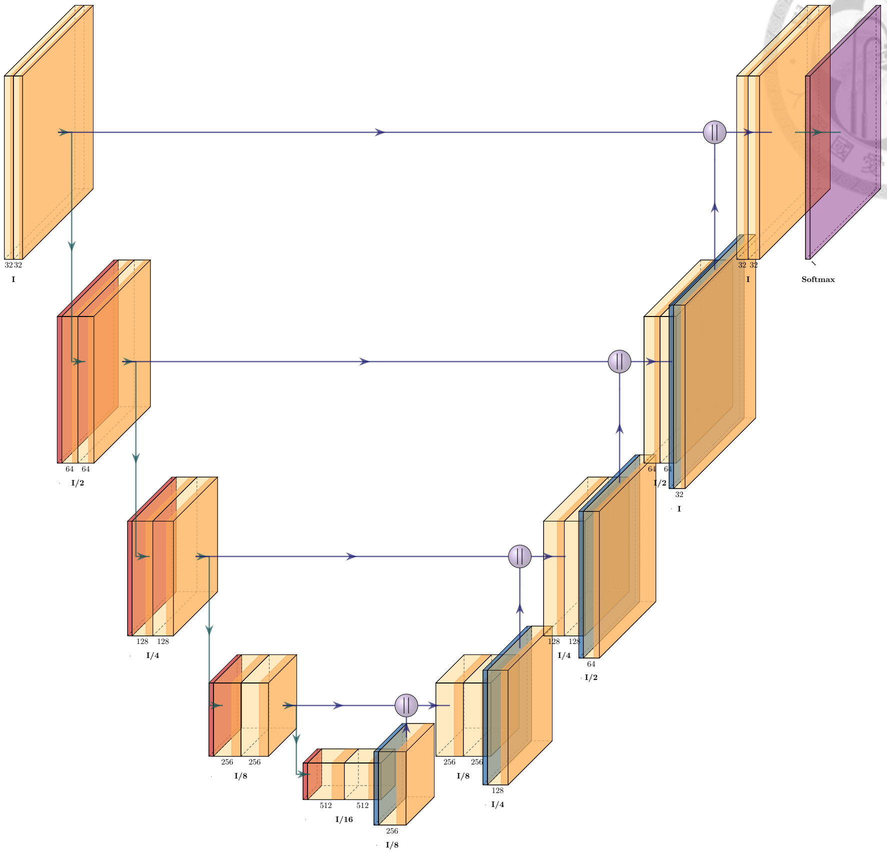

Figure 3.8 U-Net model structure. The filters inside each convolution layer are 5 ×5 with stride=2. (source: PlotNeuralNet.git)

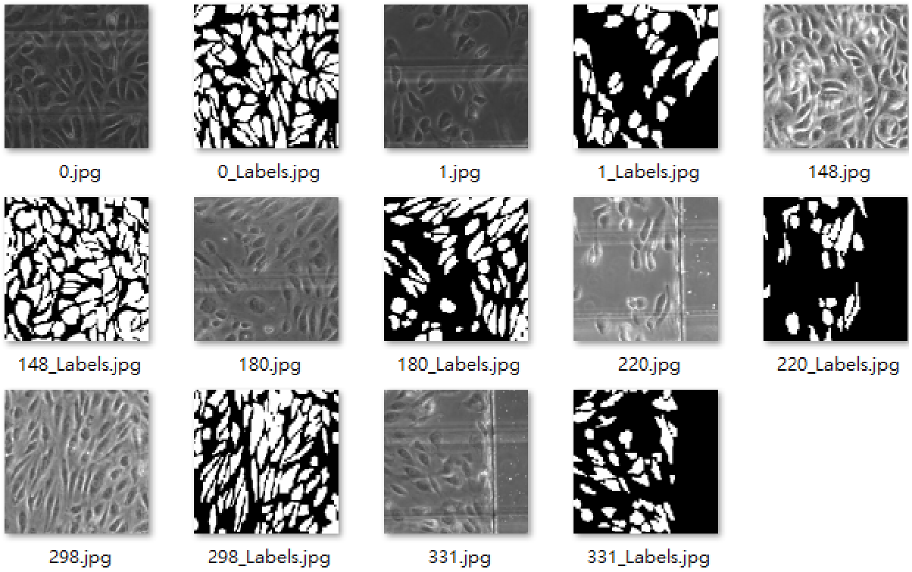

Figure 3.9 The training set for U-Net.

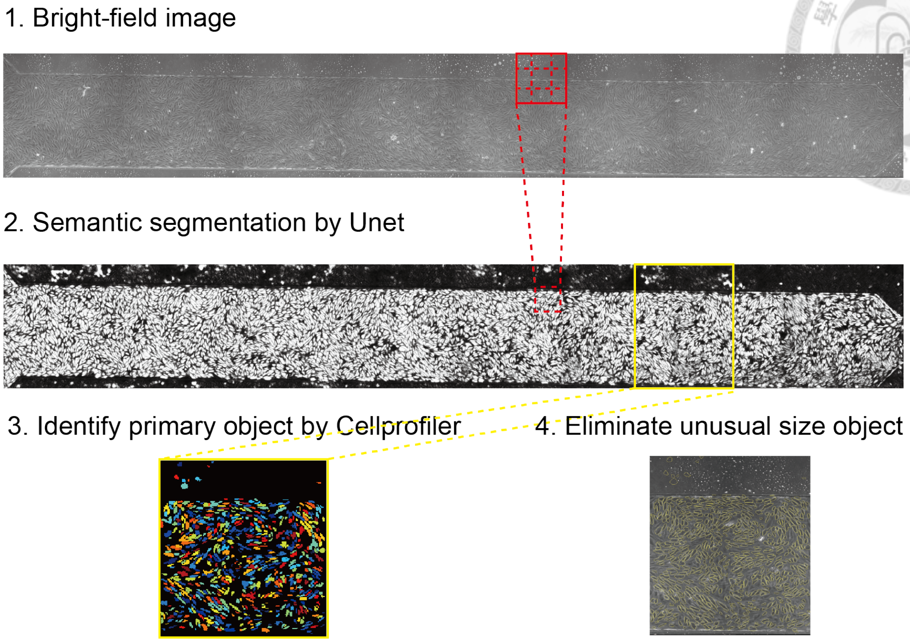

Figure 3.10 Bright-field image processing.

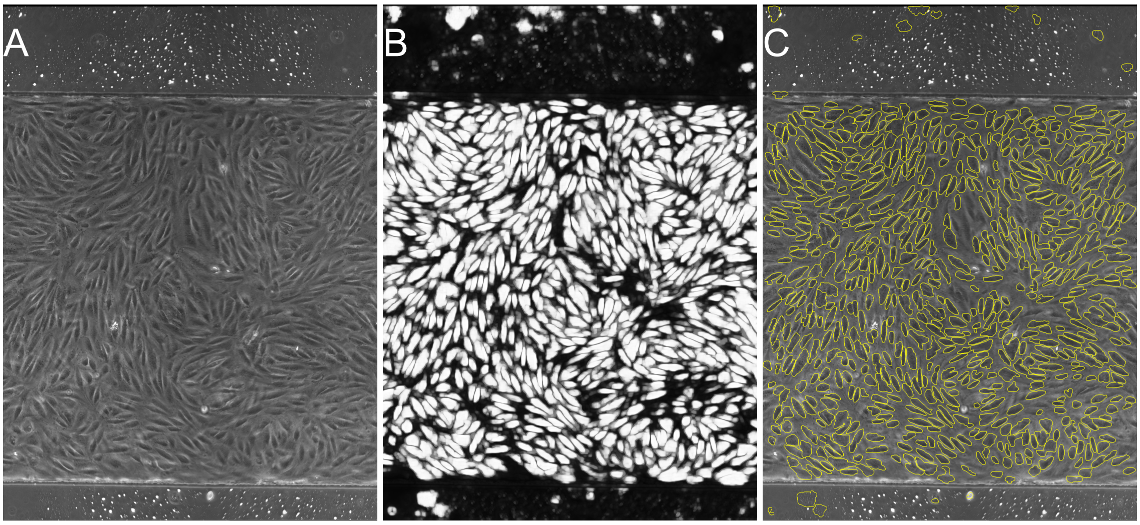

Figure 3.11 The demonstration of cell segmentation utilizing U-Net and CellProfiler. (A) Cropped image. (B) The output of U-net. The intensities are the probability, therefore the boundaries of cells are gray. (C) The final segmentation is done by CellProfiler, where the watershed algorithm is used. The final output is overlaid on the original image.

### 3.9.2 Fluorescence image processing

The fluorescence images are processed by Otsu’s threshold algorithm to determine which pixels are bright enough to belong to cells. The images are first segmented into 20 pieces just as what is done in bright-field image analysis so that each segment has different threshold values because appropriate threshold values can vary due to different fluorescence intensities over the image. To eliminate noises that have extremely high values, the algorithm to eliminate it is to recalculate the threshold value if the pixels higher that threshold is less than 10%. Those pixels will be set to be the threshold value and calculate the threshold value again to get a lower threshold value.

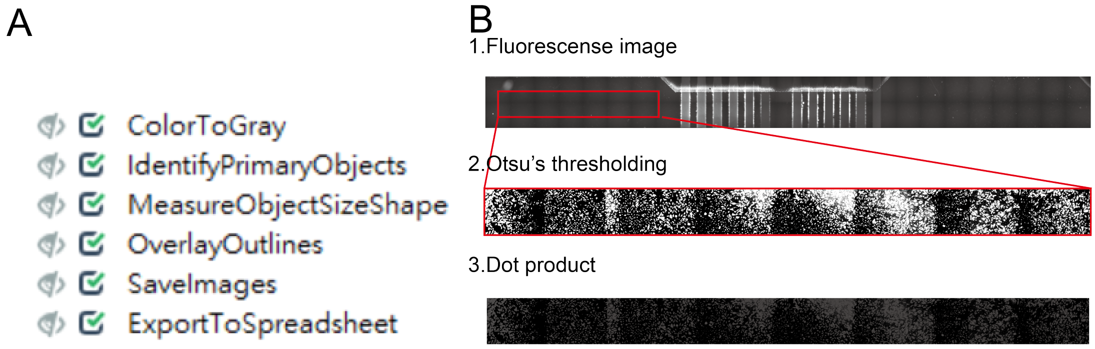

Figure 3.12 (A) Pipeline used in CellProfiler. (B) Fluorescence image processing.

# Chapter 4 Results and Discussion

## 4.1 Simulation

The simulation is done by using COMSOL 6.2 with finite elemental analysis. The fluid simulation is done by a laminar module. The hypoxic conditions are simulated by diluted species transportation and fast irreversible surface modules, where we assume that pyrogallol and NaOH is not limited reagents and react to oxygen very quickly. Henry's law is implemented by split conditions in COMSOL, which makes the constraint at the boundary that $J_{12} = J_{21} = D_1 \frac{\partial c_1}{\partial n} = D_2 \frac{\partial c_2}{\partial n}, \frac{c_1}{\mathrm{s}_1} = \frac{c_2}{\mathrm{s}_2}$, where $c$ is the concentration of oxygen in certain substrates, n is the normal vector at the interface, and s is the solubility. The parameters used are listed in the following table [52][77][7].

Table 4.1: Parameter values used in simulation

| Paramater | Value |
|---|---|
| oxygen solubility of water | 0.22 mol/m$^3$ |
| oxygen solubility of PDMS | 1.62 mol/m$^3$ |
| oxygen diffusion coefficient in medium | $1.9\times 10^{-9}$m$^2$/s |
| oxygen diffusion coefficient in PDMS | $4\times10^{-9}$m$^2$/s |
| membrane thickness | $6\times 10^{-5}$ m |
| flow rate in cell culture channel | 30 $\mu$L/min |
| flow rate in hypoxia channel | 2 $\mu$L/min |
| dynamic viscosity | 1.01 mPa $\cdot$ s |

### 4.1.1 Basic fluid characteristics

First, we show the basic fluid characteristics inside the channels. The streamline, wall shear stress, and pressure are shown in Figure 4.1A, Figure 4.1B, and Figure 4.1C. We can see the shear stress generated in the channels are about 2.5, 5, 10, 20 dyne/cm$^2$ in channels A, B, C and D respectively, which agree with the equation $\frac{6\mu Q}{wh^2}$. The pressure inside the channel is around 500 to 2500 Pa at upstream of each channel. Although a lot

doi:10.6342/NTU202402333

of research argue that hydrostatic itself can affect endothelial cells even when the shear stress doesn’t exist, we think the effect of hydrostatic pressure can be ignored because even when hydrostatic pressure reachs 40 Torr (5332 Pa), the effect is subtle [45]. The pressure differences between the overlap region of the cell culture channel and hypoxia channel are about a few Torr. The pressure differences can cause the membrane bending thus leading to cell death, this is discussed in Section 4.5.1.

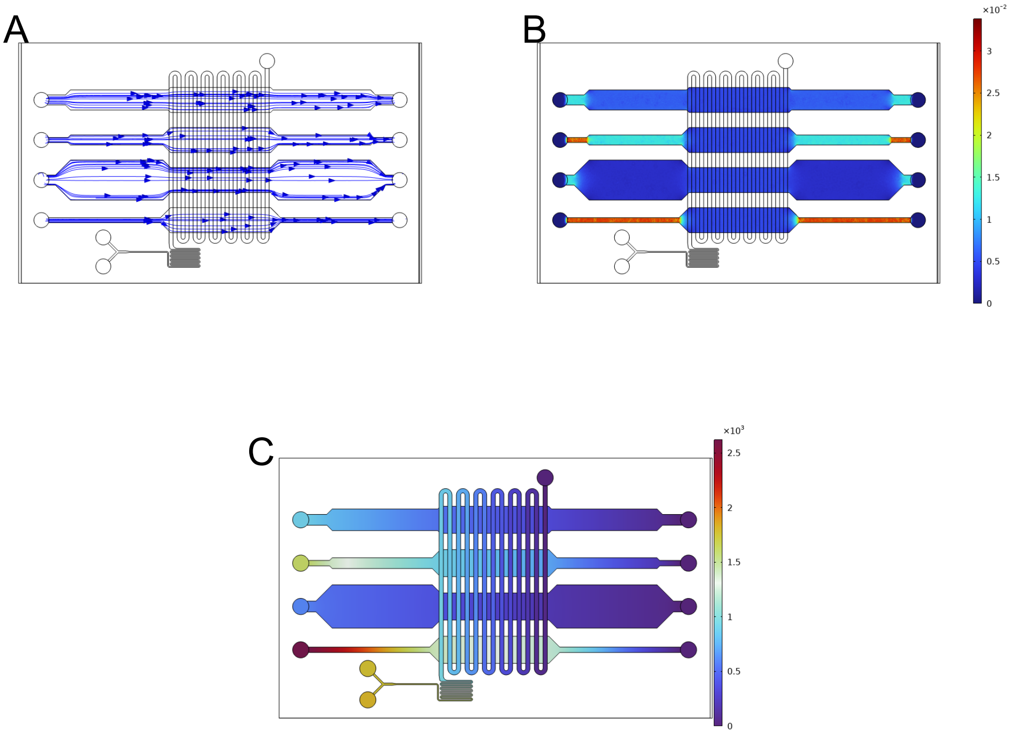

Figure 4.1 (A) Streamline of the flow. (B) Wall shear stress at the plane z = 0 $\mu$m. The unit is dyne/cm$^2$. (C) The pressure generated in channels. The plot is at the plane z = 25 $\mu$m (for cell culture channel) and 85 $\mu$m (for hypoxia channel). The unit is Pa.

### 4.1.2 Oxygen microenvironment establishment

We can establish both spatial oxygen gradient and temporal oxygen oscillation in our system. The spatial oxygen distribution is determined by the equilibrium of oxygen depletion using pyrogallol and oxygen diffusion in PDMS and water. The fresh medium first loses its oxygen when flowing beneath the hypoxia channel. With the oxygen permeability of PDMS, oxygen reacts to pyrogallol inside the hypoxia channel thus causing the instant oxygen concentration drop. After passing through the hypoxia channel, the oxygen are able to diffuse back to the channel. Therefore, the oxygen gradient is established.

#### 4.1.2.1 Constant oxygen gradient

Recall the Equation 2.12 and Equation 2.9. The comparison of these two equations is plotted below. We can see that the oxygen gradient becomes less sensitive to the flow velocity after fixation.

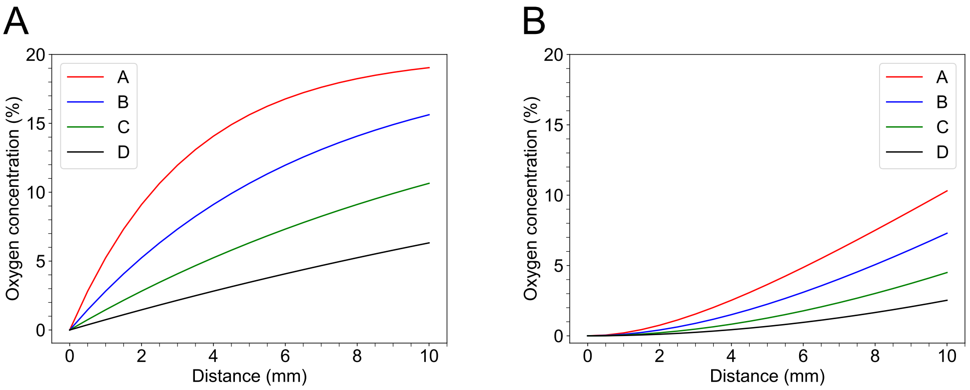

Figure 4.2 The downstream oxygen profile (A) without (B) with the assumption of a linear gradient in PDMS.

The constant oxygen gradient generated in the channel is further simulated by COMSOL as parameters described in Section 4.1. In the simulation result in Figure 4.3, we can observe that the oxygen level is dramatically decreased after passing the hypoxia region. The oxygen level gradually recovered after exiting the hypoxia region.

The experimental oxygen concentration is then verified by FLIM. FLIM can easily show the spatial distribution of oxygen in microfluidics. The measurement method of FLIM is described in Section 3.4.1. The result is shown in Figure 4.4. We can see that

doi:10.6342/NTU202402333

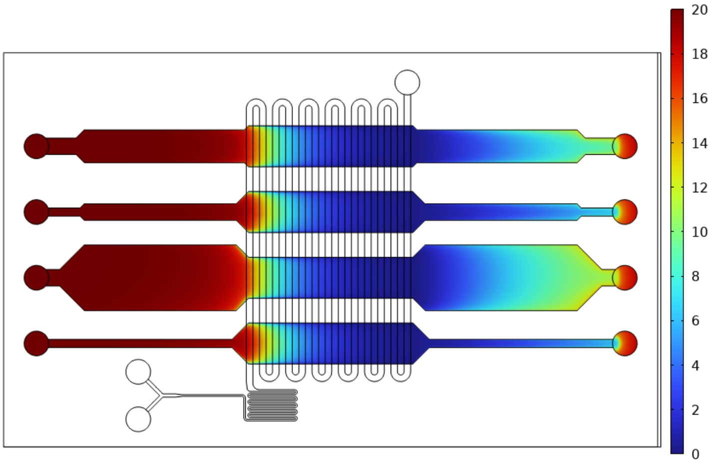

Figure 4.3 The oxygen concentration at z= 0 mm plane of the center of each channel.

the slope of the oxygen gradient in each channel is close to a straight line, which agrees with the assumption in Figure 4.2B and the simulation results. Therefore, we can claim that our device can decouple shear stress and oxygen gradient generation to some degree, this can help us to generate the desired microenvironment easier.

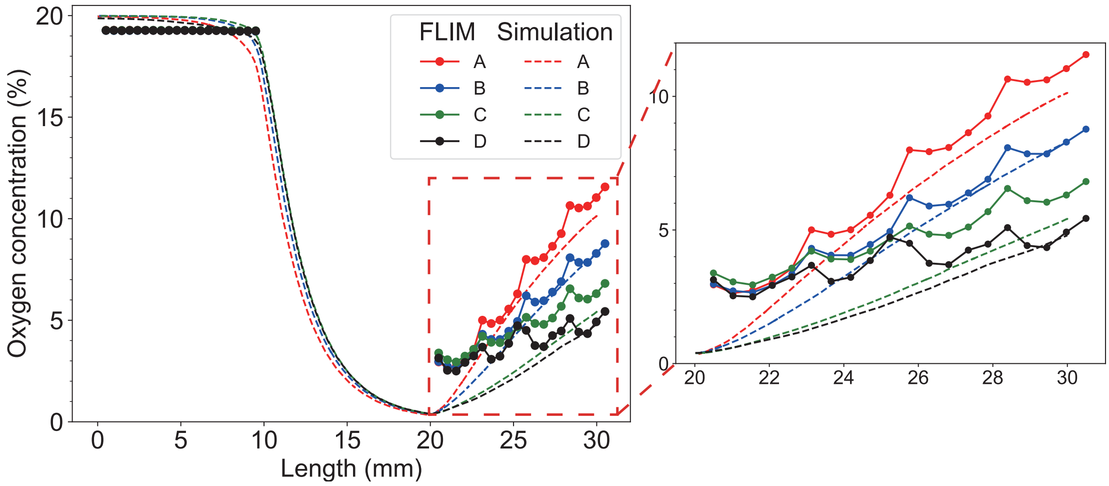

Figure 4.4 The measurement of FLIM. The lifetime of the intensities has been converted to oxygen concentration in this plot. The dot lines are the simulation results.

#### 4.1.2.2 Cyclic oxygen gradient

To investigate the microenvironment such as those in tumors, cyclic hypoxic conditions need to be generated in the microfluidic system. Here, we propose a method to achieve this. The cyclic oxygen gradient can be generated by stopping the flow of pyrogallol, while NaOH is still flowing to flush out the pyrogallol left in the hypoxia channel. This will let the oxygen in the ambient environment diffuse into PDMS and then the oxygen absorption capability will be lowered and the oxygen level in the culture channel will increase. We measured the oxygen concentration at the position right beside the hypoxia region of the widest channel to measure the oxygen level dynamic. The sampling rate is 1/30 Hz, and the result is shown in Figure 4.5.

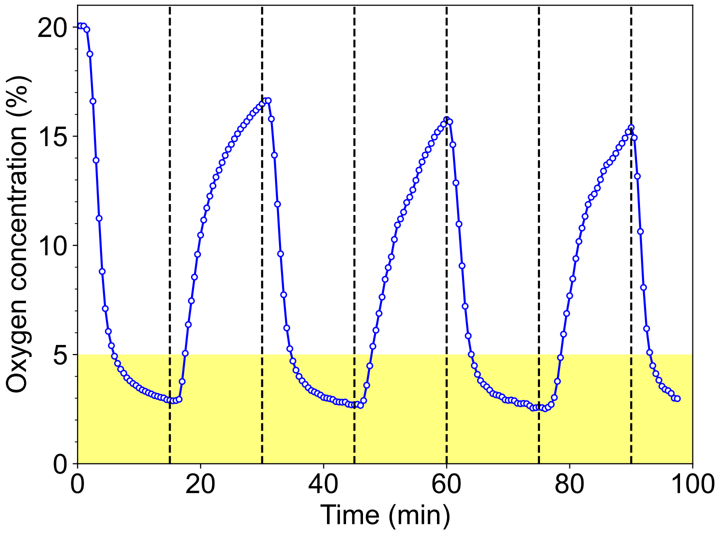

Figure 4.5 Cyclic hypoxia demonstration. The half-cycle is 15 minutes. We highlight the oxygen level is less than 5% corresponding to the oxygen level lower than physioxia in vein.

We set the half-cycle time to be 15 minutes in the demonstration due to the experiments we did before this demonstration shows 15 minutes is a suitable time for both depletion and recovery of oxygen. The dashed lines indicate the time when the flow

doi:10.6342/NTU202402333

of pyrogallol is turned off or on. The figure shows that we can generate an oxygen level oscillation between about 2.8% and 16.5% with 30 minutes per cycle in our chip. There is about a two-minute delay for the oxygen level to start to decrease or increase after the switching of pyrogallol. This indicates the time needed to flush out or fill in sufficient pyrogallol in the hypoxia channel to make the oxygen level start to change. Thus, this time can be shortened by increasing the flow rate of NaOH, however, this also increases the pressure applied to the cell culture channel. Here, we chose the flow rate of NaOH and pyrogallol to be 2 $\mu$L/min in our setup. Besides, we also observed the damping effect of PDMS. As the high solubility of PDMS, PDMS acts as a large capacitance for storing oxygen. However, the motion of oxygen inside the PDMS is diffusion-limited, so we can still successfully oscillate the oxygen level in the first cycle although the oxygen inside the PDMS isn't fully depleted. From the figure, we can also find that the oxygen consumption process is faster than the recovery process.

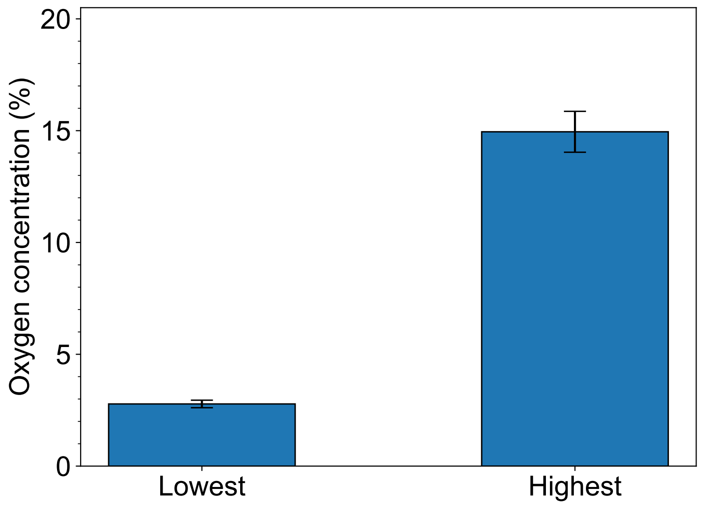

Figure 4.6 The reproducibility of cyclic hypoxia among devices (N=3). The oxygen concentration is probed in different devices to verify the stability of cyclic hypoxia generation.

We then investigate the reproducibility of cyclic hypoxia generation among different devices. By calculating the average of the lowest points and the highest points in each cycle of different devices during the same experiments, the sample standard deviation is calculated in Figure 4.6. Less than 6% variation in the oxygen level suggests the reproducibility of cyclic hypoxia generation.

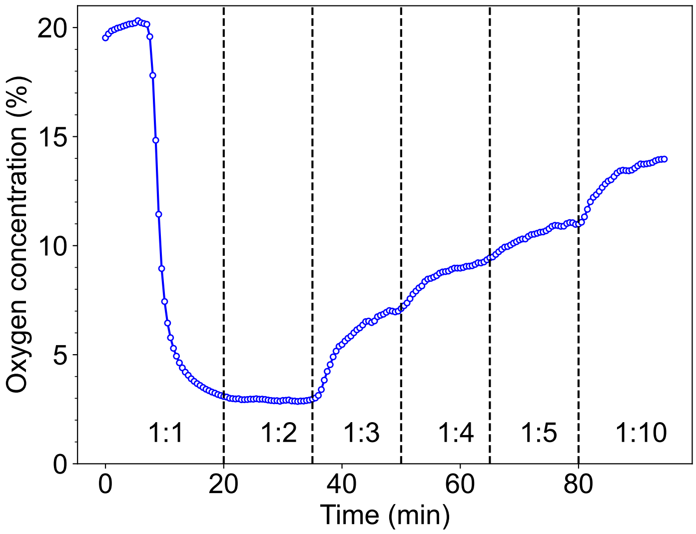

Figure 4.7 The oxygen level can be controlled by tuning the flow rate ratio between pyrogallol and NaOH.

We have demonstrated oxygen depletion can be controlled by stopping the flow rate of pyrogallol. We are curious about whether the oxygen level be set to a certain level if we tune the flow rate ratio of pyrogallol and NaOH. Figure 4.7 shows the oxygen level dynamic when tuning the flow rate of pyrogallol. We also choose 15 minutes for each section to reach a steady state. We can see the oxygen level wasn't changed when the flow rate of pyrogallol was lowered to 1 $\mu$L/min, which indicates the concentration and the flux of pyrogallol in the hypoxia is still sufficient for oxygen depletion. As the flow rate continually decreases, the oxygen level reaches a different steady state. By fixing the pyrogallol concentration and the flow rate, we demonstrated the oxygen level can be tuned by the flow rate of pyrogallol and less than 10% variation.

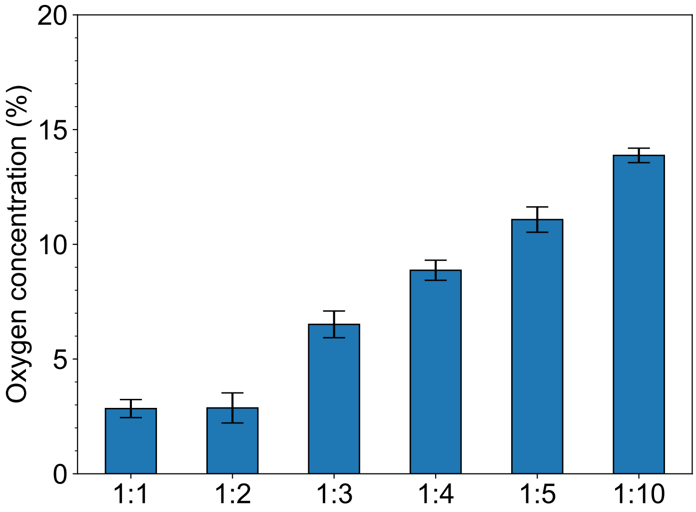

Figure 4.8 The reproducibility of oxygen level control among devices (N=3). The oxygen concentration is probed in different devices to verify the stability of cyclic hypoxia generation.

## 4.2 Cell morphology

In this research, we analyze the cell morphology as shown in Figure 4.9. The area, perimeter, and orientation are extracted from the cell image. Shape index (SI) is calculated as 4 $\pi$area/perimeter$^2$.

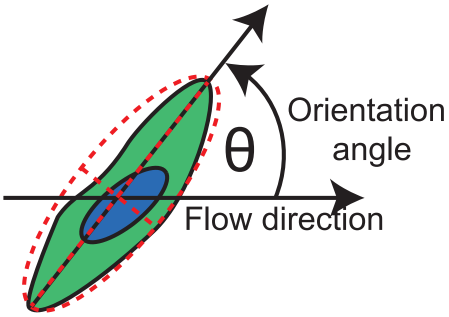

Figure 4.9 The illustration of cell morphology parameters. The fitted ellipse has the same second-moments as the cell. The major axis of the ellipse is used for orientation analysis.

### 4.2.1 Orientation changing with very short shear stress stimulation

We found that without using a pump for continuous perfusion, the cells are aligned in a certain direction due to the flow of the changing medium. This reveals that the cells can sense the flow even for a short duration of stimulation. Therefore, we have to seed our cell right before the day before experiment to prevent the cell alignment before our experiment. We used kurtosis of orientation here to measure the alignment of the cells. Kurtosis, defined as $\frac{M_4^4}{\sigma^4}$, where $M_4$ is the fourth momentum, and $\sigma$ is the second momentum. Kurtosis is a measure of tailness, that is, if the kurtosis is higher, the cells show higher collective behavior. The mean angle is not suitable to measure this behavior here because the cells are aligned in different directions in different regions just like polycrystalline. We found that the cells arranged as the shear stress is higher and the time is longer.

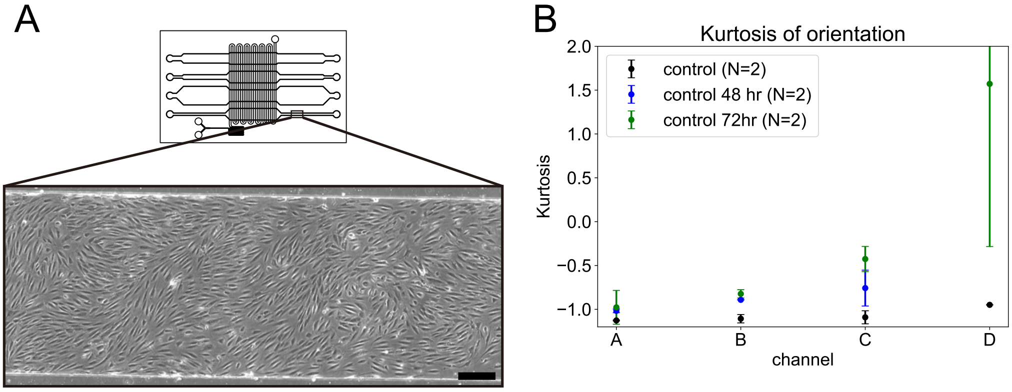

Figure 4.10 (A) Cell alignment is observed after two days of medium exchanging by gravity. The scale bar is 100 $\mu$m. (B) The kurtosis of orientation. The kurtosis is becoming higher as the width of the channel decreases and the time longer.

### 4.2.2 Cell morphology after stimulation

Because 1 hour is too short for changing cell morphology, we only analyze the morphology of 6 hours of stimulation experiments. We found that the cells in channel D are averagely aligned towards the flow for about 12° after 6 hours of shear and hypoxia. Interestingly, this effect is not seen in the cyclic hypoxia group, in which the hypoxic conditions and reoxygenation are switched every hour, and in the shear group. This result suggests that the cells arrange faster in hypoxic conditions. The kurtosis also increases by about 0.5, indicating the collective behavior of endothelial cells. We didn't observe obvious differences between the upstream and downstream regions of each condition, hence we combined them into the same condition as an N=10 experiment and got the following bar chart (Figure 4.14, 4.15, 4.16, 4.17).

doi:10.6342/NTU202402333

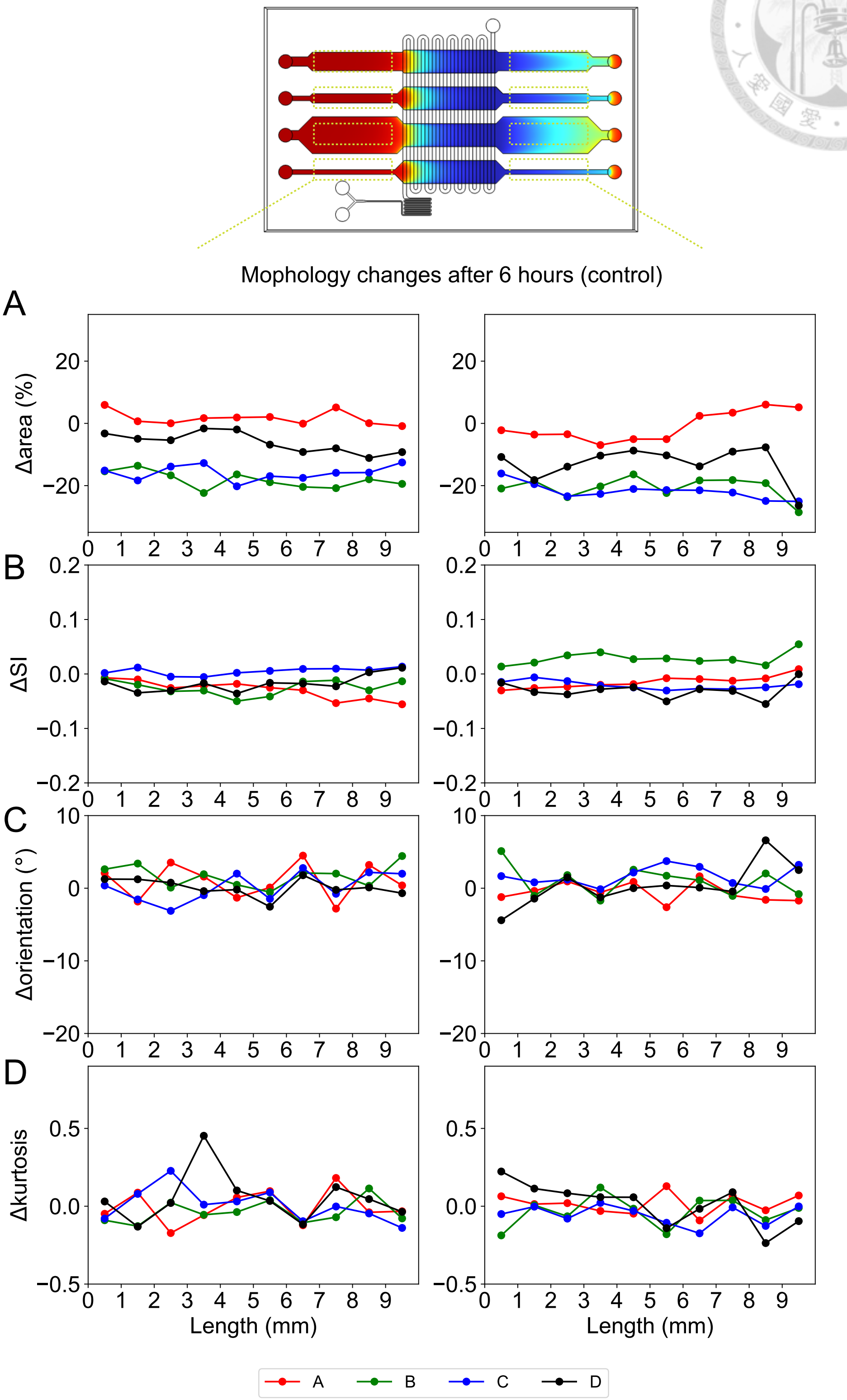

Figure 4.11 The morphology changed after 6 hours of control group (A) Area (B) Shape index (C) Orientation (D) Kurtosis of orientation.

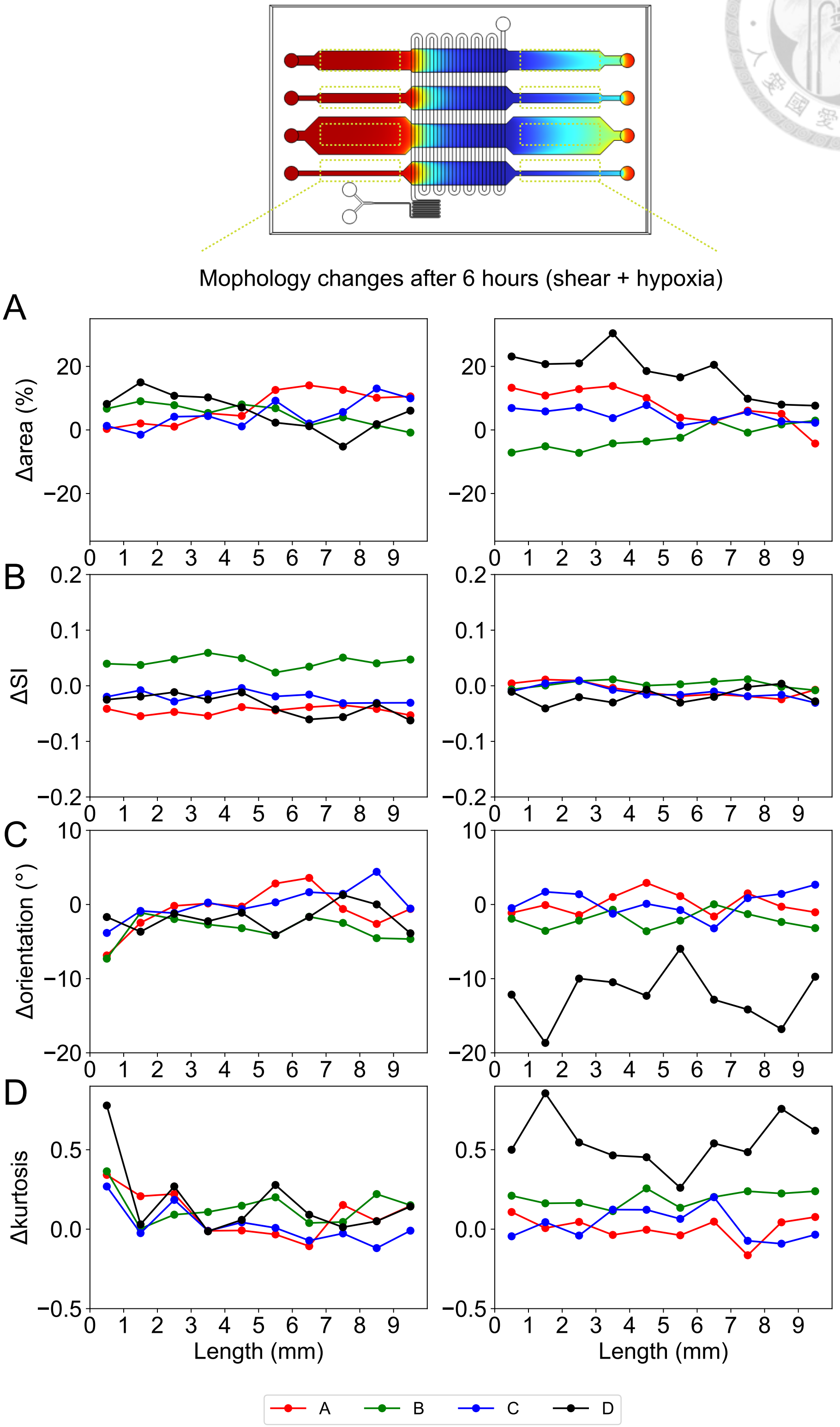

Figure 4.12 The morphology changed after 6 hours of control group (A) Area (B) Shape index (C) Orientation (D) Kurtosis of orientation.

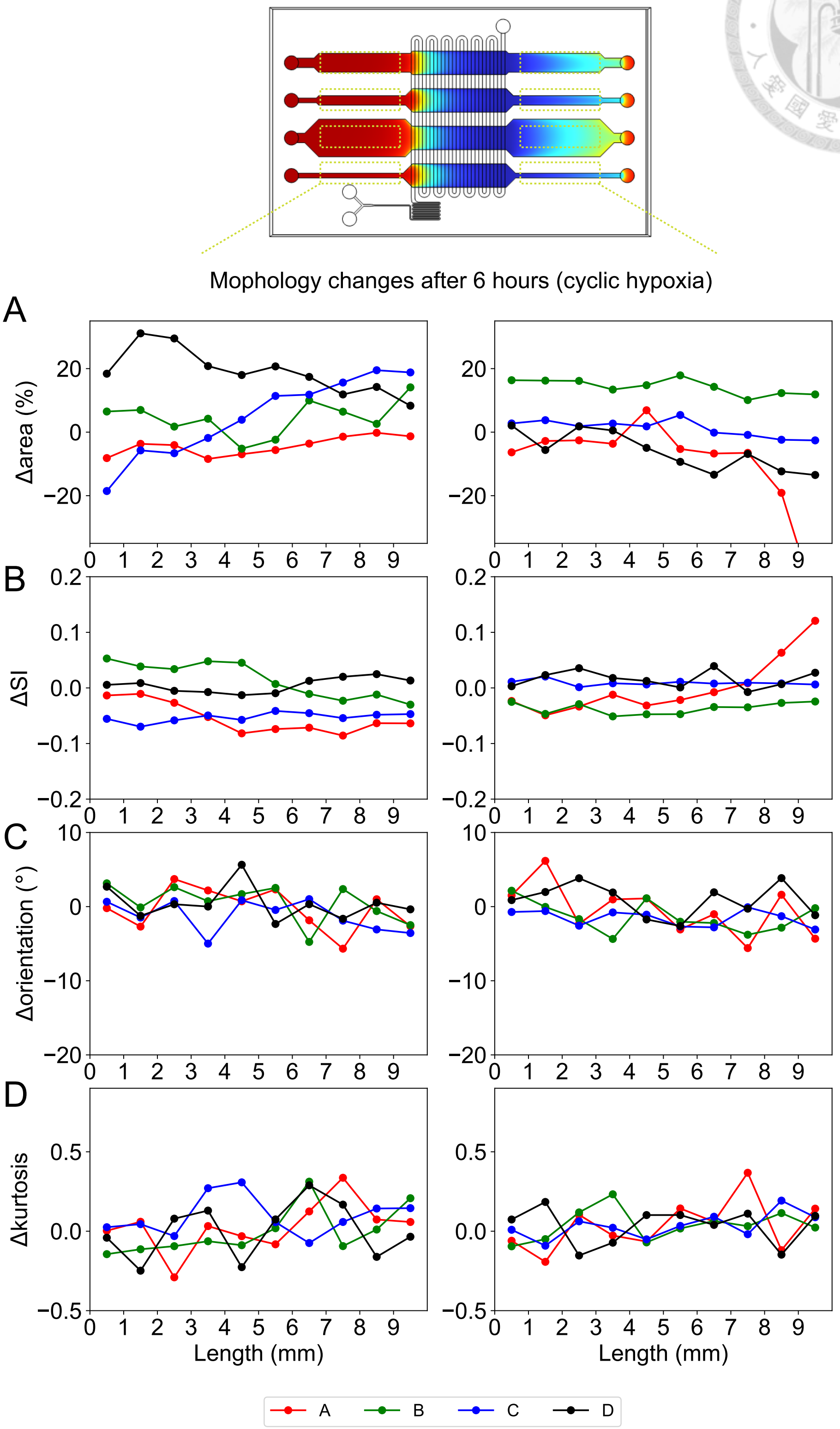

Figure 4.13 The morphology changed after 6 hours of control group (A) Area (B) Shape index (C) Orientation (D) Kurtosis of orientation.

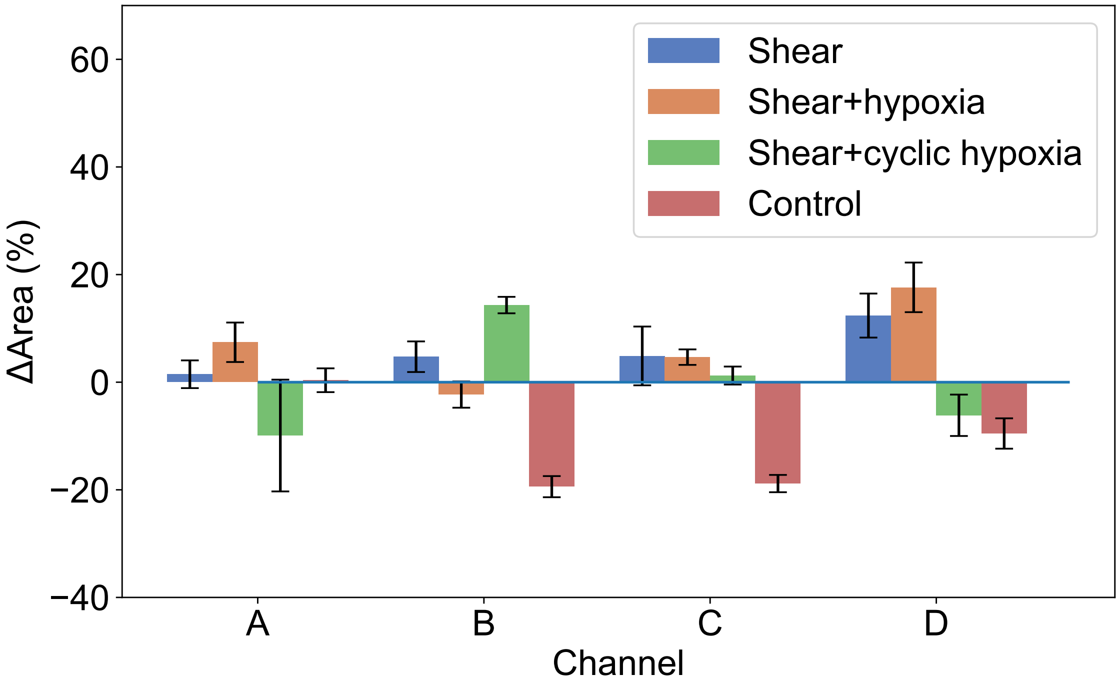

Figure 4.14 The area changed after 6 hours of different groups. The error bars represent the 95% confidence intervals.

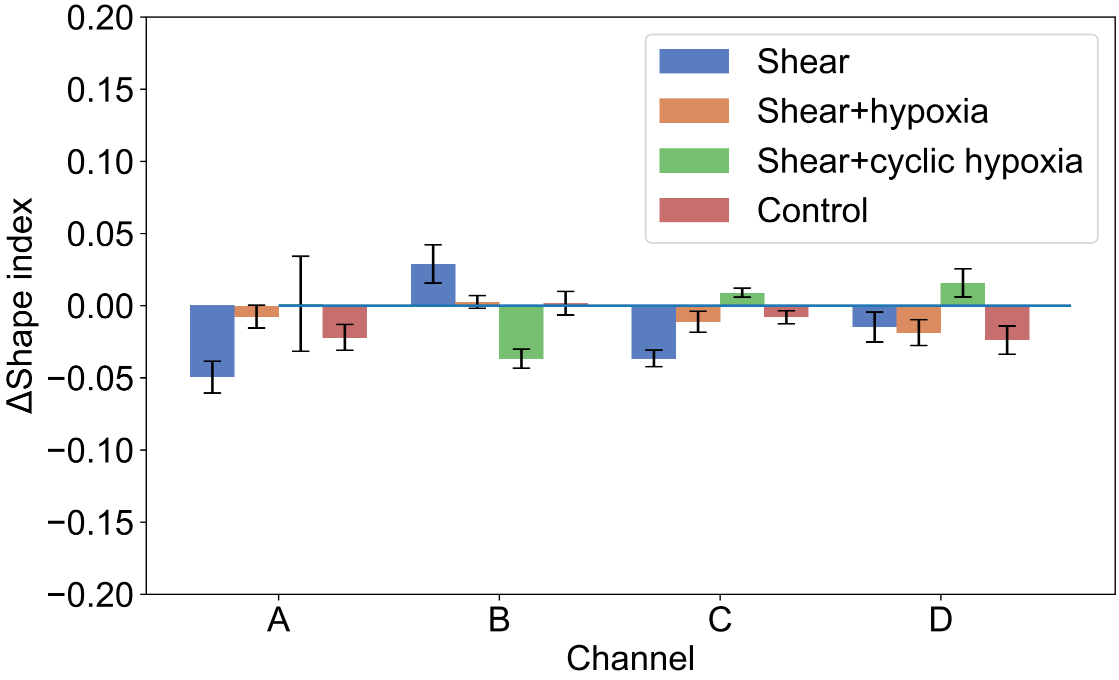

Figure 4.15 The morphology changed after 6 hours of different groups. The error bars represent the 95% confidence intervals.

doi:10.6342/NTU202402333

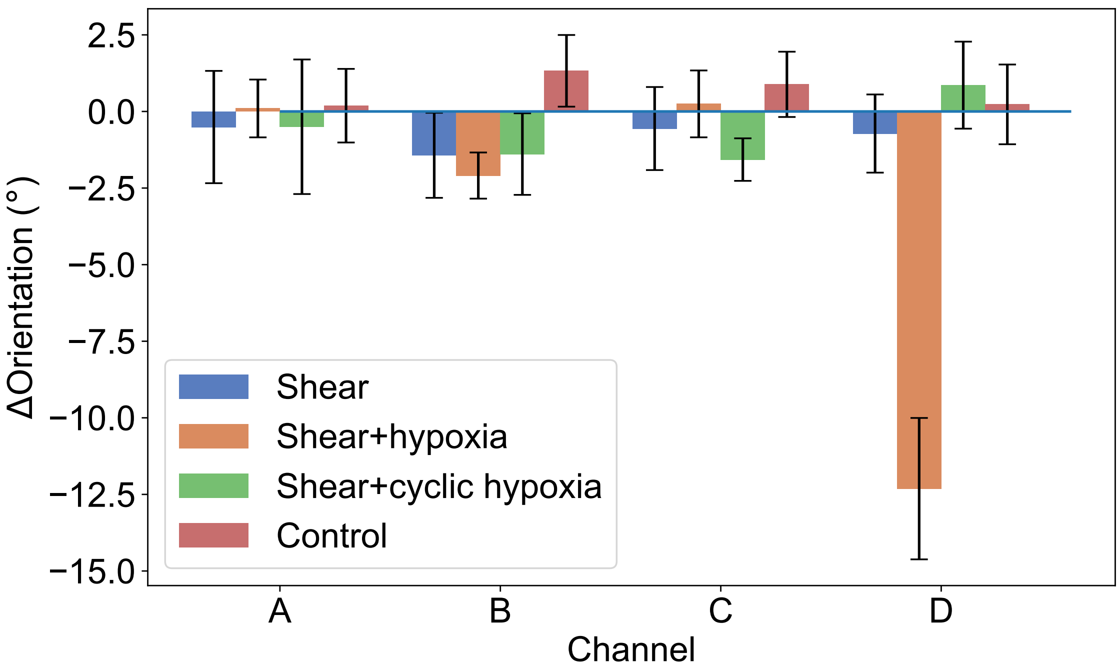

Figure 4.16 The orientation changed after 6 hours of different groups. The error bars represent the 95% confidence intervals.

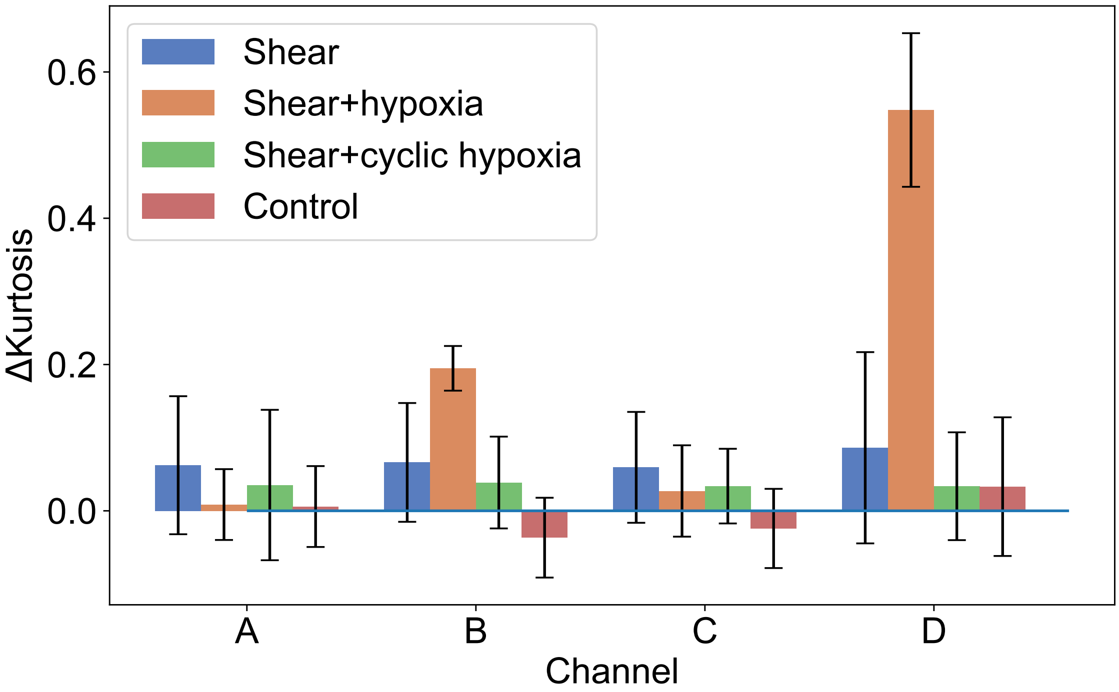

Figure 4.17 The kurtosis changed after 6 hours of different groups. The error bars represent the 95% confidence intervals.

doi:10.6342/NTU202402333

## 4.3 ROS production

### 4.3.1 ROS staining testing

To probe the ROS generation in HUVECs, we use DCFDA as described in Section 3.7. We found that ROS staining was very unstable in our chip. That is we usually see unevenness in the control group (Figure 4.19). The protocol of the staining process is shown in Figure 4.18. We inject buffer and dye using a syringe pump to control the flow rate of fluid exchange because HUVECs are extremely sensitive to shear stress even with a very short period [35] and this will change the ROS production. However, even with this protocol, we always observed higher fluorescence intensities at where we injected DCFDA (left side). We first think this may be contributed by the hydrostatic pressure generated due to the fluid injection, however, we still see this phenomenon.

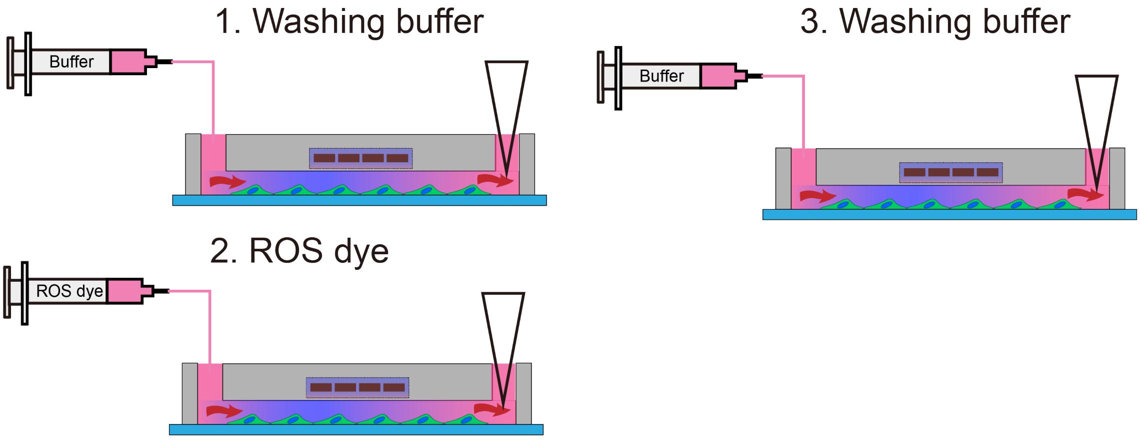

Figure 4.18 Initial staining protocol by syringe pump. The flow rate and volume used in each step is 3 $\mu$L/min and 20 $\mu$L respectively.

This suggests that the high fluorescence intensities may not correspond to the response of cells against hydrostatic pressure. We proposed another possibility is that the dye is taken by the cells upstream and thus the cells downstream share a lower concentration of the dye. Hence, we modified the protocol to inject DCFDA from both

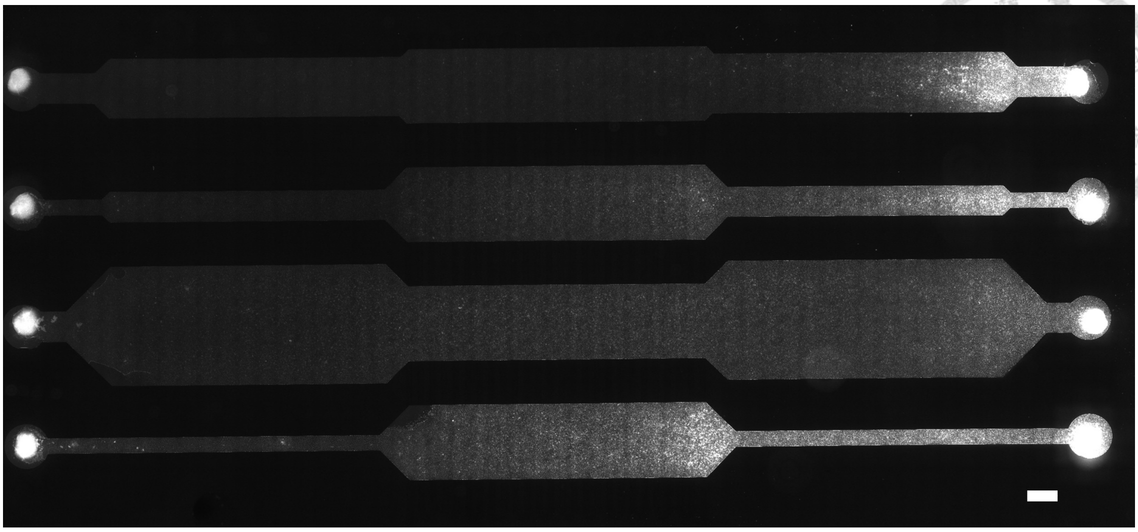

Figure 4.19 ROS intensities after using the first protocol in the control group. The scale bar is 1 mm.

sides of the channel (Figure 4.20).

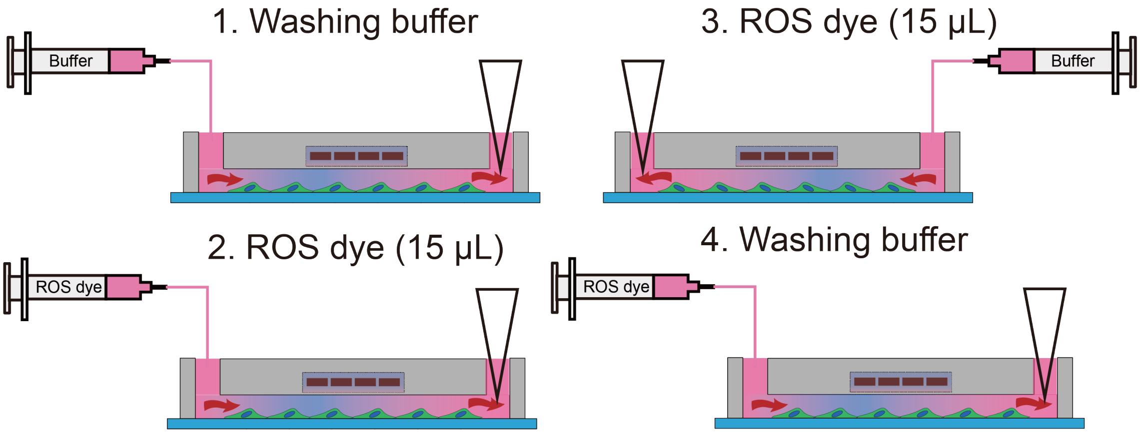

Figure 4.20 Modified staining protocol. Injecting DCFDA from both sides of the channel. The flow rate and volume used in step 1 and step 4 are 3 $\mu$L/min and 30 $\mu$L respectively. The flow rate in step 2 and step 3 is the same as step 1 and step 4.

The modified results are shown in Figure 4.21. Then evenness seems solved within the channel, but the intensities seem inversely proportional to the channel width. We then calculate the mean intensity in each channel and use the reciprocal ratio of it to calculate each volume we should inject into the channel.

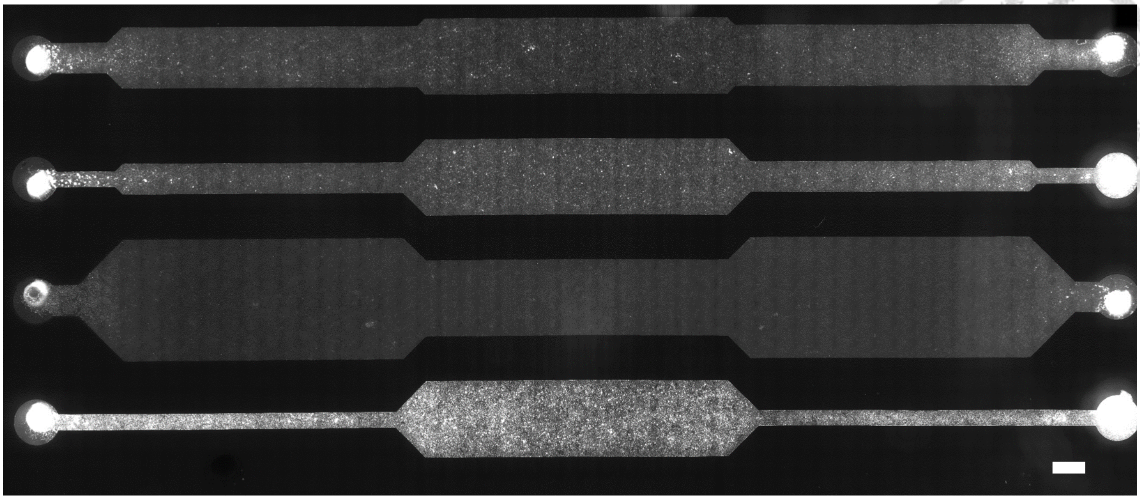

Figure 4.21 Using modified ROS staining protocol. The evenness between different ports is moderated. The scale bar is 1 mm.

The volumes used from the thinnest channel to the widest channel are 15, 30, 45, and 60 $\mu$L respectively. The result is shown in Figure 4.22. The inter-channel intensities are much more balanced.

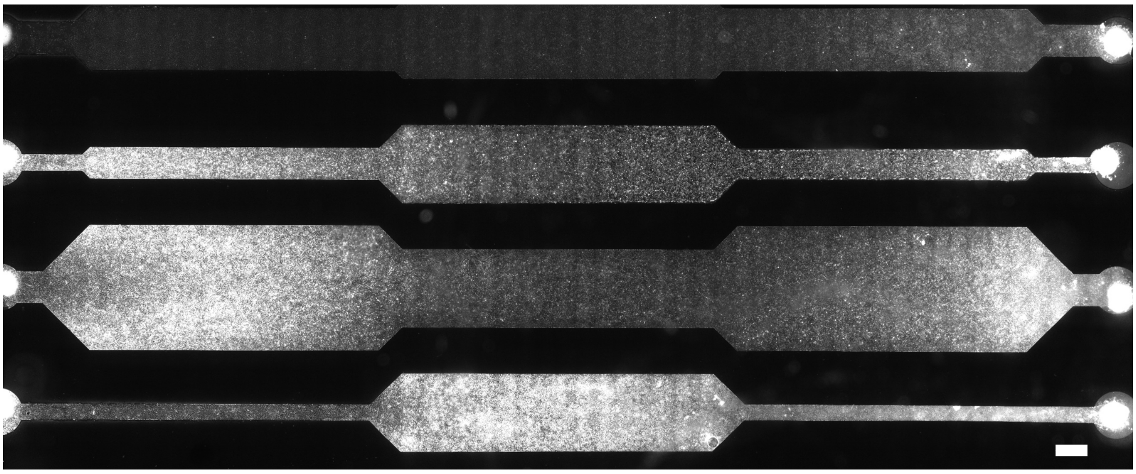

Figure 4.22 The final version of ROS staining protocol. The intensities difference between channels are compensated by using different volumes. The scale bar is 1 mm.

Although we should adopt the final version of the ROS staining protocol, we failed to solve the problem that there are often bubbles in the syringes due to using small volume DCFDA in our experiments. The bubbles will cause cell death as soon as they entered the channel, therefore we ended up using the protocol that used gravity to exchange fluid.

### 4.3.2 ROS production after continuous hypoxia and shear stress

After setting up the system as depicted in Section 3.5. We choose the stimulation time to be 1 hour. The duration time is determined by previous research revealed that ROS induced by shear stress appears in 15 minutes, while ROS induced by hypoxia appears in 60 minutes [9][34]. This plot shows the upstream of the channel, where the hypoxic conditions are not applied here. We observed a high expression of ROS in channel D, which indicates the shear stress induces ROS production. When the oxygen gradient is applied in the downstream channel, ROS intensity suppression is observed.

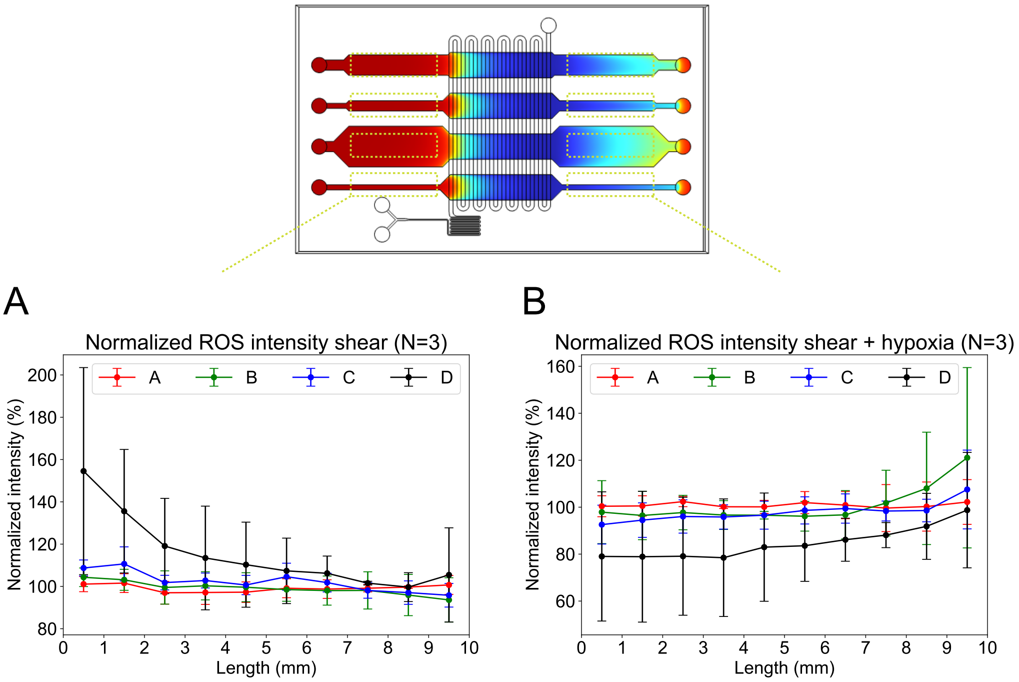

Figure 4.23 Normalized ROS intensity of (A) shear-only group (B) shear + hypoxia

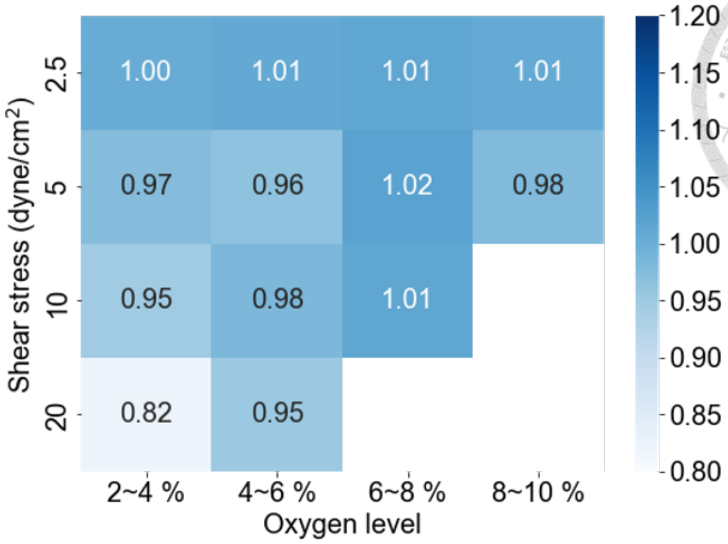

Figure 4.24 The normalized ROS vs oxygen level. Each section in channels corresponds to a different oxygen level. The results are calibrated according to the FLIM measurement (Figure 4.4).

## 4.4 NO production

### 4.4.1 NO staining testing

We use DAF-FM DA to measure the NO production inside HUVECs. We first test the dye with different concentrations in Petri dish. The protocol is as follows:

1. Remove medium in each Petri dish.
2. Adding 200 µL of 10, 5, 2, and 1 µM DAF-FM DA dissolved in medium respectively.
3. Wait for 1 hour.
4. Wash with 1ml medium twice and wait for 30 minutes to allow complete de-esterification of the intracellular diacetates.

The recommended concentration from the manufacturer is between 1 and 10 $\mu$M, so we test within this range. The cell contours are clearly seen when the concentration is more than 5 $\mu$M (Figure 4.25), so we chose 5 $\mu$M for our experiment. We have also tried 30$\mu$M due to the very low fluorescence intensity of DAF FM-DA, however, the cells are dead after treatment. We also observed that cells at the place where the dye is first added are much brighter than other cells (Figure 4.26). This suggests that the dye itself will stimulate cells or the dye is quickly absorbed by cells, which prevents the dye from distributing evenly through the dish. As the fluorescence intensity of DAF FM-DA is too low, we tried to suppress background noises by exchanging the solution with PBS. However, the background noises still exist.

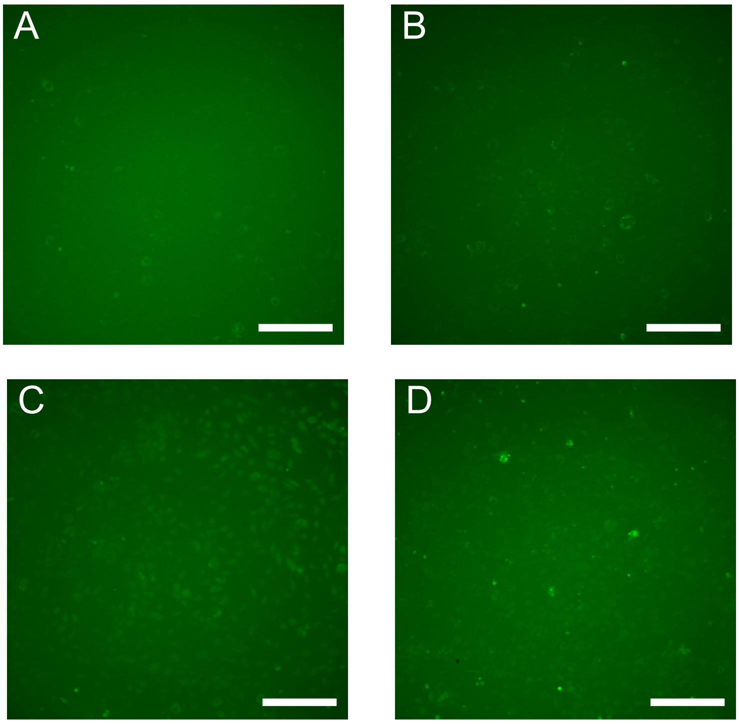

Figure 4.25 The NO dye testing in Petri dishes. (A) 1 $\mu$M (B) 2 $\mu$M (C) 5 $\mu$M (A) 10 $\mu$M. The scale bar is 100 $\mu$m.

doi:10.6342/NTU202402333

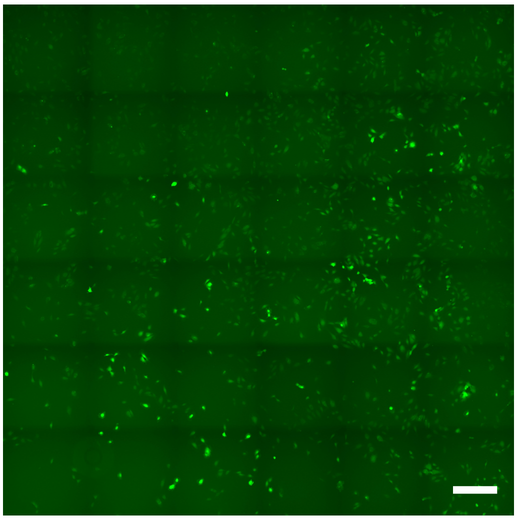

Figure 4.26 Unevenness of NO staining in Petri dish. The concentration here is 5 $\mu$M. The scale bar is 200 $\mu$m.

### 4.4.2 NO production after continuous hypoxia and shear stress

For NO production experiments, we set the stimulation time to 6 hours because the downregulation of NO is related to the transcriptional pathway, which needs a few hours to see the effect. In addition, DAF-FM DA is stable enough for taking multiple times of images, so we tried to get the time-lapse accumulated NO in HUVECs. The staining protocol is similar to the previous section:

1. Removing medium in each Petri dish
2. Adding 90, 60, 45, and 30 μL of 5 μM DAF-FM DA into each channel
3. Wait for 1 hour
4. Wash with 100 $\mu$ L medium twice and wait for 30 minutes.

We didn't see any differences after 6 hours no matter under what kind of stimulation. The NO production is normalized to the initial condition. However, in one of the experiments (not counted in previous plots), we observed the NO increment in the middle of channel D only (Figure 4.29A). We take $\frac{1}{3}$ width of the center channel as the high shear region to calculate to intensity changes. Although we might see the shear can up-regulate

doi:10.6342/NTU202402333

the NO production, but we still didn’t see any effect of hypoxia (Figure 4.28A). By the time-lapse image, we can know that NO is accumulated through time.

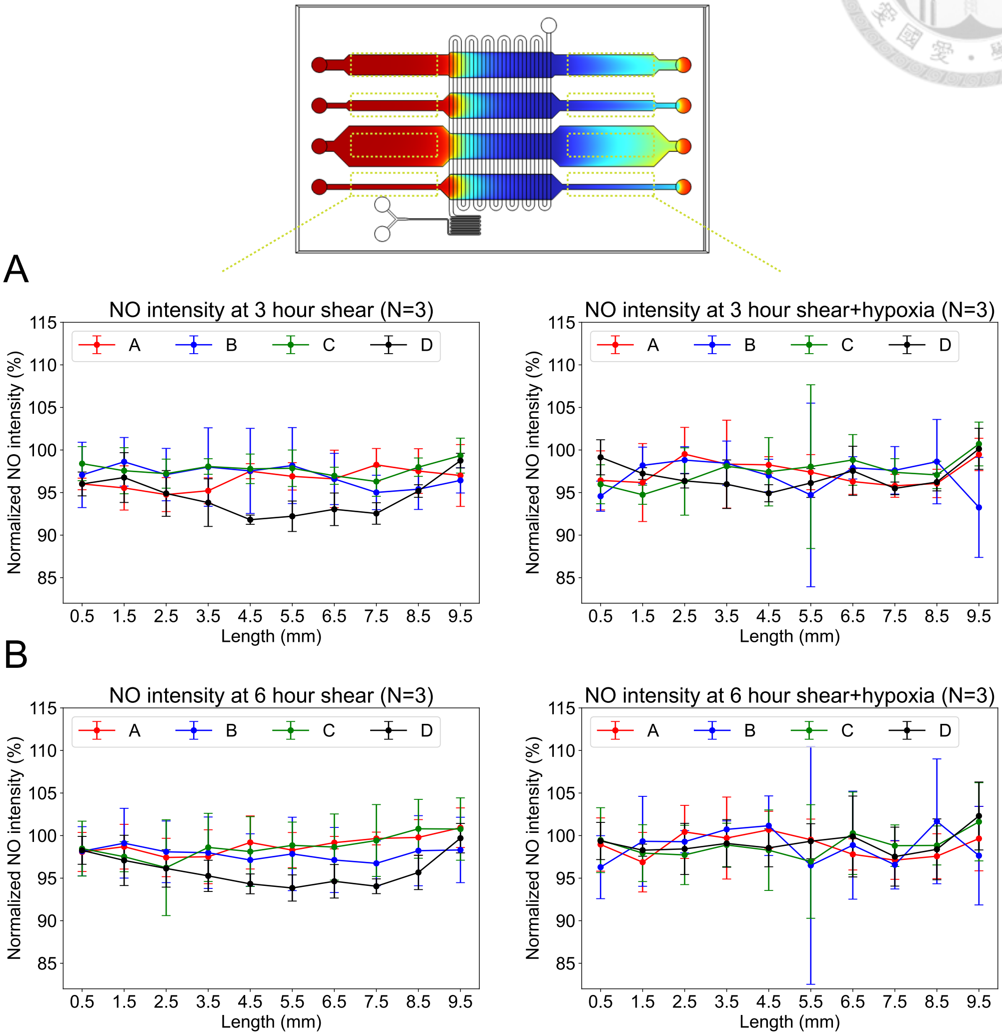

Figure 4.27 NO production under shear for (A) 3hours (B) 6 hours.

doi:10.6342/NTU202402333

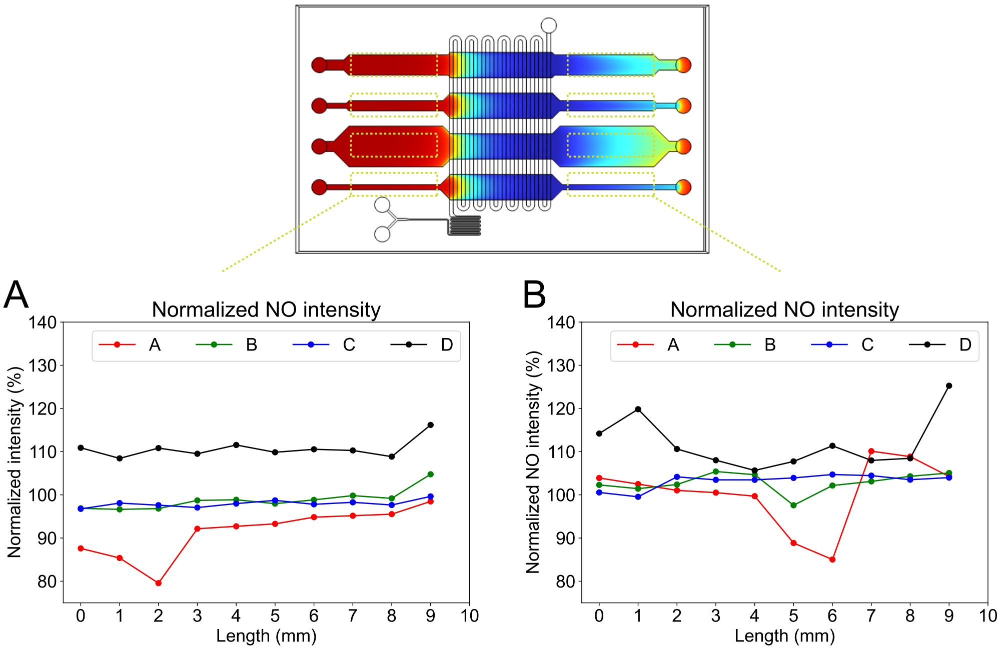

Figure 4.28 NO production under (A) shear and hypoxia and (B) shear for 6 hours in this certain experiment.

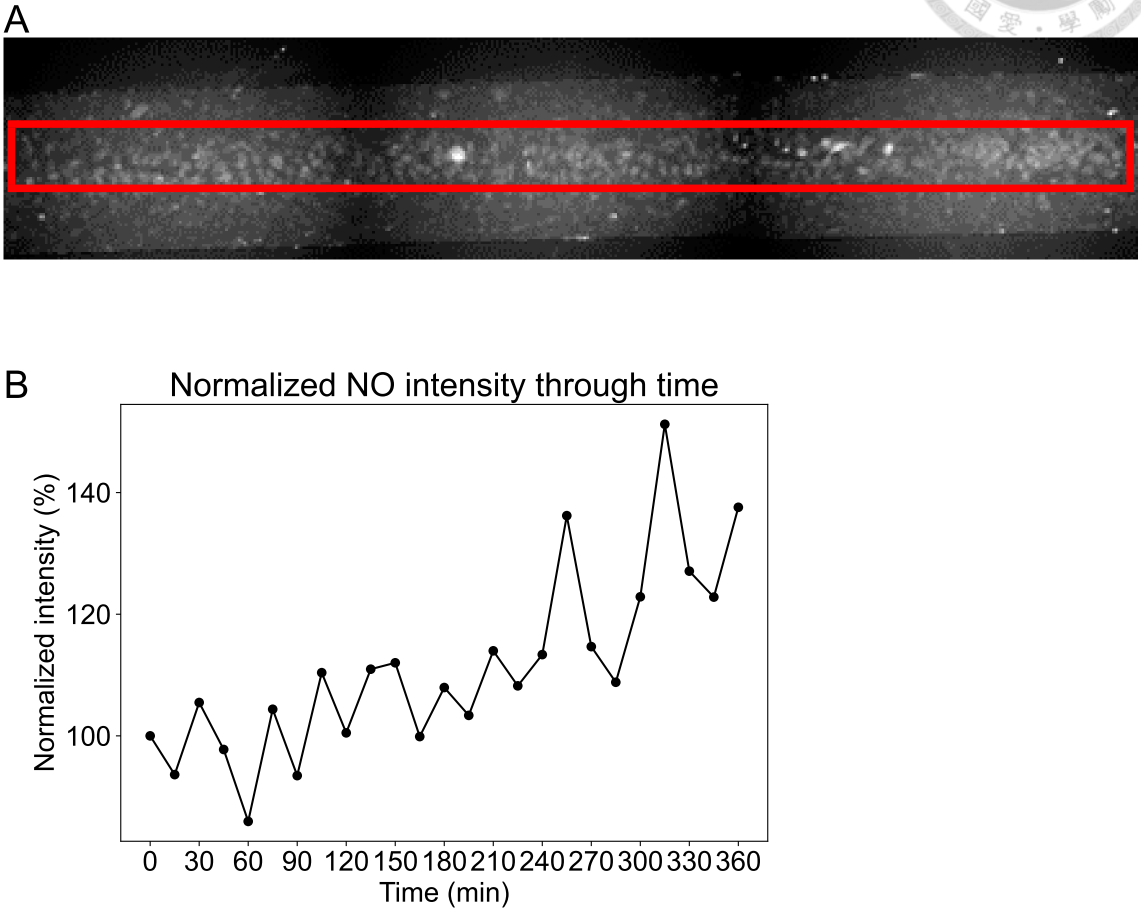

Figure 4.29 (A) Fluorescence image of HUVECs in channel D under stress stimulation for 6 hours in this certain experiment. NO production increase was observed at the center of the channel. This time-lapse measure of the red rectangular area is plotted in (B). (B) Time-lapse measurement of NO production. NO production increased suppose to the shear stress applied by flow.

## 4.5 Discussion

### 4.5.1 Chip design revisit

While designing and testing our chip, we found that the pressure generated in the hypoxia channel is very large due to its slender channel (Figure 4.30). This leads to the compression of the cell culture channel and results in extremely high local shear stress emerging beneath the upstream of the hypoxia channel. This high shear stress eventually kills the cells as shown in Figure 4.31. We identified the threshold value of the pressure differences around 4000 Pa. Therefore, we doubled the width of the hypoxia channel and halved its total length. We can expect that the pressure will then drop to about one-fourth of the previous design, and thus keep the pressure differences below threshold value.

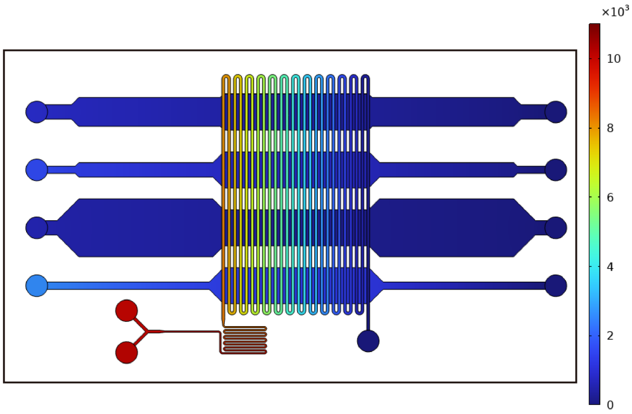

Figure 4.30 The pressure generated when the flow rate of the hypoxia channel and cell culture channel is 1 $\mu$L/min and 30 $\mu$L/min, respectively.

Besides, when performing staining in our experiment, we found that long channels are not suitable for staining. The solution inside the channel is hard to be fully exchanged, furthermore, the fluorescence dye will also hard to inject into the channel because of the high flow resistance. A large area of the channel also requires more cells for seeding. The reason that we designed our chip for such a long length is because we need to ensure medium enter hypoxic condition. From the derivation in Section 2.1, we can reduce our channel height to shorten the distance, this also helps lower the flow rate for generating the same shear stress thus further reducing the channel length. That is if the channel height is halved, the channel length can be $\frac{1}{8}$. On the other hand, the flow resistance is proportional to $wh^{-3}L$, for $(h \gg w)$, therefore the flow resistance is unchanged.

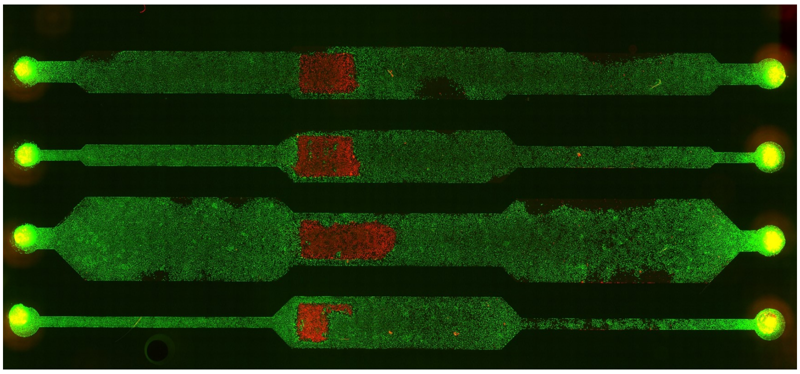

Figure 4.31 Live(green)/dead(red) staining of Calcein-AM/Eth-1 after 6 hours of shearing with 30 $\mu$L/min

### 4.5.2 Hypoxic condition generation

In our experiments, we always suffer from the coupling of shear stress and oxygen gradient. However, the solution may be hidden in Equation 2.12. Recall the solution for oxygen gradient region, and here we define the decoupling coefficient $\lambda = \frac{D_{\text{medium}} L_{\text{gradient}}}{H^2_{\text{channel}} v}$. We can rewrite the equation 2.12 as:

$$c_{\text{medium}}(x) = 0.75\text{solubility}_{\text{medium}}\left(\frac{x}{L_{\text{gradient}}} + \frac{1}{\lambda}\left(e^{-\lambda \frac{x}{L_{\text{gradient}}}} - 1\right)\right) \tag{4.1}$$

It is obvious that when $\lambda \to \infty$, the oxygen gradient is independent of velocity. Therefore, reducing channel height may be a good strategy to decouple shear stress and oxygen gradient. In our original design, $\lambda$ =0.0475, 0.095, 0.19, 0.38 for channels A, B, C, and D, respectively. Which is still too high if we say a threshold of 10%. If we halved the channel length, and maintain the shear stress condition, then the flow rate can be reduced to $\frac{1}{4}$. The plot for this condition of each channel will be as Figure 4.32. We can see that the gradient in each channel is almost the same. This will help us better control shear stress and oxygen gradient separately.

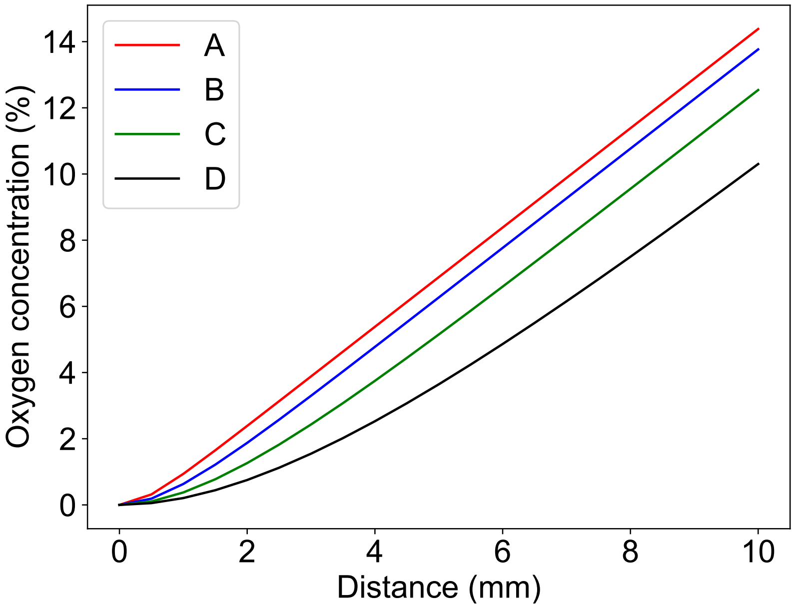

Figure 4.32 The oxygen profile estimated by Equation 2.12 when the channel height is halved.

### 4.5.3 Morphology

We used a machine learning based method to automatically calculate almost all the cells inside the channel. However, the cells don’t show any clear trends except we see cell alignment towards flow in the thinnest channel in hypoxic conditions. This result agrees with the previous study [68]. Interestingly, this alignment is not observed in the cyclic hypoxia condition. This might contribute that HIF-2$\alpha$, a transcription factor related to blood vessel maturation is not activated.

doi:10.6342/NTU202402333

### 4.5.4 ROS production

The ROS production under hypoxic conditions shows a clear trend of suppression. This is different from previous research. We have no idea why the differences exist, but it is still reasonable that the ROS production needs oxygen. If the oxygen is depleted, ROS production should also be lowered.

### 4.5.5 NO production

We didn't observe any clear changes in NO production. This should due to the NO dye itself's low sensitivity. We have no tools to test the dynamic range of the NO dye currently, so maybe the NO production of HUVECs is just out of the dynamic range. The NO intensity increment observed in the thinnest channel can not be replicated in other experiments. We doubt that the only time that shows gradually increasing NO intensity is because the channel may occur deformation. This generated unexpected high shear stress at the middle of the channel and thus induced the NO intensity.

doi:10.6342/NTU202402333

# Chapter 5 Conclusions

We have successfully developed a microfluidic system capable of generating both shear stress and hypoxic conditions simultaneously within a single chip, effectively mimicking the in vivo environment. This system has allowed us to achieve the following:

1. **Microenvironment control**

Utilizing microfluidic technology, we fabricated a two-layer PDMS device to create specific microenvironments. By mixing pyrogallol and NaOH and flowing this mixture through the top layer, we generated an oxygen scavenger that depleted oxygen in the bottom layer, establishing hypoxic conditions ranging from 2.8% to 12%. Introducing flow into the microfluidic device produced shear stress values of 2.5, 5, 10, and 20 dyne/cm$^2$ in channels A, B, C, and D, respectively. Simulations were employed to estimate the oxygen gradient, ensuring the conditions fell within the desired oxygen levels. Such precise control over the microenvironment is crucial for studying cellular responses under physiologically relevant conditions.

2. **Multiplexing capability of the device**

One of the notable features of our microfluidic chip is its multiplexing capability. This allows simultaneous investigation of four different combinations of oxygen gradients and shear stress levels, significantly accelerating the research process and reducing the labor intensity associated with traditional cell culture methods. This capability is particularly valuable for high-throughput screening and combinatorial studies, which are essential for understanding complex cellular behaviors.

3. **Cell behavior analysis**

In this study, we analyzed cell morphology, reactive oxygen species (ROS) production,

doi:10.6342/NTU202402333

and nitric oxide (NO) production under various conditions.

In cell morphology, we observed that cells aligned to the flow direction more rapidly under hypoxic conditions and higher shear stress, with a 12-degree alignment observed within 6 hours in channel D. This rapid alignment suggests an adaptive cellular response to the combined stimuli of hypoxia and shear stress .

Hypoxia appeared to suppress ROS production by approximately 20%, though the ROS dye stability was insufficient for definitive conclusions. These findings contradict previous research in endothelial cells, therefore further investigation is needed to confirm the reason.

No significant differences in NO production were observed across the different conditions. This lack of response may be attributed to the applied shear stress not being large enough or the exposure time being too short to elicit a detectable effect from hypoxia. Future studies could explore longer exposure times or higher shear stress levels to further investigate NO dynamics.

In summary, our microfluidic system offers a robust platform for studying endothelial cell responses under controlled shear stress and hypoxic conditions, providing valuable insights into cellular dynamics relevant to vascular biology and pathology.

doi:10.6342/NTU202402333

# Chapter 6 Future Work

This study successfully achieved a well-controlled microenvironment of shear stress and hypoxia generated within a microfluidic chip. However, to address the challenges encountered during our research and to further explore cellular behavior, several improvements and methodologies can be considered:

1. **Enhanced measurement tools for ROS and NO**

In our experiments, the measurement tools for ROS and NO posed significant challenges. For instance, while ROS dyes are sensitive, they are prone to interference and are unsuitable for long-term experiments. Conversely, NO dyes allow for monitoring over extended periods (more than 6 hours), but they suffer from much lower sensitivity. To overcome these limitations, the use of electrochemical-based sensors could be beneficial, despite their current limitation to extracellular ROS production measurements. These sensors offer higher stability and sensitivity, potentially providing more reliable data over prolonged periods.

2. **Fully automated system for staining processes**

Human umbilical vein endothelial cells (HUVECs) are highly sensitive to shear stress. In microfluidic systems, any perturbation can significantly affect the results. Therefore, developing an automated fluid exchange system that maintains consistent shear stress conditions during medium changes or staining processes is crucial. Such automation would reduce labor intensity and enhance experimental stability and reproducibility.

3. **Improved chip design**

As discussed in Section 4.5.1, shortening the channel height may address some of the issues encountered. However, this modification increases flow resistance and undesired

doi:10.6342/NTU202402333

shear stress. Further testing and optimization are necessary to identify a chip design that balances these factors effectively. Innovations in microfluidic chip design, such as incorporating adaptive materials or advanced fabrication techniques, could offer solutions to these challenges.

### 4. Co-culturing with other cells

Co-culturing endothelial cells with tumor cells has been a significant area of research for studying tumor vascularization, particularly under cyclic hypoxia, a key condition in the tumor microenvironment. Additionally, co-culturing with leukocytes is essential for investigating interactions during inflammatory reactions or immune responses. These studies could provide deeper insights into the complex cellular dynamics and interactions within different physiological and pathological contexts

By implementing these improvements, we believe a more precise microenvironment can be created, allowing for the capture of more accurate cellular behavior. These advancements will contribute to a deeper understanding of cardiovascular diseases and potentially lead to more effective therapeutic strategies.

doi:10.6342/NTU202402333

# References

[1] N. Amara, D. Goven, F. Prost, R. Muloway, B. Crestani, and J. Boczkowski. Nox4/nadph oxidase expression is increased in pulmonary fibroblasts from patients with idiopathic pulmonary fibrosis and mediates tgf$\beta$1-induced fibroblast differentiation into myofibroblasts. Thorax, 65(8):733–738, 2010.

[2] N. Baeyens, C. Bandyopadhyay, B. G. Coon, S. Yun, M. A. Schwartz, et al. Endothelial fluid shear stress sensing in vascular health and disease. The Journal of clinical investigation, 126(3):821–828, 2016.

[3] R. Bartoszewski, A. Moszyńska, M. Serocki, A. Cabaj, A. Polten, R. Ochocka, L. Dell'Italia, S. Bartoszewska, J. Króliczewski, M. Dąbrowski, et al. Primary endothelial cell–specific regulation of hypoxia-inducible factor (hif)-1 and hif-2 and their target gene expression profiles during hypoxia. The FASEB Journal, 33(7):7929–7941, 2019.

[4] C. Bayer and P. Vaupel. Acute versus chronic hypoxia in tumors. Strahlentherapie und Onkologie, 188(7):616–627, 2012.

[5] L. Botto, E. Beretta, R. Daffara, G. Miserocchi, and P. Palestini. Biochemical and morphological changes in endothelial cells in response to hypoxic interstitial edema. Respiratory research, 7(1):1–14, 2006.

[6] C. Bouquerel, W. César, L. Barthod, S. Arrak, A. Battistella, G. Gropplero, F. Mechta-Grigoriou, G. Zalcman, M. C. Parrini, M. Verhulsel, et al. Precise and fast control of the dissolved oxygen level for tumor-on-chip. Lab on a Chip, 22(22):4443–4455, 2022.

[7] P. Buchwald. Fem-based oxygen consumption and cell viability models for avascular pancreatic islets. Theoretical Biology and Medical Modelling, 6:1–13, 2009.

[8] A. E. Carpenter, T. R. Jones, M. R. Lamprecht, C. Clarke, I. H. Kang, O. Friman, D. A. Guertin, J. H. Chang, R. A. Lindquist, J. Moffat, et al. Cellprofiler: image analysis software for identifying and quantifying cell phenotypes. Genome biology, 7:1–11, 2006.

[9] N. Chandel, E. Maltepe, E. Goldwasser, C. Mathieu, M. Simon, and P. Schumacker. Mitochondrial reactive oxygen species trigger hypoxia-induced transcription. Proceedings of the National Academy of Sciences, 95(20):11715–11720, 1998.

[10] C.-W. Chang, Y.-J. Cheng, M. Tu, Y.-H. Chen, C.-C. Peng, W.-H. Liao, and Y.-C. Tung. A polydimethylsiloxane–polycarbonate hybrid microfluidic device capable of generating perpendicular chemical and oxygen gradients for cell culture studies. Lab on a Chip, 14(19):3762–3772, 2014.

[11] L.-J. Chen, S. Ito, H. Kai, K. Nagamine, N. Nagai, M. Nishizawa, T. Abe, and H. Kaji. Microfluidic co-cultures of retinal pigment epithelial cells and vascular endothelial cells to investigate choroidal angiogenesis. Scientific reports, 7(1):3538, 2017.

[12] W.-L. Chen, C.-C. Wang, Y.-J. Lin, C.-P. Wu, and C.-H. Hsieh. Cycling hypoxia induces chemoresistance through the activation of reactive oxygen species-mediated b-cell lymphoma extra-long pathway in glioblastoma multiforme. Journal of translational medicine, 13(1):1–13, 2015.

[13] S. Chien. Effects of disturbed flow on endothelial cells. Annals of biomedical engineering, 36:554–562, 2008.

[14] L. Chin, J. Yu, Y. Fu, T. Yu, A. Liu, and K. Luo. Production of reactive oxygen species in endothelial cells under different pulsatile shear stresses and glucose concentrations. Lab on a Chip, 11(11):1856–1863, 2011.

[15] D. A. Chistiakov, A. N. Orekhov, and Y. V. Bobryshev. Effects of shear stress on endothelial cells: go with the flow. Acta physiologica, 219(2):382–408, 2017.

[16] C. C. Chua, R. C. Hamdy, and B. H. Chua. Upregulation of vascular endothelial growth factor by h2o2 in rat heart endothelial cells. Free Radical Biology and Medicine, 25(8):891–897, 1998.

[17] S. M. Dauphinee and A. Karsan. Lipopolysaccharide signaling in endothelial cells. Laboratory investigation, 86(1):9–22, 2006.

[18] C. Dewey Jr, S. Bussolari, M. Gimbrone Jr, and P. F. Davies. The dynamic response of vascular endothelial cells to fluid shear stress. 1981.

[19] J. M. Dolan, H. Meng, S. Singh, R. Paluch, and J. Kolega. High fluid shear stress and spatial shear stress gradients affect endothelial proliferation, survival, and alignment. Annals of biomedical engineering, 39:1620–1631, 2011.

[20] A. Fick. Ueber diffusion. Annalen der Physik, 170(1):59–86, 1855.

[21] I. B. Fridman, G. S. Ugolini, V. VanDelinder, S. Cohen, and T. Konry. High throughput microfluidic system with multiple oxygen levels for the study of hypoxia in tumor spheroids. Biofabrication, 13(3):035037, 2021.

[22] K. Funamoto, D. Yoshino, K. Matsubara, I. K. Zervantonakis, K. Funamoto, M. Nakayama, J. Masamune, Y. Kimura, and R. D. Kamm. Endothelial monolayer permeability under controlled oxygen tension. Integrative Biology, 9(6):529–538, 2017.

[23] K. K. Gaikwad, S. Singh, and Y. S. Lee. A pyrogallol-coated modified ldpe film as an oxygen scavenging film for active packaging materials. Progress in Organic Coatings, 111:186–195, 2017.

[24] C. Galbraith, R. Skalak, and S. Chien. Shear stress induces spatial reorganization of the endothelial cell cytoskeleton. Cell motility and the cytoskeleton, 40(4):317–330, 1998.

[25] R. Gao, Z. Yuan, Z. Zhao, and X. Gao. Mechanism of pyrogallol autoxidation and determination of superoxide dismutase enzyme activity. Bioelectrochemistry and Bioenergetics, 45(1):41–45, 1998.

doi:10.6342/NTU202402333

[26] J. Grant, E. Lee, M. Almeida, S. Kim, N. LoGrande, G. Goyal, A. M. Sesay, D. T. Breault, R. Prantil-Baun, and D. E. Ingber. Establishment of physiologically relevant oxygen gradients in microfluidic organ chips. Lab on a Chip, 22(8):1584–1593, 2022.

[27] S. M. Grist, S. S. Nasseri, L. Laplatine, J. C. Schmok, D. Yao, J. Hua, L. Chrostowski, and K. C. Cheung. Long-term monitoring in a microfluidic system to study tumour spheroid response to chronic and cycling hypoxia. Scientific Reports, 9(1):17782, 2019.

[28] R. Gulaboski, V. Mirčeski, R. Kappl, M. Hoth, and M. Bozem. Quantification of hydrogen peroxide by electrochemical methods and electron spin resonance spectroscopy. Journal of The Electrochemical Society, 166(8):G82, 2019.

[29] K. Hattori, Y. Munehira, H. Kobayashi, T. Satoh, S. Sugiura, and T. Kanamori. Microfluidic perfusion culture chip providing different strengths of shear stress for analysis of vascular endothelial function. Journal of bioscience and bioengineering, 118(3):327–332, 2014.

[30] A. Hernandez-Mijares, M. Rocha, S. Rovira-Llopis, C. Bañuls, L. Bellod, C. De Pablo, A. Alvarez, I. Roldan-Torres, E. Sola-Izquierdo, and V. M. Victor. Human leukocyte/endothelial cell interactions and mitochondrial dysfunction in type 2 diabetic patients and their association with silent myocardial ischemia. Diabetes care, 36(6):1695–1702, 2013.

[31] J. D. Ho, H. J. Man, and P. A. Marsden. Nitric oxide signaling in hypoxia. Journal of molecular medicine, 90:217–231, 2012.

[32] T. K. Hsiai, J. Hwang, M. L. Barr, A. Correa, R. Hamilton, M. Alavi, M. Rouhanizadeh, E. Cadenas, and S. L. Hazen. Hemodynamics influences vascular peroxynitrite formation: Implication for low-density lipoprotein apo-b-100 nitration. Free Radical Biology and Medicine, 42(4):519–529, 2007.

[33] C.-H. Hsieh, W.-C. Shyu, C.-Y. Chiang, J.-W. Kuo, W.-C. Shen, and R.-S. Liu. Nadph oxidase subunit 4-mediated reactive oxygen species contribute to cycling hypoxia-promoted tumor progression in glioblastoma multiforme. PloS one, 6(9):e23945, 2011.

[34] H.-J. Hsieh, C.-C. Cheng, S.-T. Wu, J.-J. Chiu, B.-S. Wung, and D. L. Wang. Increase of reactive oxygen species (ros) in endothelial cells by shear flow and involvement of ros in shear-induced c-fos expression. Journal of cellular physiology, 175(2):156–162, 1998.

[35] H.-J. Hsieh, C.-A. Liu, B. Huang, A. H. Tseng, and D. L. Wang. Shear-induced endothelial mechanotransduction: the interplay between reactive oxygen species (ros) and nitric oxide (no) and the pathophysiological implications. Journal of biomedical science, 21:1–15, 2014.

[36] M. A. Incalza, R. D'Oria, A. Natalicchio, S. Perrini, L. Laviola, and F. Giorgino. Oxidative stress and reactive oxygen species in endothelial dysfunction associated with cardiovascular and metabolic diseases. Vascular pharmacology, 100:1–19, 2018.

[37] M. H. Kim, S. D. Green, C.-C. Lin, and H. Konig. Engineering tools for regulating hypoxia in tumour models. Journal of Cellular and Molecular Medicine, 25(16):7581–7592, 2021.

[38] Y.-W. Kim and T. V. Byzova. Oxidative stress in angiogenesis and vascular disease. Blood, the Journal of the American Society of Hematology, 123(5):625–631, 2014.

[39] Y.-W. Kim, X. Z. West, and T. V. Byzova. Inflammation and oxidative stress in angiogenesis and vascular disease. Journal of molecular medicine, 91(3):323–328, 2013.

[40] R. Koens, Y. Tabata, J. C. Serrano, S. Aratake, D. Yoshino, R. D. Kamm, and K. Funamoto. Microfluidic platform for three-dimensional cell culture under spatiotemporal heterogeneity of oxygen tension. APL bioengineering, 4(1), 2020.

[41] P. Lee, N. S. Chandel, and M. C. Simon. Cellular adaptation to hypoxia through hypoxia inducible factors and beyond. Nature reviews Molecular cell biology, 21(5):268–283, 2020.

[42] M. Levesque and R. Nerem. The elongation and orientation of cultured endothelial cells in response to shear stress. 1985.

[43] Y. Li, L. Li, Z. Liu, M. Ding, G. Luo, and Q. Liang. A microfluidic chip of multiple-channel array with various oxygen tensions for drug screening. Microfluidics and Nanofluidics, 20:1–9, 2016.

[44] J. Liu, Y. Qiang, O. Alvarez, and E. Du. Electrical impedance characterization of erythrocyte response to cyclic hypoxia in sickle cell disease. ACS sensors, 4(7):1783–1790, 2019.

[45] M.-C. Liu, H.-C. Shih, J.-G. Wu, T.-W. Weng, C.-Y. Wu, J.-C. Lu, and Y.-C. Tung. Electrofluidic pressure sensor embedded microfluidic device: a study of endothelial cells under hydrostatic pressure and shear stress combinations. Lab on a Chip, 13(9):1743–1753, 2013.

[46] J. López-Barneo, R. Pardal, and P. Ortega-Sáenz. Cellular mechanism of oxygen sensing. Annual review of physiology, 63(1):259–287, 2001.

[47] E. Lubos, D. E. Handy, and J. Loscalzo. Role of oxidative stress and nitric oxide in atherothrombosis. Frontiers in bioscience: a journal and virtual library, 13:5323, 2008.

[48] P. Martinive, F. Defresne, C. Bouzin, J. Saliez, F. Lair, V. Grégoire, C. Michiels, C. Dessy, and O. Feron. Preconditioning of the tumor vasculature and tumor cells by intermittent hypoxia: implications for anticancer therapies. Cancer research, 66(24):11736–11744, 2006.

[49] P. Martinive, F. Defresne, E. Quaghebeur, G. Daneau, N. Crokart, V. Gregoire, B. Gallez, C. Dessy, and O. Feron. Impact of cyclic hypoxia on hif-1$\alpha$ regulation in endothelial cells–new insights for anti-tumor treatments. The FEBS journal, 276(2):509–518, 2009.

[50] J. S. McNally, M. E. Davis, D. P. Giddens, A. Saha, J. Hwang, S. Dikalov, H. Jo, and D. G. Harrison. Role of xanthine oxidoreductase and nad (p) h oxidase in endothelial superoxide production in response to oscillatory shear stress. American Journal of Physiology-Heart and Circulatory Physiology, 285(6):H2290–H2297, 2003.

[51] L. P. McQuillan, G. K. Leung, P. A. Marsden, S. K. Kostyk, and S. Kourembanas. Hypoxia inhibits expression of enos via transcriptional and posttranscriptional mechanisms. American Journal of Physiology-Heart and Circulatory Physiology, 267(5):H1921–H1927, 1994.

[52] T. Merkel, V. Bondar, K. Nagai, B. Freeman, and I. Pinnau. Gas sorption, diffusion, and permeation in poly (dimethylsiloxane). Journal of Polymer Science Part B: Polymer Physics, 38(3):415–434, 2000.

[53] C. Michiels, T. Arnould, and J. Remacle. Endothelial cell responses to hypoxia: initiation of a cascade of cellular interactions. Biochimica et Biophysica Acta (BBA)-Molecular Cell Research, 1497(1):1–10, 2000.

[54] C. Michiels, C. Tellier, and O. Feron. Cycling hypoxia: A key feature of the tumor microenvironment. Biochimica et Biophysica Acta (BBA)-Reviews on Cancer, 1866(1):76–86, 2016.

[55] B. Muz, P. de la Puente, F. Azab, and A. K. Azab. The role of hypoxia in cancer progression, angiogenesis, metastasis, and resistance to therapy. Hypoxia, 3:83, 2015.

[56] J. M. Oh, H. M. Begum, Y. L. Liu, Y. Ren, and K. Shen. Recapitulating tumor hypoxia in a cleanroom-free, liquid-pinning-based microfluidic tumor model. ACS biomaterials science & engineering, 8(7):3107–3121, 2022.

[57] V. Palacio-Castañeda, N. Velthuijs, S. Le Gac, and W. P. Verdurmen. Oxygen control: the often overlooked but essential piece to create better in vitro systems. Lab on a Chip, 22(6):1068–1092, 2022.

[58] T. G. Papaioannou, C. Stefanadis, et al. Vascular wall shear stress: basic principles and methods. Hellenic J Cardiol, 46(1):9–15, 2005.

[59] D. P. Pearlstein, M. H. Ali, P. T. Mungai, K. L. Hynes, B. L. Gewertz, and P. T. Schumacker. Role of mitochondrial oxidant generation in endothelial cell responses to hypoxia. Arteriosclerosis, thrombosis, and vascular biology, 22(4):566–573, 2002.

[60] J.-P. PIRET, D. Mottet, M. Raes, and C. Michiels. Cocl2, a chemical inducer of hypoxia-inducible factor-1, and hypoxia reduce apoptotic cell death in hepatoma cell line hepg2. Annals of the New York Academy of Sciences, 973(1):443–447, 2002.

[61] N. Ricard, S. Bailly, C. Guignabert, and M. Simons. The quiescent endothelium: signalling pathways regulating organ-specific endothelial normalcy. Nature Reviews Cardiology, 18(8):565–580, 2021.

[62] O. Ronneberger, P. Fischer, and T. Brox. U-net: Convolutional networks for biomedical image segmentation. In Medical Image Computing and

Computer-Assisted Intervention–MICCAI 2015: 18th International Conference, Munich, Germany, October 5-9, 2015, Proceedings, Part III 18, pages 234–241. Springer, 2015.

[63] H.-C. Shih, T.-A. Lee, H.-M. Wu, P.-L. Ko, W.-H. Liao, and Y.-C. Tung. Microfluidic collective cell migration assay for study of endothelial cell proliferation and migration under combinations of oxygen gradients, tensions, and drug treatments. Scientific reports, 9(1):8234, 2019.

[64] V. S. Shirure, S. F. Lam, B. Shergill, Y. E. Chu, N. R. Ng, and S. C. George. Quantitative design strategies for fine control of oxygen in microfluidic systems. Lab on a Chip, 20(16):3036–3050, 2020.

[65] H. Sies, V. V. Belousov, N. S. Chandel, M. J. Davies, D. P. Jones, G. E. Mann, M. P. Murphy, M. Yamamoto, and C. Winterbourn. Defining roles of specific reactive oxygen species (ros) in cell biology and physiology. Nature Reviews Molecular Cell Biology, 23(7):499–515, 2022.

[66] V. I. Sikavitsas, G. N. Bancroft, and A. G. Mikos. Formation of three-dimensional cell/polymer constructs for bone tissue engineering in a spinner flask and a rotating wall vessel bioreactor. Journal of Biomedical Materials Research: An Official Journal of The Society for Biomaterials, The Japanese Society for Biomaterials, and The Australian Society for Biomaterials and the Korean Society for Biomaterials, 62(1):136–148, 2002.

[67] G. P. Sorescu, H. Song, S. L. Tressel, J. Hwang, S. Dikalov, D. A. Smith, N. L. Boyd, M. O. Platt, B. Lassegue, K. K. Griendling, et al. Bone morphogenic protein 4 produced in endothelial cells by oscillatory shear stress induces monocyte adhesion by stimulating reactive oxygen species production from a nox1-based nadph oxidase. Circulation research, 95(8):773–779, 2004.

[68] N. Takahashi, D. Yoshino, R. Sugahara, S. Hirose, K. Sone, J.-P. Rieu, and K. Funamoto. Microfluidic platform for the reproduction of hypoxic vascular microenvironments. Scientific reports, 13(1):5428, 2023.

[69] S. R. Thomas, P. K. Witting, and G. R. Drummond. Redox control of endothelial function and dysfunction: molecular mechanisms and therapeutic opportunities. Antioxidants & redox signaling, 10(10):1713–1766, 2008.

[70] J. N. Topper, J. Cai, D. Falb, and M. Gimbrone Jr. Identification of vascular endothelial genes differentially responsive to fluid mechanical stimuli: cyclooxygenase-2, manganese superoxide dismutase, and endothelial cell nitric oxide synthase are selectively up-regulated by steady laminar shear stress. Proceedings of the National Academy of Sciences, 93(19):10417–10422, 1996.

[71] E. Tzima, M. Irani-Tehrani, W. B. Kiosses, E. Dejana, D. A. Schultz, B. Engelhardt, G. Cao, H. DeLisser, and M. A. Schwartz. A mechanosensory complex that mediates the endothelial cell response to fluid shear stress. Nature, 437(7057):426–431, 2005.

[72] M. Ushio-Fukai and R. W. Alexander. Reactive oxygen species as mediators of angiogenesis signaling. role of nad (p) h oxidase. Molecular and cellular biochemistry, 264(1):85–97, 2004.

[73] L. Wang, W. Liu, Y. Wang, J.-c. Wang, Q. Tu, R. Liu, and J. Wang. Construction of oxygen and chemical concentration gradients in a single microfluidic device for studying tumor cell–drug interactions in a dynamic hypoxia microenvironment. Lab on a Chip, 13(4):695–705, 2013.

[74] Y.-X. Wang, H.-B. Liu, P.-S. Li, W.-X. Yuan, B. Liu, S.-T. Liu, and K.-R. Qin. Ros and no dynamics in endothelial cells exposed to exercise-induced wall shear stress. Cellular and Molecular Bioengineering, 12:107–120, 2019.

[75] S. J. White, E. M. Hayes, S. Lehoux, J. Y. Jeremy, A. J. Horrevoets, and A. C. Newby. Characterization of the differential response of endothelial cells exposed to normal and elevated laminar shear stress. Journal of cellular physiology, 226(11):2841–2848, 2011.

[76] H.-M. Wu, T.-A. Lee, P.-L. Ko, W.-H. Liao, T.-H. Hsieh, and Y.-C. Tung. Widefield frequency domain fluorescence lifetime imaging microscopy (fd-flim) for accurate measurement of oxygen gradients within microfluidic devices. Analyst, 144(11):3494–3504, 2019.

[77] W. Xing, M. Yin, Q. Lv, Y. Hu, C. Liu, and J. Zhang. Oxygen solubility, diffusion coefficient, and solution viscosity. In Rotating electrode methods and oxygen reduction electrocatalysts, pages 1–31. Elsevier, 2014.

[78] W. Yang and E. R. Block. Effect of hypoxia and reoxygenation on the formation and release of reactive oxygen species by porcine pulmonary artery endothelial cells. Journal of cellular physiology, 164(2):414–423, 1995.

[79] T. Ziegler, K. Bouzourene, V. J. Harrison, H. R. Brunner, and D. Hayoz. Influence of oscillatory and unidirectional flow environments on the expression of endothelin and nitric oxide synthase in cultured endothelial cells. Arteriosclerosis, thrombosis, and vascular biology, 18(5):686–692, 1998.

[80] C. Zielke, C. W. Pan, A. J. Gutierrez Ramirez, C. Feit, C. Dobson, C. Davidson, B. Sandel, and P. Abbyad. Microfluidic platform for the isolation of cancer-cell subpopulations based on single-cell glycolysis. Analytical chemistry, 92(10):6949–6957, 2020.

[81] J. J. Zulueta, F.-S. Yu, I. A. Hertig, V. J. Thannickal, and P. M. Hassoun. Release of hydrogen peroxide in response to hypoxia-reoxygenation: role of an nad (p) h oxidase-like enzyme in endothelial cell plasma membrane. American journal of respiratory cell and molecular biology, 12(1):41–49, 1995.

Appendices

doi:10.6342/NTU202402333

# Appendix A — Cell Morphology

## A.1 Scatter plots

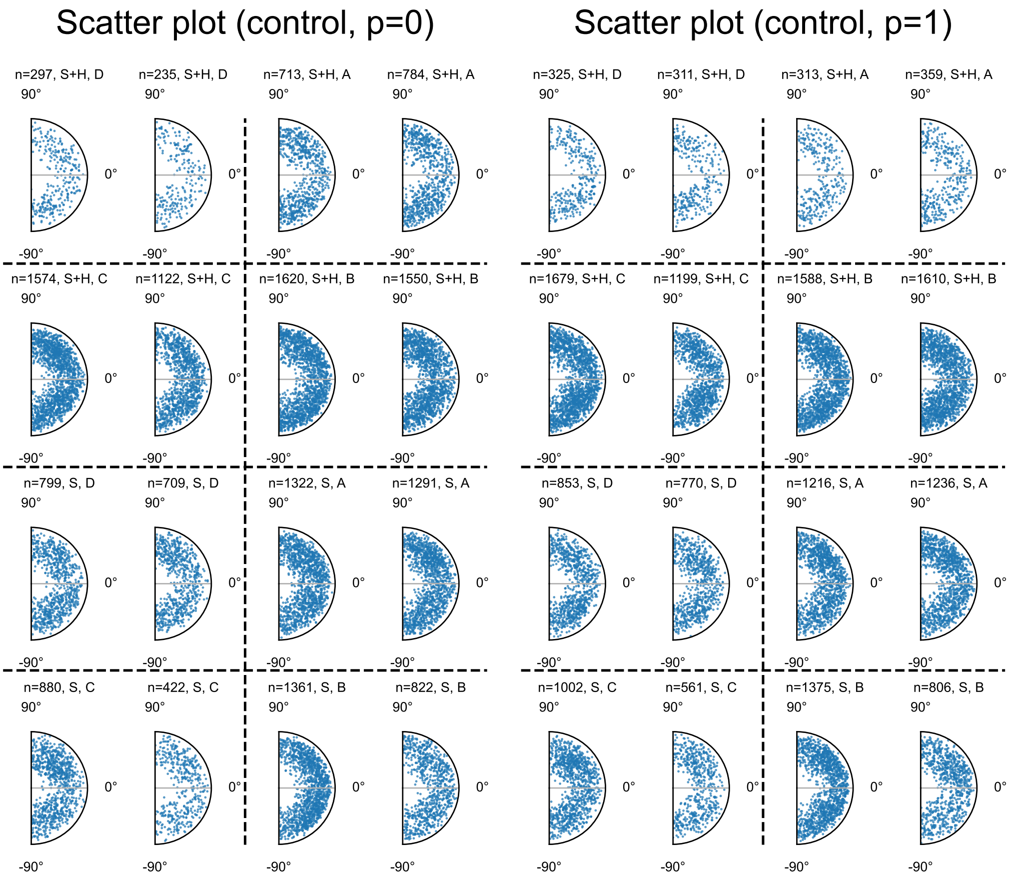

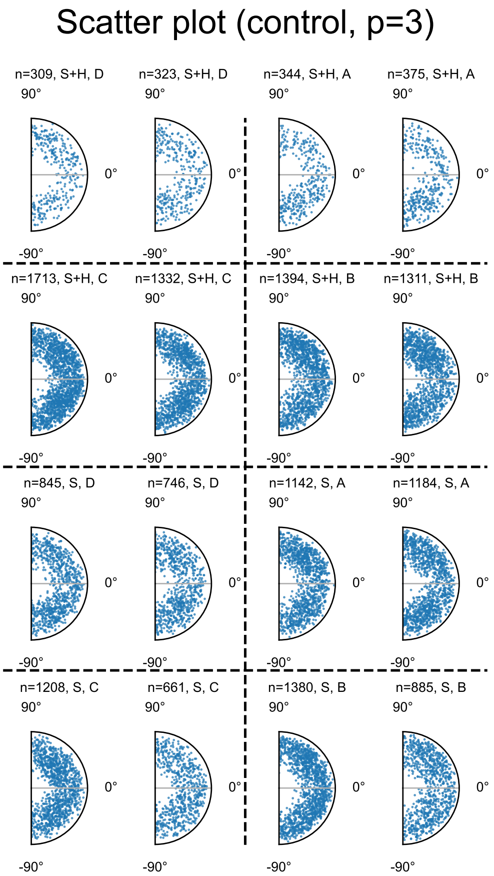
Scatter plot (control, p=3)
n=309, S+H, D
n=323, S+H, D
n=344, S+H, A
n=375, S+H, A
n=1713, S+H, C
n=1332, S+H, C
n=1394, S+H, B
n=1311, S+H, B
n=845, S, D
n=746, S, D
n=1142, S, A
n=1184, S, A
n=1208, S, C
n=661, S, C
n=1380, S, B
n=885, S, B
90°
0°
-90°

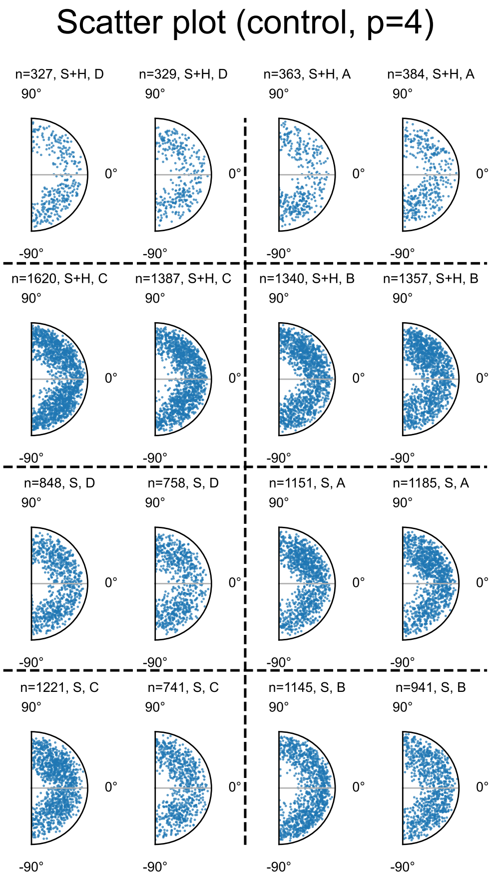
Scatter plot (control, p=4)
n=327, S+H, D
n=329, S+H, D
n=363, S+H, A
n=384, S+H, A
n=1620, S+H, C
n=1387, S+H, C
n=1340, S+H, B
n=1357, S+H, B
n=848, S, D
n=758, S, D
n=1151, S, A
n=1185, S, A
n=1221, S, C
n=741, S, C
n=1145, S, B
n=941, S, B
90°
0°
-90°

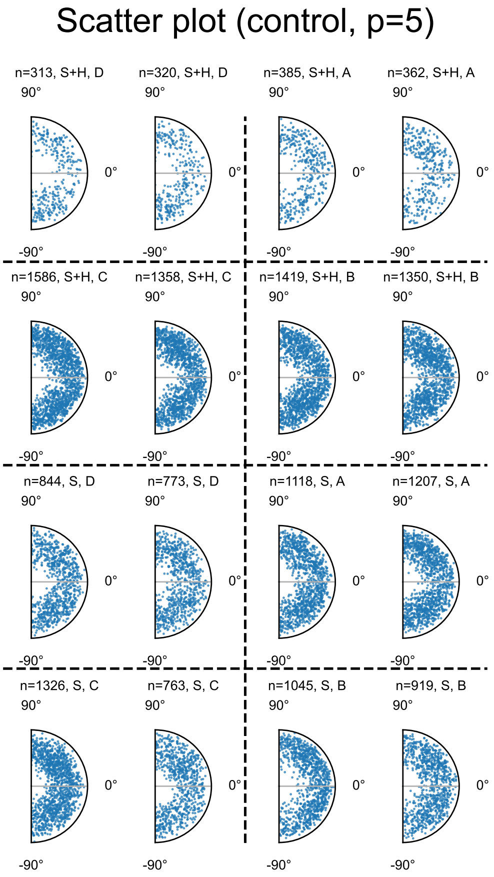
Scatter plot (control, p=5)
n=313, S+H, D
n=320, S+H, D
n=385, S+H, A
n=362, S+H, A
n=1586, S+H, C
n=1358, S+H, C
n=1419, S+H, B
n=1350, S+H, B
n=844, S, D
n=773, S, D
n=1118, S, A
n=1207, S, A
n=1326, S, C
n=763, S, C
n=1045, S, B
n=919, S, B
90°
0°
-90°

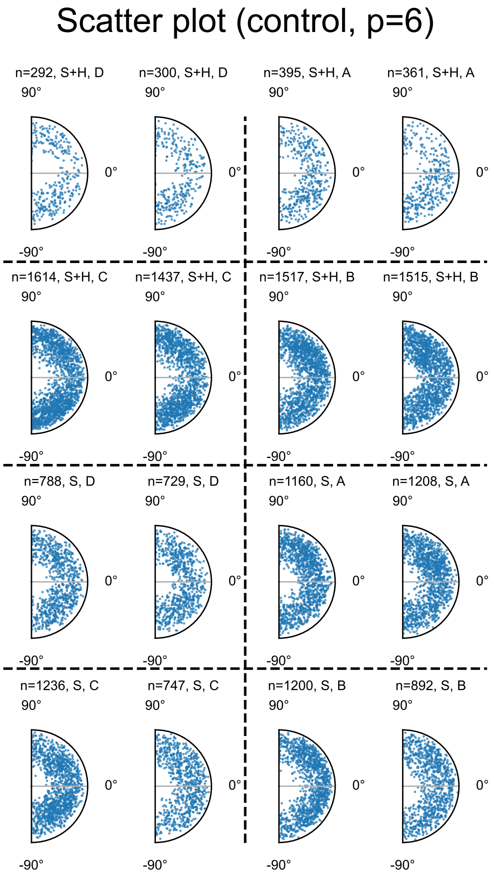
Scatter plot (control, p=6)
n=292, S+H, D
n=300, S+H, D
n=395, S+H, A
n=361, S+H, A
n=1614, S+H, C
n=1437, S+H, C
n=1517, S+H, B
n=1515, S+H, B
n=788, S, D
n=729, S, D
n=1160, S, A
n=1208, S, A
n=1236, S, C
n=747, S, C
n=1200, S, B
n=892, S, B
90°
0°
-90°

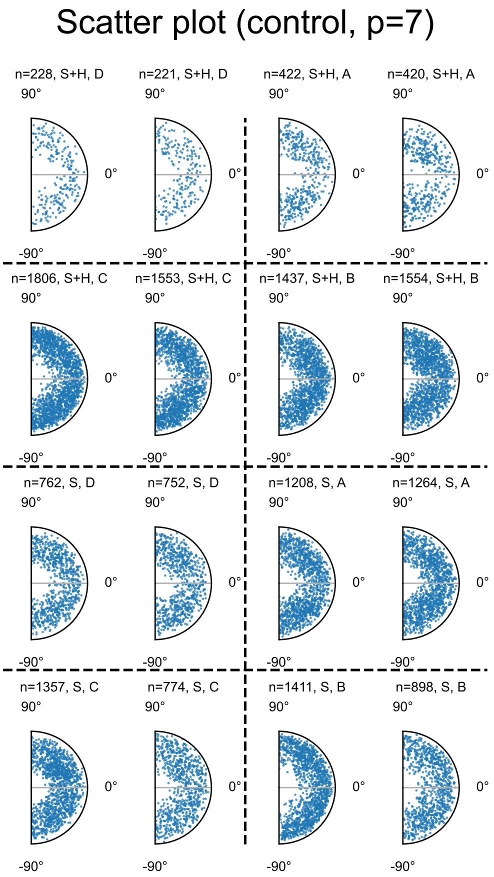
Scatter plot (control, p=7)

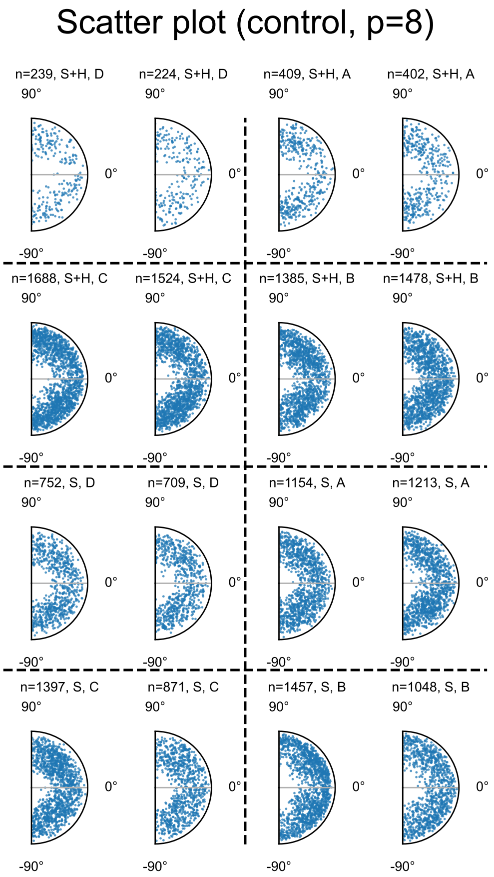
Scatter plot (control, p=8)

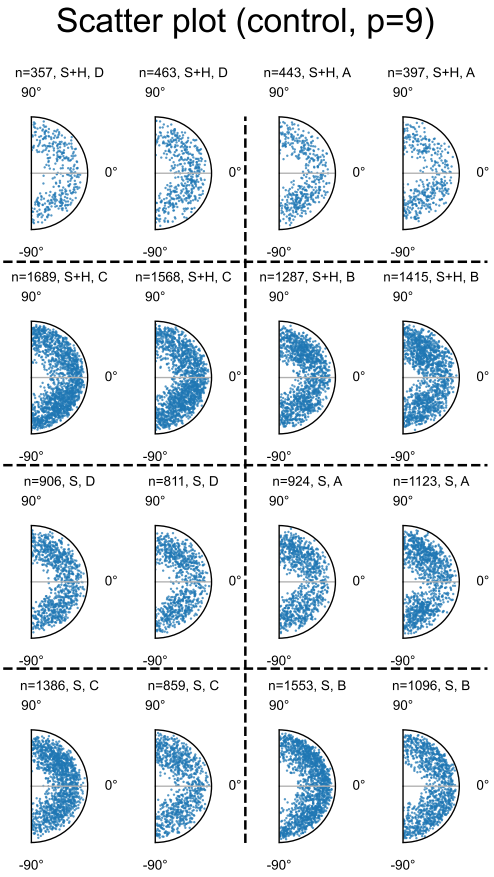
Scatter plot (control, p=9)

doi:10.6342/NTU202402333

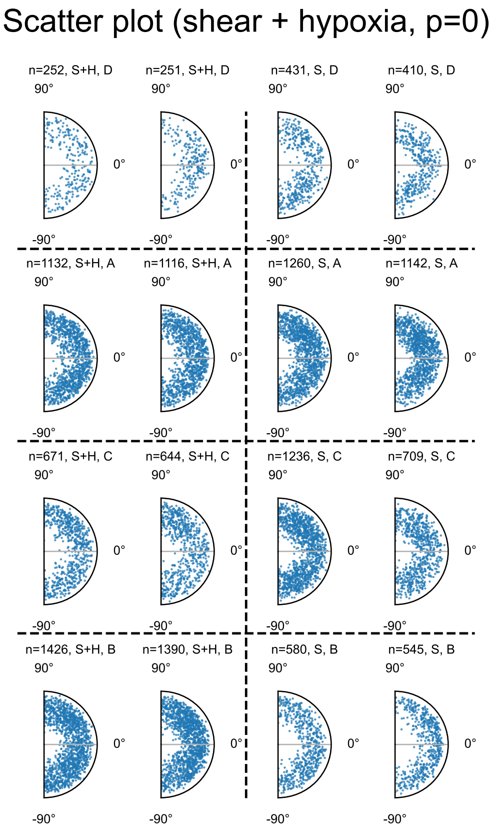
Scatter plot (shear + hypoxia, p=0)

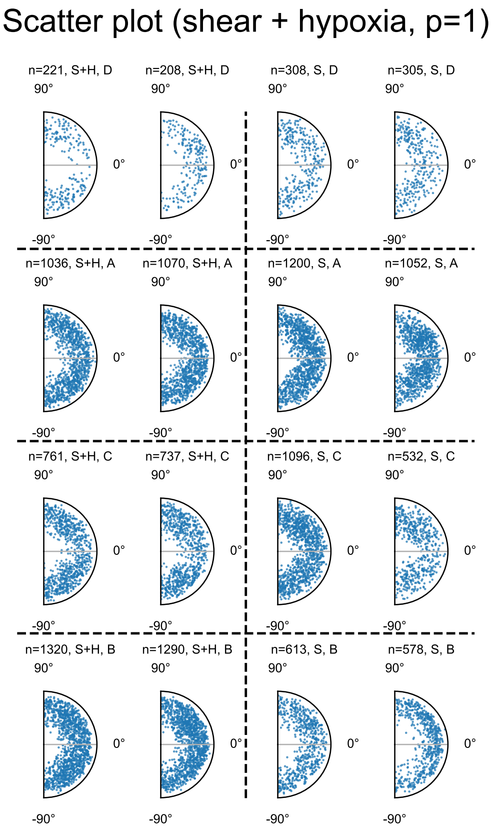
Scatter plot (shear + hypoxia, p=1)

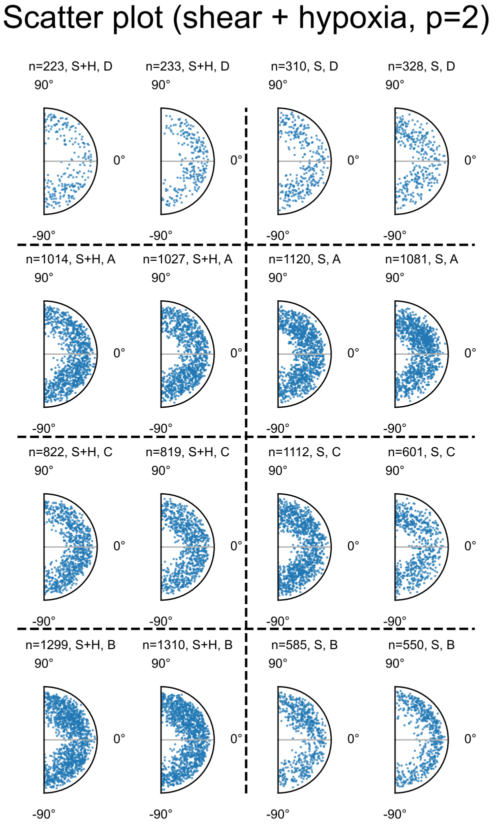
Scatter plot (shear + hypoxia, p=2)

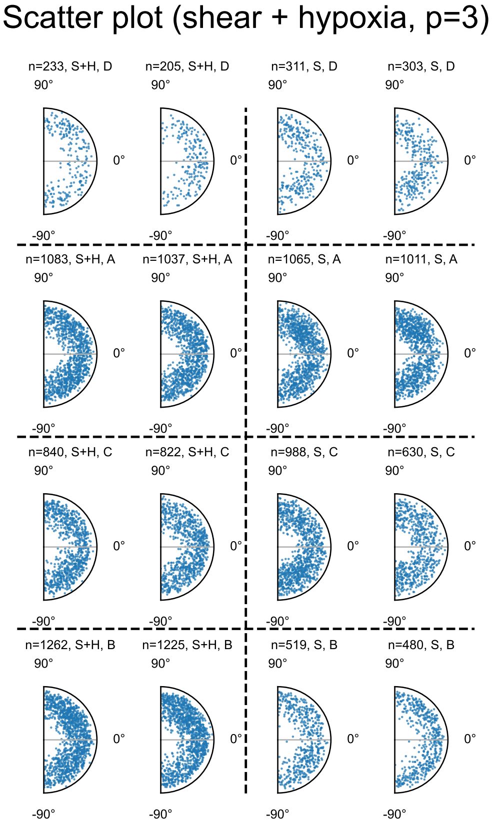
Scatter plot (shear + hypoxia, p=3)

Scatter plot (shear + hypoxia, p=4)

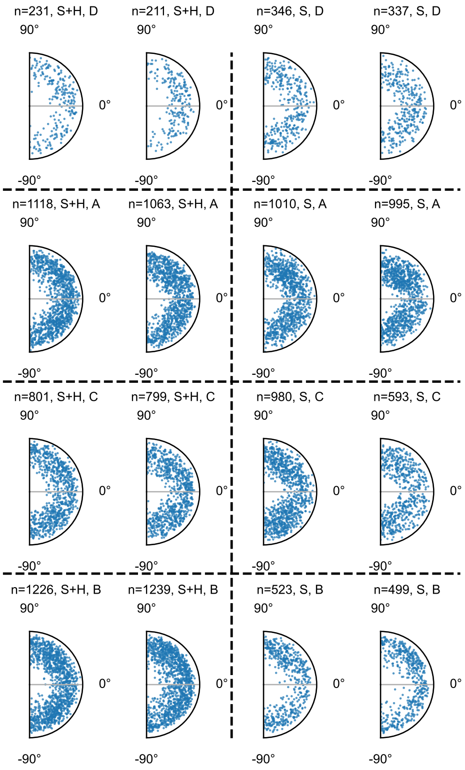

Scatter plot (shear + hypoxia, p=5)

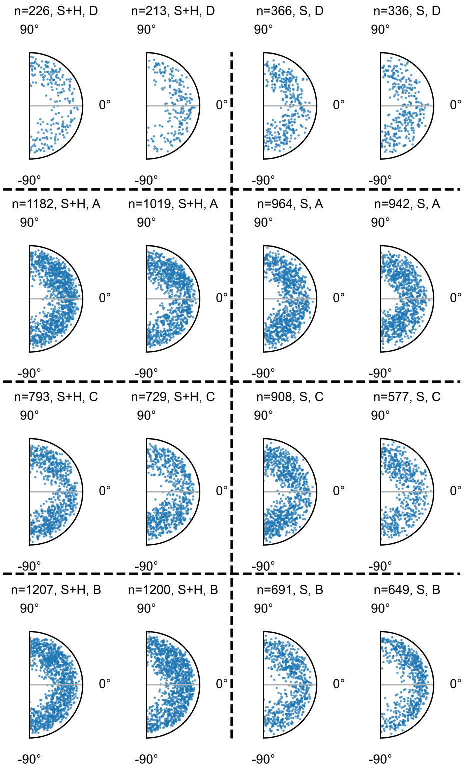

Scatter plot (shear + hypoxia, p=6)

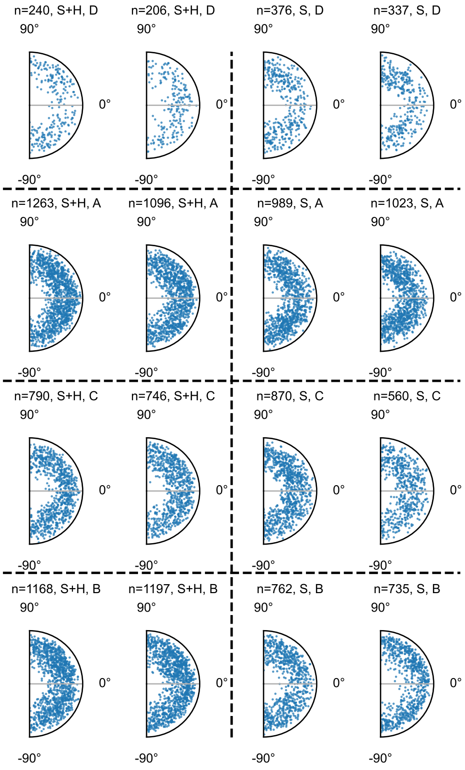

Scatter plot (shear + hypoxia, p=7)

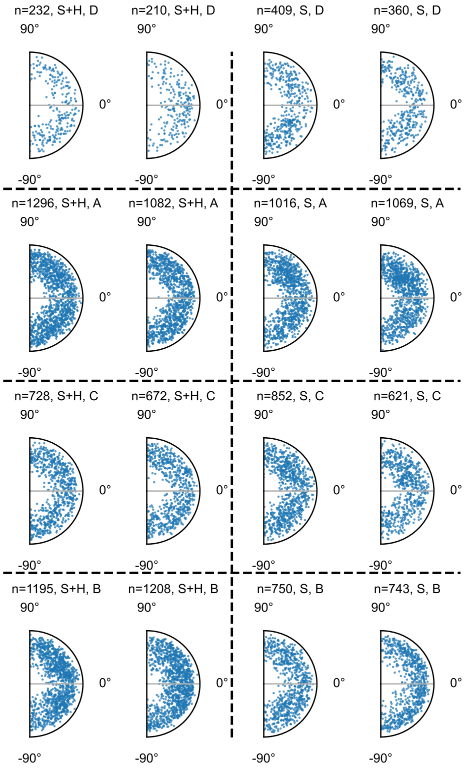

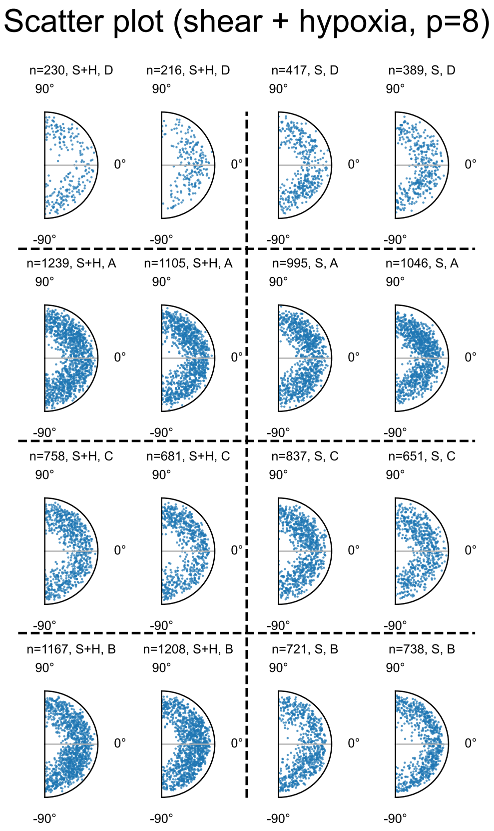
Scatter plot (shear + hypoxia, p=8)
n=230, S+H, D
n=216, S+H, D
n=417, S, D
n=389, S, D
n=1239, S+H, A
n=1105, S+H, A
n=995, S, A
n=1046, S, A
n=758, S+H, C
n=681, S+H, C
n=837, S, C
n=651, S, C
n=1167, S+H, B
n=1208, S+H, B
n=721, S, B
n=738, S, B
90°
0°
-90°

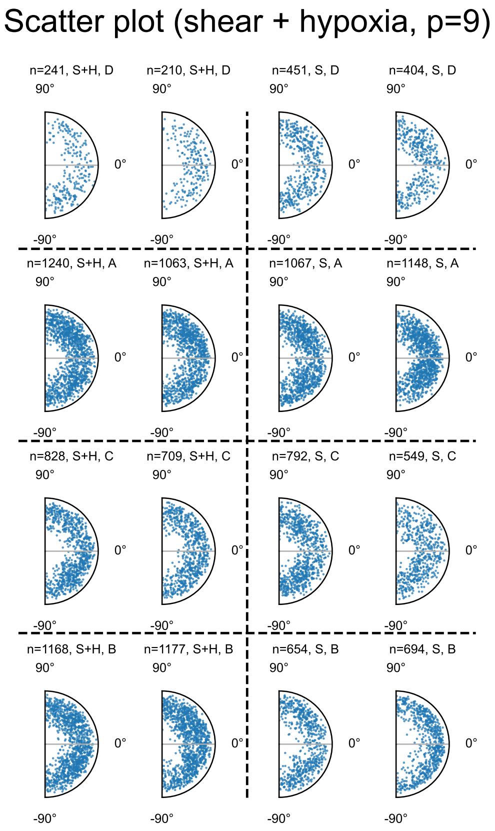
Scatter plot (shear + hypoxia, p=9)
n=241, S+H, D
n=210, S+H, D
n=451, S, D
n=404, S, D
n=1240, S+H, A
n=1063, S+H, A
n=1067, S, A
n=1148, S, A
n=828, S+H, C
n=709, S+H, C
n=792, S, C
n=549, S, C
n=1168, S+H, B
n=1177, S+H, B
n=654, S, B
n=694, S, B
90°
0°
-90°

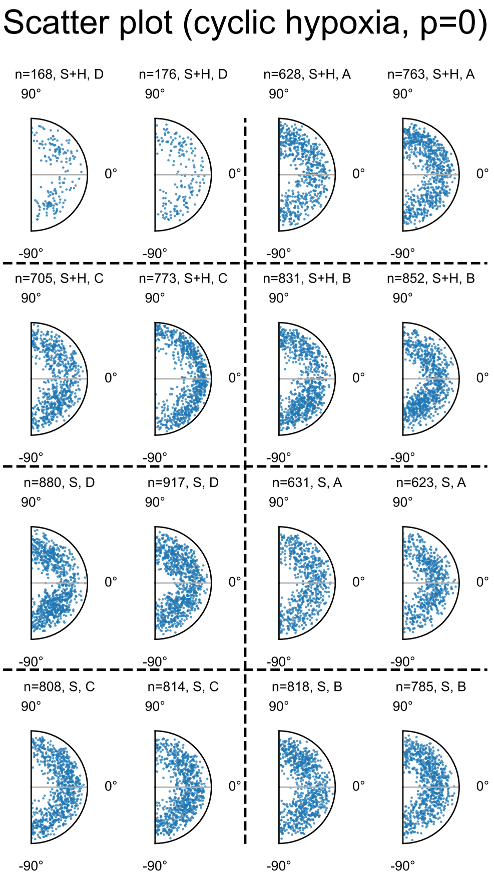
Scatter plot (cyclic hypoxia, p=0)

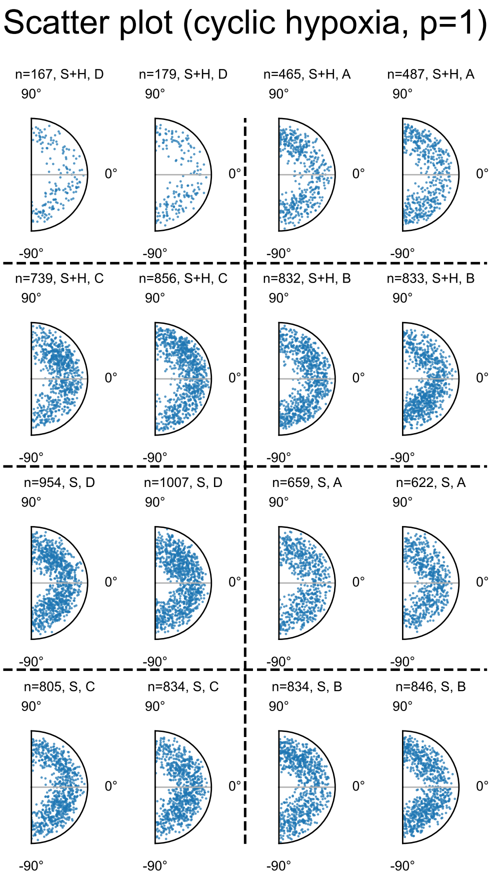
Scatter plot (cyclic hypoxia, p=1)

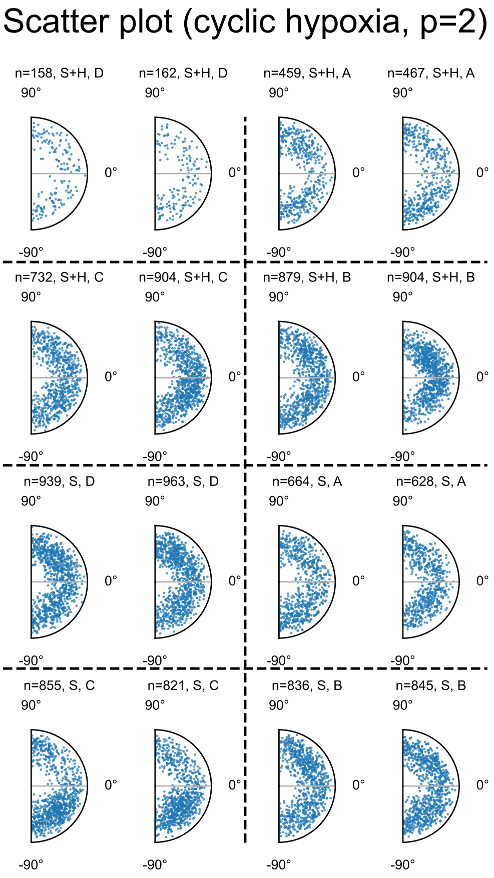
Scatter plot (cyclic hypoxia, p=2)

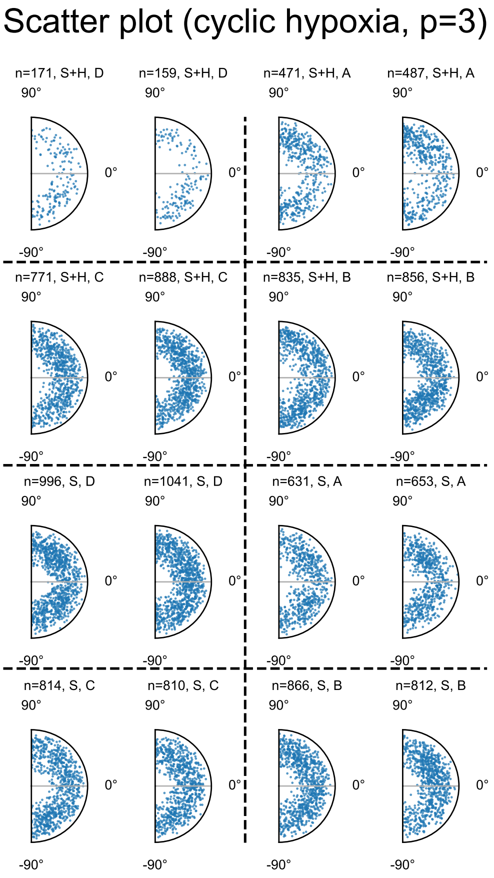
Scatter plot (cyclic hypoxia, p=3)

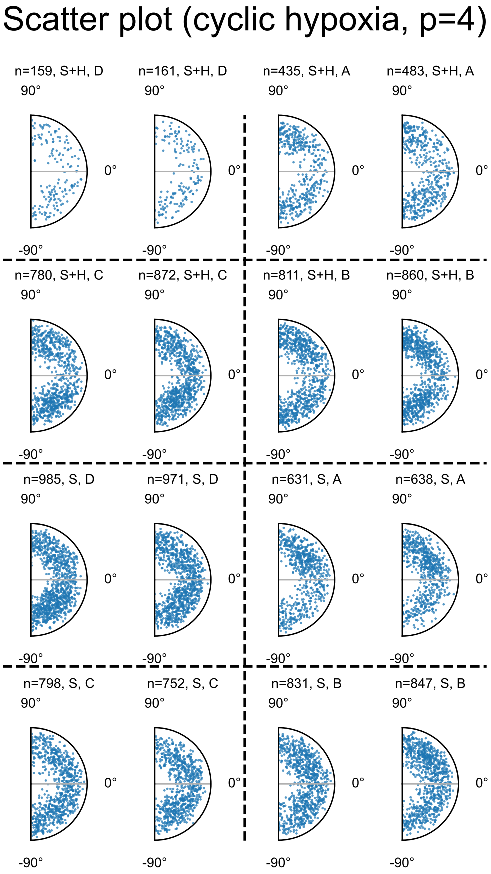

Scatter plot (cyclic hypoxia, p=4)

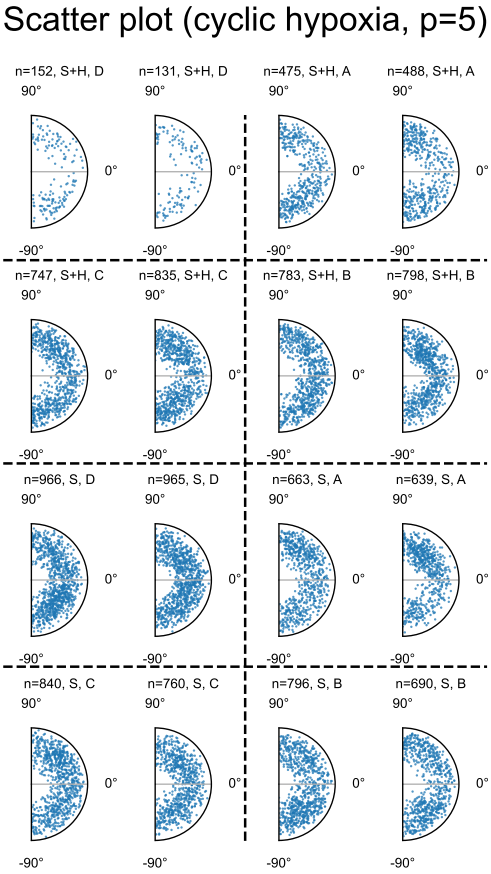

Scatter plot (cyclic hypoxia, p=5)

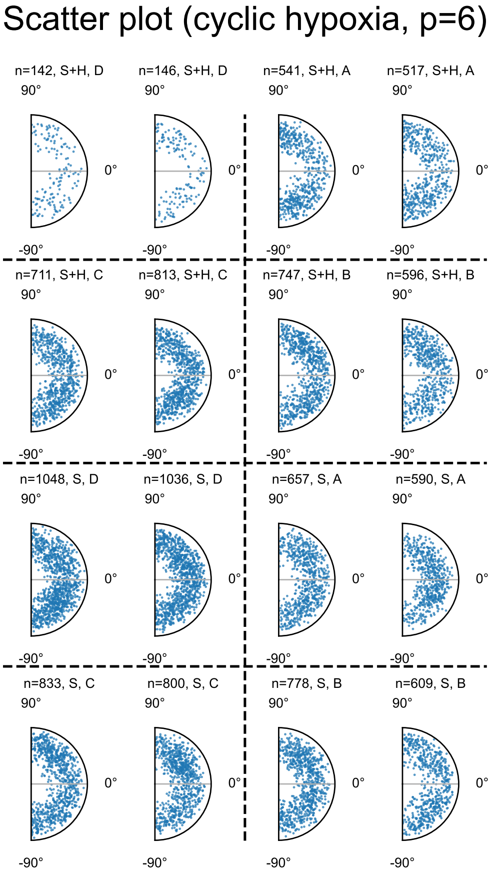

Scatter plot (cyclic hypoxia, p=6)

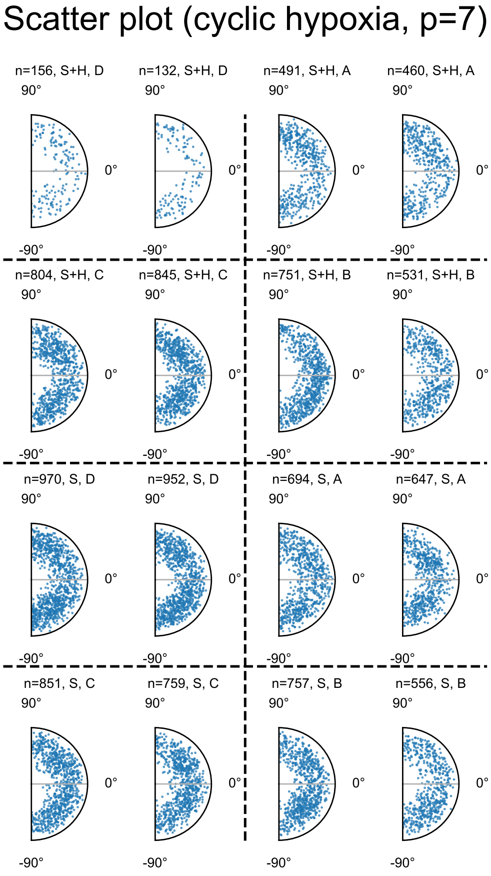

Scatter plot (cyclic hypoxia, p=7)

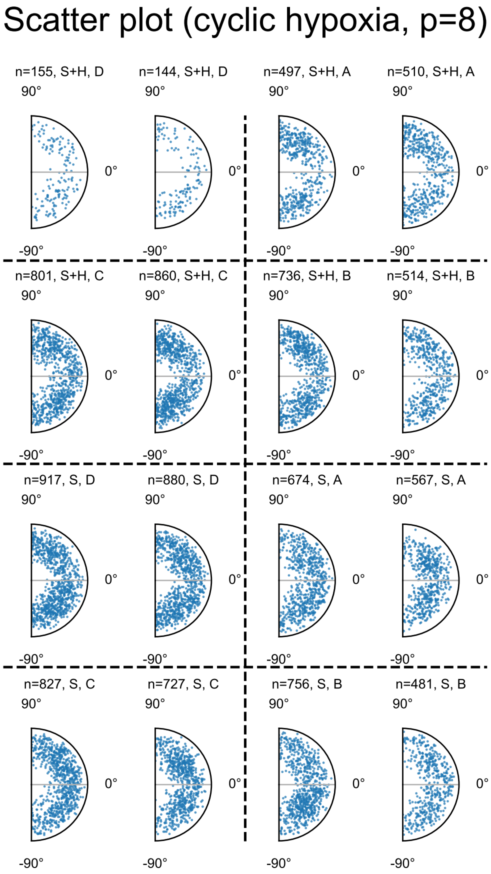

Scatter plot (cyclic hypoxia, p=8)

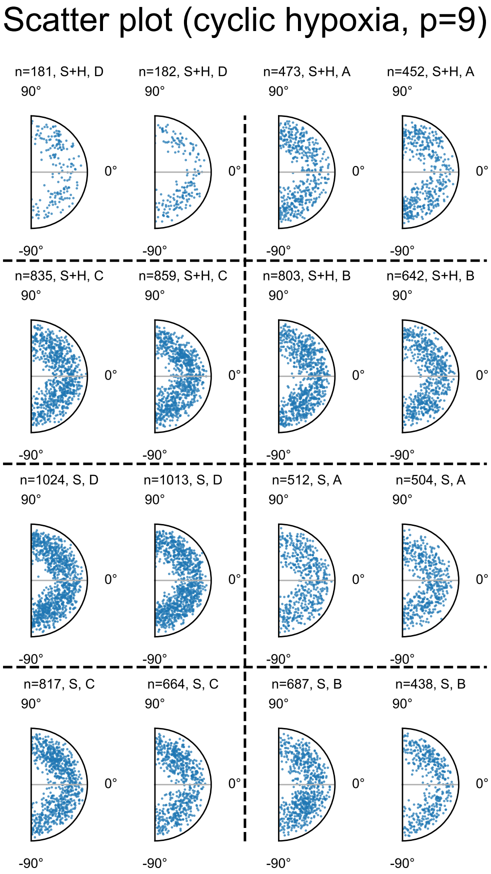

Scatter plot (cyclic hypoxia, p=9)